

1-1-2018

Chemical And Physical Studies Of Charge Transfer Excited States Of Ruthenium Complexes With Aromatic Ligands

Marim Khalifa Alnaed
Wayne State University,

Follow this and additional works at: https://digitalcommons.wayne.edu/oa_dissertations

 Part of the [Chemistry Commons](#)

Recommended Citation

Alnaed, Marim Khalifa, "Chemical And Physical Studies Of Charge Transfer Excited States Of Ruthenium Complexes With Aromatic Ligands" (2018). *Wayne State University Dissertations*. 2001.
https://digitalcommons.wayne.edu/oa_dissertations/2001

This Open Access Dissertation is brought to you for free and open access by DigitalCommons@WayneState. It has been accepted for inclusion in Wayne State University Dissertations by an authorized administrator of DigitalCommons@WayneState.

**CHEMICAL AND PHYSICAL STUDIES OF CHARGE TRANSFER EXCITED
STATES OF RUTHENIUM COMPLEXES WITH AROMATIC LIGANDS**

by

MARIM KHALIFA ALNAED

DISSERTATION

Submitted to the Graduate School

of Wayne State University,

Detroit, Michigan

in partial fulfillment of the requirements

for the degree of

DOCTOR OF PHILOSOPHY

2018

MAJOR: CHEMISTRY (Analytical)

Approved By:

Advisor Date

Advisor Date

© COPYRIGHT BY
MARIM KHALIFA ALNAED
2018
All Rights Reserved

DEDICATION

My dissertation is dedicated to my husband, kids, and family

ACKNOWLEDGMENTS

I would like to start off by giving thanks to Professor John Endicott, my advisor. Since the beginning, his mentorship and guidance has been at the foundation of my graduate education. Professor John Endicott's patience and invaluable guidance regarding comprehensive methods to the formulation of my written work and publication submissions have led me to accomplish more than I imagined possible, during my graduate studies. I truly and greatly appreciate his encouragement to always strive for the best and his constant support during hard times and obstacles I have faced during my time as a graduate researcher.

I would also like to give a special thank you to my previous lab partner, Ryan Thomas. I appreciate the support and aid he shared with me during my time as a researcher.

Also, I would like to thank my committee members: Professor Wen Li, Professor H. Bernhard Schlegel, Professor Colin Poole, and Professor Usmen Mumtaz for their support and guidance throughout my journey.

I would also like to thank my parents for their inspiration and wisdom they have given me; allowing me to persevere and complete my education. Lastly, I would like to thank my husband Mohmmad for his patience and tremendous assistance he provided me throughout my studies.

TABLE OF CONTENTS

DEDICATION	ii
ACKNOWLEDGEMENTS	iii
LIST OF TABLES	viii
LIST OF FIGURES	x
Chapter 1. GENERAL INTRODUCTION.....	1
Chapter 2: “Chemical Scavenging of Short-Lived Products from the Visible Light Photoionization of the tris-bipyridine-ruthenium(II) Triplet Metal-to-Ligand Charge Transfer Excited State”	5
2.1 EXPERIMENTAL	9
2.1.1 Compound preparation	9
2.2 Instrumentation	10
2.2.1 Ambient and 77 k emission and absorption spectrophotometers	10
2.2.2 Electrochemistry	11
2.2.3 Lifetime measurements	12
2.2.4 Proton nuclear magnetic resonance spectroscopy (¹ H NMR)	13
2.2.5 Light sources used for photolysis experiments	13
2.2.6 Photolysis cells and holders	14
2.2.7 Experimental set up for ambient photolysis study of various ruthenium complexes.....	15
2.2.8 Data analysis.....	18
2.3 RESULTS	19
2.3.1 Characterization of experimental systems	19
2.3.2 Fraction of [Ru(bpy) ₃] ²⁺ photodecomposition with irradiation time	24

2.3.3 The dependence of initial rates on light intensity	26
2.3.4 Iodometry	29
2.3.5 Acid dependence of photodecomposition rate	32
2.3.6 Superimposed dual laser irradiations	38
2.3.7 Ambient condition photolysis of $[\text{Ru}(\text{bpy})_3]^{2+}$ with the QTH lamp	42
2.3.8 Comparison of the absorption spectra of the $[\text{Ru}(\text{bpy})_3]^{2+}$ ground state and $^3\text{MLCT}$ excited state to the relative intensity distributions in the global solar spectrum and QTH lamp spectra	43
2.3.9 Estimates of photoionization quantum yields	44
2.3.10 Preliminary observations of the photolysis of various ruthenium complexes under ambient conditions	46
2.3.11. Fitting parameters of other complexes	48
2.3.12. Absorption spectra of ruthenium complexes	50
2.3.13 Emission spectra of ruthenium complexes	51
2.3.14. Excited state lifetimes	52
2.3.15. Diffusion effects	53
2.3.16. An example of the effect of diffusion	59
2.4 DISCUSSION AND CONCLUSION	60
2.5 The $[\text{Ru}(\text{bpy})_3]^{2+}$ $^3\text{MLCT}$ excited state photoionization	60
2.4.2 Significance and implications of $[\text{H}^+]$ -dependent photoionization yields	61
2.4.3 Photoionization yields and threshold energy	64
2.4.4 Possible complications from the generation of photo-substitution products	65
2.4.5 Some other related considerations	66

2.5 Basic mechanistic treatment of: (a) $^3\text{MLCT}$ thermal reactions and (b) photoionization	67
2.5.1 $^3\text{MLCT}$ excited state reactions for generating a substitutional product	67
2.5.2 The chemical equations	67
2.5.3 The rate laws and photostainary states	68
2.5.4 The reduced rate	69
2.5.5 Quantum yield	70
2.6 Acid dependent, two photon photoionization and the photoionization quantum yield expressed in terms of experimental rate parameters	70
2.6.1 Some general considerations and simplifying assumptions	70
2.6.2 Basic reaction	71
2.6.3 Rate equations	72
2.6.4 Quantum yield.....	75
2.7 CONCLUSIONS.....	76
Chapter 3. Studies of the Physical and Chemical Excited State Properties of ruthenium (II) complexes containing aromatic ligands	77
3.1 INTRODUCTION	77
3.2 EXPEIMENTAL SECTION	80
3.2.1 Compounds prepared for the study of the chemical and physical properties of $^3\text{MLCT}$ excited states of ruthenium quinoline complexes	80
3.2 2 Light sources for the study of the chemical and physical properties of $^3\text{MLCT}$ of ruthenium quinoline complexes	86
3.2.3 Instrumental system used for 77 K Emission spectroscopy set up for ruthenium quinoline complexes	86

3.2.4 Instrumental system used for low temperature spectroscopy of Ru-quinoline chromophores	87
3.3 RESULTS	89
3.3.1 Proton Nuclear Magnetic Resonance Spectroscopy (^1H NMR)	89
3.3.2 Absorption Spectra.....	91
3.3.3 77 K emission spectra	94
3.3.4 77 K life-time measurements.....	100
3.3.5. Comparison of the spectroscopic properties of the triplet metal to ligand charge transfer ($^3\text{MLCT}$) various Ru-aromatic complexes.....	102
3.4 DFT Modeling.....	102
3.4.1 Calculated bond dissociation energies of pentaammine-Ru ^{II} complexes with monodentate quinolone ligands	102
3.4.2. Excited state modeling done for this project by Dr. Yi-Jung Tu.....	103
3.5 Ambient and 77 K Life-time measurements of cathepsin L (CSTL) inhibitors bearing Re(I) and Ru(II)	114
3.6 DISCUSSION AND CONCLUSIONS.....	115
3.6.1 Absorption spectroscopy and the singlet excited states.	116
3.6.2 Emission spectroscopy and the triplet excited states.	118
3.6.3 Triplet excited state emission quantum yields, relaxation rates and excited state properties.....	119
3.7. Overview: summary of significance and implications	120
REFERENCES	123
ABSTRACT	137
AUTOBIOGRAPHICAL STATEMENT	139

LIST OF TABLES

Table 1. Contrast in 405 nm laser beam modification by photolysis cells.....	19
Table 2. Dependence of initial photolysis rates on 2-propanol concentration	24
Table 3. Laser intensity ratios based on measured emission intensities	26
Table 4. Average relative intensity of 405 nm radiation absorbed by $[\text{Ru}(\text{bpy})_3]^{2+}$	27
Table 5. Fitting parameters of the initial rates of $[\text{Ru}(\text{bpy})_3]^{2+}$ photodecomposition using 405 nm irradiations in 2 mm cylindrical cell with different light intensities	28
Table 6. Summary of iodometric yield determinations.....	31
Table 7. Initial rates of $[\text{Ru}(\text{bpy})_3]^{2+}$ photodecomposition resulting from the 405 nm Irradiation in acidic 2-propanol solutions in a 2 mm cylindrical cell	36
Table 8. Summary of the fitting parameters of acid dependence of $[\text{Ru}(\text{bpy})_3]^{2+}$ photodecomposition rate in various aqueous acidic solutions in 2 mm cylindrical cell with 405 nm irradiation (Ar deaerated).....	36
Table 9. Summary of the calculated initial rate of the photodecomposition of $[\text{Ru}(\text{bpy})_3]^{2+}$ in a 3 mm id cuvette cell with individual 405 and 532 or the laser beams superimposed	41
Table 10. Summary of the calculated initial rate of the photodecomposition of $[\text{Ru}(\text{bpy})_3]^{2+}$ in a 3 mm cuvette using QTH as irradiation source under ambient condition	42
Table 11. Photoionization quantum yield estimates	45
Table 12. Parameters for quantum yield estimate of $[\text{Ru}(\text{bpy})_3]^{2+}$	48
Table 13. Summary of fitting parameters for Tris(1,10-phenanthroline) ruthenium(II) photodecomposition rate in various aqueous acidic solutions in a 2 mm cylindrical cell with 405 nm radiation (Ar deaerated).....	49
Table 14. Fits of photodecomposition rates found for 405 and 532 nm irradiations of $[\{(bpy)_2\text{Ru}\}_2(2,3\text{-}(dipyridyl)pyrazine)]$	49
Table 15. Initial photodecomposition rates and emission lifetimes for solutions of $[\text{Ru}(\text{bpy})_3]^{2+}$ in a 2 mm cylindrical cell with different amounts of oxygen	56

Table 16. Life-time data for $[\text{Ru}(\text{bpy})_3]^{2+}$ and $[\text{Ru}(\text{bpy})_2(\text{CN})_2]$ for the experimental conditions employed	56
Table 17. Summary of the initial rates determined for superimposed 532 and 405 nm, individual 405 and 532 nm laser irradiations in 3 mm cuvette using the linear fit for $[\text{Ru}(\text{bpy})_2(\text{CN})_2]$ and for QTH lamp irradiations of $[\text{Ru}(\text{bpy})_3]^{2+}$; complexes in aqueous solutions; ambient conditions.....	56
Table 18. Estimation of diffusion effects	58
Table 19. Quantum yield data, radiative and non-radiative rate constants of various $[\text{Ru-TQA-(X)}_2]$, $[\text{Ru-(NH}_3)_5\text{-ISO-Quinoline}]$, and $[\text{Ru(NH}_3)_5\text{-phenyl pyridine}]$	102
Table 20. DFT Calculation of The Bond Energies of $[\text{Ru-(NH}_3)_5\text{-L}]$, L= Quinoline or Iso-Quinoline	103
Table 21. Calculated $^1\text{MLCT}$ energies, oscillator strengths and Natural transition orbitals of the SOMOs for the $\text{S}_0 \rightarrow \text{S}_n$ transitions of RuTQA(ACN)_2	106
Table 22. Relative energies of the $^3\text{MLCT}$ and ^3MC states and orbital contributions (%) of Ru and ligands to the SOMOs	113
Table 23. 77 K and ambient condition lifetime measurements of $[\text{MH-3-110}]$ and $[\text{MH-3-55}]$ with 337 nm excitation in potassium phosphate buffer	115
Table 24. Summary of absorption spectra of the complexes.....	117

LIST OF FIGURES

- Figure 1. A qualitative illustration of the scavenging yield obtained from the formation of the caged pairs as the scavenger concentration is varied. The “*geminate recombination*”, which describes the caged pairs that successfully react, either through *primary* or *secondary recombination*. The time regimes for primary and secondary recombination are probably in the fs and ps, respectively. Only higher acid concentration can compete with the primary and secondary recombination processes. At lower acid concentration, free solvated electrons are scavenged in the ns time regime 7
- Figure 2. Ambient and 77K Lifetime measurements setup 12
- Figure 3. An example of the lifetime instrument response to scattered laser light with no sample. The instrument response function was determined prior to the lifetime measurements and it was determined to be about 11-12 ns. 13
- Figure 4. Schematic diagram shows the cell holder we designed to hold 3 mm cuvette cell for the ambient condition photolysis experiment. 15
- Figure 5. Figure 5. Schematic diagram shows the cell holder designed to hold 2 mm cylindrical cell for the ambient condition photolysis experiment..... 15
- Figure 6. Schematic diagram of the photolysis experimental set up showing the relative positions of the 532 nm and 405 nm lasers and spectrophotometer used 17
- Figure 7. Experimental setup for the QTH lamp output; the sample cell was angled at 45 degrees to minimize the scatter light 17
- Figure 8. Typical extrapolation of the observed emission intensity, I_t , to an “effective intensity at zero-time”, I_0 in the photolysis of $[\text{Ru}(\text{bpy})_3]^{2+}$. The gray rectangle indicates the time where the shutter was partially opened..... 20
- Figure 9. Illustrating the small increase in the emission intensity for 532 nm irradiation of 10^{-4} M $[\text{Ru}(\text{bpy})_3]^{2+}$ with 0.1 M 2-propanol and 0.5 M trifluoroacetic acid in aqueous solution (ambient conditions) 21
- Figure 10. Example of the Andor Solis operating software readout using the kinetic mode: ambient condition photolysis experiment showing the changes in the emission intensity as a result of 405 nm irradiation of $[\text{Ru}(\text{bpy})_3]^{2+}$ in a 2 mm id cylindrical cell. The right panel shows the superimposed variations of the spectral scans as a function of irradiation time and the left shows the spectral scan variations displayed as the kinetic mode output. The solution contained 0.5 M acid, 0.1 M 2-propanol and 1.0×10^{-4} M $[\text{Ru}(\text{bpy})_3]^{2+}$. The spectral scans shown start at 117 s (which excludes the time for opening the shutter), have 39 s intervals and 13 min the time of irradiation 22

Figure 11. Procedure for selection of the initial points for LSQ fits; y-axis is the fractional change of emission after the designated period of photolysis and the x-axis is the irradiation time in seconds. The red line indicates the initial points that we used for the initial rate calculations. 23

Figure 12. The contrasts between the photolysis rates in a 2 mm cylindrical cell of $[\text{Ru}(\text{bpy})_3]^{2+}$ using superimposed 532 & 405 nm irradiation or individual 405 or 532 irradiations. The individual 532 nm is represented by G; and 405 nm is represented by B. The fraction of product formed when the two laser beams were superimposed is represented by B&G. The circles are the fractions of product formed ($F_t = (I_{\text{em}(t=0)} - I_{\text{em}(t)})/I_{\text{em}(t=0)}$) in the separate photolysis experiments. The squares correspond to the individual laser photolyses with F adjusted for the fraction of the intensity that each individual laser contributed to the observed emission in the dual laser experiment (both lasers produce emitting $^3\text{MLCT}$ excited states); in the dual laser experiment $I_{\text{em}(\text{B}\&\text{G})} = f_{\text{B}}I_{\text{em}(\text{B})} + f_{\text{G}}I_{\text{em}(\text{G})}$ where the experimental values are $f_{\text{B}} = 0.57$ and $f_{\text{G}} = 0.43$. The solid lines are fits to eq 1: for this set of experiments $R_{\text{init}}(\text{B}\&\text{G}) = (38 \pm 2)$, $R_{\text{init}}(\text{B}(\text{adj})) = (17 \pm 1)$ and $R_{\text{init}}(\text{G}(\text{adj})) = (-1.1 \pm 0.1)$ $\text{s}^{-1}/10^{-4}$ (B(adj) and G(adj) have been adjusted to account for the fractional contributions of the respective lasers to the observed emission) ; the open squares are for (B(adj) + G(adj)). The difference between $R_{\text{init}}(\text{B}\&\text{G})$ and $R_{\text{init}}(\text{B}(\text{adj}) + \text{G}(\text{adj}))$, see the arrow in the figure, is ΔR_{init} for 405 nm photolysis of that portion of the $^3\text{MLCT}$ excited state that was generated by absorption of 532 nm light. The ratio of the two lasers used in these experiments were calculated from taking the differences in intensities between the two lasers when we irradiation the sample in 3 mm cuvette cell with the superimposed two lasers and the 405 nm irradiation was blocked each 3 minutes for several times. 25

Figure 13. The dependence of the initial photodecomposition rate, R_{init} , of $[\text{Ru}(\text{bpy})_3]^{2+}$ on the square of the incident intensity of 405 nm radiation; the error bars correspond to standard deviations of replicate determinations. The sample contained a deaerated solution of 0.5 M $[\text{H}^+]$, 0.1 M isopropanol and 10^{-4} M substrate. The samples were irradiated in 2 mm id cylindrical cells for 6 min and stacks of microscope slides were used as filters. The dashed line is the LSQ fit ($r^2 = 0.95$): $R_{\text{init}} \times 10^4 = (56 \pm 5)(I_{\text{n}}/I_0)^2 + 0.4 \pm 2.4$ 26

Figure 14. The figure shows the changes in the absorption of $[\text{Ru}(\text{bpy})_3]^{2+}$ that result from 405 nm irradiation (upper panel) and the recovery of Ru^{2+} absorbance after adding an equal volume of 0.01 M KI to the photolyte (compared to the unphotolyzed solution absorbance after adding KI (lower panel). The black area is the unphotolyzed solution absorbance and red area is the photolyzed solution absorbance in both figures. The solutions contained of 1×10^{-4} M $[\text{Ru}(\text{bpy})_3]^{2+}$ and the acid concentration was 4 M, the solution was irradiated with 405 nm for 30 min. The dilution errors were determined from comparisons of the unphotolyzed solution absorbance with and without KI and averaged to be about 10%. The generation of the photo-product ($[\text{Ru}(\text{bpy})_2]^{3+}$) was accompanied by the oxidation of I^- , and we were not able to determine the stoichiometric relationship between them due to the

background absorbencies in the UV region. In addition, the photolysis resulted in a small blue shift in the $\text{bpy-}\pi\pi^*$ absorption at about 250-300 nm 30

Figure 15. The dependence of the photodecomposition rate on, R_{init} , on acid concentration for various Ru^{II} complexes in ambient aqueous solutions with 0.1 M 2-propanol in a 2 mm cylindrical cell: The green circles is for $[\text{Ru}(\text{bpy})_3]^{2+}$, the red squares are for $[\text{Ru}(\text{phen})_3]^{2+}$ and the black diamonds are for $[\{\text{Ru}(\text{bpy})_2\}_2(2,3\text{-dpp})]$ with the 532 nm irradiation and the light blue diamonds for 405 nm irradiation. The errors are the standard deviations of the determinations. The dashed curve is the non-linear least squares fit of eq 2 to the $[\text{Ru}(\text{bpy})_3]^{2+}$ data and the red-dashed curve is the fit of eq 3 for a large number of scavengeable ion pair species. The best fit in both cases required a small positive intercept. The data are from Table 8. 33

Figure 16. The photodecomposition of $[\text{Ru}(\text{bpy})_3]^{2+}$ at low acid concentration. See the caption of Figure 12 for details..... 35

Figure 17. The changes in $^3\text{MLCT}$ emission intensity that accompany irradiation of $[\text{Ru}(\text{bpy})_3]^{2+}$ with superimposed 405 & 532 nm laser beams. The left panel shows the superimposed variations of the spectral scans as a function of irradiation time and the right panel shows the spectral scan variations displayed as the kinetic mode output. The solutions contained 0.5 M acid, 0.1 M 2-propanol and initial concentrations of $[\text{Ru}(\text{bpy})_3]^{2+} = 1.0 \times 10^{-4}$ M. The irradiation times represented start at 117 s (which excludes the time for opening the shutter; the kinetic mode timing is internal in the spectrometer software) with spectral scans at 39 s intervals and 13 min total time of irradiation. The experimental data points were obtained as the intensities of the kinetic mode spectral scans. 39

Figure 18. Experiments illustrating the contrasting fractional decreases in $^3\text{MLCT}$ emission intensity induced by the simultaneous 532 and 405 nm laser irradiations of $[\text{Ru}(\text{bpy})_3]^{2+}$ in ambient acidic solution with those of the 405 nm laser alone in a 3 mm id cuvette (13 min total irradiation time): superimposed 532 and 405 nm laser beams in the left panel and 405 nm laser only in the right panel. The conditions and procedures are as described in the caption of Figure 14, 40

Figure 19. Observed photochemistry of 10^{-4} $[\text{Ru}(\text{II})]$ in aqueous solution with 0.5 M trifluoroacetic acid and 0.1 M 2-propanol using QTH lamp as irradiation source at ambient condition. Red line is the variation of the emission intensity with a < 558 nm cut off filter. The black line is the variation of the emission intensity without using the cut off filter 42

Figure 20. Comparison of the absorption spectra of the ground state and $^3\text{MLCT}$ excited state of $[\text{Ru}(\text{bpy})_3]^{2+}$ to the relative intensity distributions in the global solar and QTH lamp spectra. The green triangles represent the 532 nm and blue is for 405 nm. The amplitudes of the spectra have been adjusted for convenient comparison; the $^3\text{MLCT}$ absorptivity at 405 nm is about three times that of the ground state. The standard global

solar spectrum was downloaded from PVEducation.org, (www.pveducation.org/pvcdrom/appendices/standard-solarspectra) as an EXCEL file . 44

Figure 21. Ambient condition photolysis of $[\text{Ru}(\text{bpy})_2(\text{CN})_2]$, $[\{\text{Ru}(\text{bpy})_2\}_2(2, 3\text{-dpp})](\text{PF}_6)_4$, and Tris(1,10-phenanthroline) ruthenium (II). The photolysis solution contained $2 \times 10^{-4} \text{ M}$ $[\text{Ru}(\text{bpy})_2(\text{CN})_2]$, 0.5 M acetone. The photolysis of $[\{\text{Ru}(\text{bpy})_2\}_2(2, 3\text{-dpp})](\text{PF}_6)_4$, and Tris(1,10-phenanthroline) ruthenium (II) contain $10 \times 10^{-4} \text{ M}$ complex and 0.1 M 2-Propanol, and 0.5 M triflic acid. The irradiation of $[\text{Ru}(\text{bpy})_2(\text{CN})_2]$ was done in 3 mm cuvette, while the irradiation of $[\{\text{Ru}(\text{bpy})_2\}_2(2, 3\text{-dpp})](\text{PF}_6)_4$, and Tris(1,10-phenanthroline) ruthenium (II) were done in a 2 mm cell 47

Figure 22. Ambient absorption of 10^{-4} $[\text{Ru}\text{-tris-1, 10-(phenanthroline)}]$ in 0.5 M triflic acid and 0.1 M Iso-propanol in 4:1 Ethanol: Methanol. 50

Figure 23. Ambient absorption of 10^{-4} $[(\text{Ru}(\text{bpy})_2)_2\text{-2, 3-dpp}]$ complex in butyronitrile 51

Figure 24. 77 K emission spectrum of $[(\text{Ru}(\text{bpy})_2)_2\text{-}(2,3\text{-dpp})]^{4+}$ in butyronitrile 52

Figure 25. Emission decay of $[\text{Ru}(\text{bpy})_3]^{2+}$ in aqueous solution using 337 nm pulsed excitation monitored at 610 nm. The mono exponential fit (black) and the extracted data (pink) are indistinguishable; residuals are in red. (a) monoexponential fit for an aqueous solution of 10^{-4} $[\text{Ru}(\text{bpy})_3]^{2+}$ in 0.1 M 2-Propanol and 0.5 M trifluoroacetic acid; (b) fits for an aqueous solution of 10^{-4} $[\text{Ru}(\text{bpy})_3]^{2+}$ (control); (c) emission decay fits for an aqueous solution of 10^{-4} $[\text{Ru}(\text{bpy})_3]^{2+}$ with 0.1 M 2-Propanol 53

Figure 26. Ambient Emission decay of 10^{-4} M $[\text{Ru}\text{-Tris-1,10-phenanthroline}]$ in 0.5 M aqueous acidic solution and 0.1 M Iso-propanol, emission decay was monitored at 470 nm. 54

Figure 27. 77 K Emission decay of $[(\text{Ru}(\text{bpy})_2)_2(2,3\text{-dpp})]$ in acetonitrile, emission decay was monitored at 530 nm. 55

Figure 28 The parameters used in k_D calculations for the 3mm id cuvette. Segment numbers are circled. I_0 is selected as illustrated in this section 2.3 and/or by comparison to other experiments in the same series. The manual shutter opening (or closing) can complicate the initial intensity determination for a segment and when this happens, we used a short extrapolation as illustrated at the beginning of segment 3 (note that some photochemistry occurs during the opening and closing of the shutter) 59

Figure 29. An example of the effect of vibration and diffusion on the observed emission intensities. The anomaly at 400 s was generated by tapping the photolysis cell. The gray rectangle indicates the time during which the shutter was being opened 59

Figure 30. The initial rate of photodecomposition, R_{init} , replotted as function of $\log_{10}([H^+])$ for the photoionization of $[Ru(bpy)_3]^{2+}$ 3MLCT excited state (green circles) and estimated photoionization yields for the 254 nm irradiation of I^- (white circles). The photoionization yields for the $[Ru(bpy)_3]^{2+}$ 3MLCT excited state were relative to ϕ for $[H^+] = 0.5$ M in Table 7 and were calculated as $\phi_{app} = 3.4 \times R_{init} \times (0.026/52)$; R_{init} data are from Table 2. The photoionization yields for I^- are from Figure 1 of ref. ¹ . The time regime for the e^-/H^+ reaction in aqueous solution is based on the rate constant, $= 2.3 \times 10^{10} \text{ M s}^{-1}$ and $\tau_{react} = 1/([H^+])^2$	61
Figure 31. Synthesis of (1-iso TQA).....	81
Figure 32. Synthesis of $[Ru-(1-iso)-(TQA)(CN)_2]$	84
Figure 33. Synthesis of $[Ru(NH_3)_5(iso-quinoline)]$	86
Figure 34. Ambient and 77K emission spectroscopy setup	87
Figure 35. 90 K absorption spectroscopy set up for ruthenium quinoline Complexes	88
Figure 36. 1H NMR of $[Ru(NH_3)_5-iso-quinoline]$	90
Figure 37. 1H NMR of $[iso-quinoline]$	90
Figure 38. The normalized ambient and 90 K absorption spectra of $[Ru-(1-iso-TQA)-(X)_2]$ series. Top left if the spectrum for $[Ru-(1-iso-TQA)-(CH_3CN)_2]$; top right is for $[Ru-(1-iso-TQA)-(SCN)_2]$, middle bottom is for $[Ru-(1-iso-TQA)-(CN)_2]$. The black line represents the ambient condition absorption while the red line represents the 90 K absorption, all the absorption spectrum were taken in 4: 1 Ethanol: Methanol	92
Figure 39: Ambient and 90 K UV-vis absorption comparison of $[Ru-(3-ISO-TQA)-(NCCH_3)_2]^{2+}$ left, $[Ru-(1-iso-TQA)-(CN)_2]$ right, in 4:1 ethanol: methanol. Black is the ambient spectrum and red is 90 K spectrum, spectrum were taken in 4: 1 Ethanol: Methanol.....	93
Figure 40: Ambient absorption of 10^{-4} M $[Ru(NH_3)_5-Isoquinoline]$ and free iso-quinoline ligand in 4:1 Ethanol: Methanol	94
Figure 41. Normalized 77 K emission spectra of $[Ru(1-ISO-TQA)(NCCH_3)_2]^{2+}$, $[Ru-(1-iso-TQA)-(CN)_2]$ and $[Ru-(1-iso-TQA)-(NCS)_2]$. The emission spectra were in 4: 1 Ethanol: Methanol	95

Figure 42. Normalized 77 K emission spectra of [Ru-(3-iso-TQA)-(NCCH ₃) ₂] ²⁺ , [Ru-(3-iso-TQA)-(CN) ₂] and [Ru-(3-iso-TQA)-(NCS) ₂]. The emission spectra were obtained in 4:1 Ethanol: Methanol	96
Figure 43: 77 K Emission of 6.2E-4 M[Ru(NH ₃) ₅ -iso-Quinoline] in butyronitrile using 470 excitation.	97
Figure 44: Emission spectra observed at 470 nm irradiation of [Ru(NH ₃) ₅ -IQ] complex in butyronitrile at 77 K	98
Figure 45. 470 nm 77 K irradiation of iso-quinoline ligand in 4:1 ethanol : methanol, (i) and butyronitrile (ii)	98
Figure 46. Comparison of the complex and free ligand emissions in ethanol: methanol. Black line represents the 77 K emission using 470 nm excitation; red line represent the 77 K emission of the isoquinoline free ligand at 405 nm excitation; blue line represent the 77 K of the free ligand using 470 nm excitation.	99
Figure 47. 77 K Lifetime measurements of [Ru-(1-iso-TQA)-(NCCH ₃) ₂] top left, [Ru-(1-iso-TQA)-(CN) ₂] top right, [Ru(1-iso-TQA)(NCS) ₂] bottom left, and [Ru(1-iso-TQA)-(Cl) ₂] bottom right	100
Figure 48. 77 K Lifetime Measurements for [Ru-(3-iso-TQA)-(L) ₂] ^{m+} series in 4:1 ethanol: methanol. Top left is the emission decay for [Ru-(3-iso-TQA)-(CN) ₂] ^{m+} , [Ru-(3-iso-TQA)-(SCN) ₂] ^{m+} top right, and bottom is the emission decay for [Ru-(3-TQA)-(CH ₃ CN) ₂] ^{m+}	101
Figure 49. Comparison of calculated (lower “UV-Vis Spectrum”) and experimental (upper; black curve at 300 K and red curve at 90 K) spectra for Ru-1-TQA-(ACN) ₂ . The calculated energies are about 0.5 eV higher energy than the observed peaks.	104
Figure 50. Calculated triplet excited state energies, oscillator strengths and Natural transition orbitals of the SOMOs of [Ru-(1-iso-TQA)-(ACN) ₂].	110
Figure 51. Comparison of donor SOMOs (isovalue=0.03 a.u.) and orbital contributions (%) for the lowest energy CT state of TQA and bpy Ru complexes with the ancillary ligands: A) [Ru-(1-iso-TQA)-(MeCN) ₂] ²⁺ ; B) [Ru-(1-iso-TQA)-(CN) ₂]; C) [Ru(bpy) ₂ (MeCN) ₂] ²⁺ ; D) [Ru(bpy) ₂ (CN) ₂] in the ³ CT optimized geometries	112
Figure 52: Emission decay of [MH-3-110] and [MH-3-55] concentration 47.5 μM and 4.09 μM respectively at ambient and 77 K (frozen solution) ² in potassium phosphate buffer 50	

mM, PH 7.4 and 10% DMSO solvent using 337 N nm pulsed excitation monitored at 543 and 631. (A) [MH-3-110] at 77 K; (B) [MH-3-55] at 77 K. (C) [MH-3-110] at ambient condition. (D) [MH-3-55] at ambient condition. The mono exponential fit (black) and the extracted data (pink) are indistinguishable; residuals are in red. The samples were probably microcrystalline at 77K. A fast decay component with about 10% of the substrate amplitude was probably mostly due to the instrument response to scattered excitation light, but it could also contain contribution from heterogeneities or impurities. Exponential decay fittings performed in Origin; IRF= 12 ns. 114

CHAPTER 1. GENERAL INTRODUCTION

Over the past several decades there have been increasingly sophisticated studies that attempt to develop a scientific understanding of the chemical and physical properties of the lowest triplet states ($^3\text{MLCT}$) of nd^6 transition metal complexes. This strong interest has been stimulated both by the important applications of these complexes and by the challenges presented by excited state electronic configurations that differ significantly from those known for ground state complexes. For example, these materials have been used as sensitizers in dye-sensitized solar cells,³⁻⁶ in photodynamic therapy, etc.⁷⁻⁹

Many of the potential applications involve the lowest energy triplet state and the understanding of the properties of these lowest energy triplet states ($^3\text{MLCT}$) are much more poorly understood than for those of pure organic materials. The chemical properties of molecules depend on their electronic structures and the descriptions of the electronic configurations of $^3\text{MLCT}$ excited states are most often based on idealized models in which light absorption results in oxidation of a metal center and reduction of a ligand moiety of the complex. Emission spectroscopy and contemporary density functional theory techniques have relatively recently shown that such primitive models of electronic structure are not always appropriate.

The lowest energy triplet metal-to-ligand-charge-transfer ($^3\text{MLCT}$) excited states of ruthenium(II) have been of interest for some time largely due to their facile excited state electron transfer reactions or to facile excited state-ligand substitution reactions. In order to design efficient photosensitizers, it is necessary to understand the molecular properties that will optimize these efficiencies.

In addition to the previously mentioned importance of understanding the properties of the charge transfer excited state, understanding the requirement for photoionized electrons to the solvent will be important in biology, solution chemistry and electrochemistry. The solvent plays important role in affecting the outcome and efficiency of the reactions, and light absorption by the ground state of the substrate, a charge transfer to solvent transition (CTTS) state may be generated and this corresponding to the formation of photoionized species. In case of iodide the formation of the CTTS state is accompanied by the formation of $\{S^+, e^-\}_{IP}$ ion pairs. This kind of intermediate has not been reported for the photoionization of transition metal complexes.

The most obvious requirements for an effective excited state photosensitizer are: (a) its chemical integrity during the time of the sensitized reaction; and (b) that it is sufficiently reactive that the rate determining step of the sensitized reaction has a lifetime that is more or less comparable to its excited state lifetime. The chemical integrity of the excited state depends on its various intrinsic decay pathways (including those that are thermally activated) and on its susceptibility to photodecomposition if it absorbs some of the light used in its generation. These factors can be altered to various extents by mixing of the photo-sensitizer excited state with other electronic excited states that have similar energies. Transition metal complexes typically have a large number of electronic excited states whose energies differ only a little from that of their lowest energy excited states. As a result, many excited states can be populated by light absorption with many different relaxation pathways and some mixing among the states with different electronic configurations is expected. The lowest energy excited states of transition metal complexes

are difficult to characterize because: (a) these states have short lifetimes so that standard thermochemical and structural characterization techniques cannot be used; and (b) there are a several excited states that are close in energy and mix to alter the electronic configuration of the lowest energy excited state and the shape of its potential energy surface.

It is theoretically reasonable to expect that the configurational mixing (CI) between different excited states with the same spin multiplicity generally larger than the spin-orbit coupling (SOC) mediated mixing between states with different spin multiplicities for the same energy differences between the mixed states, although there is little direct experimental confirmation of this. Such mixing appears to be important in [ruthenium(II)–(aromatic ligand)] based photo-sensitizers. Balzani and his co-workers¹⁰ have surveyed the synthesis and the photochemical, photophysical, and electrochemical properties of a large number of complexes of the Ru-polypyridine family and the properties of the lowest energy excited states of monobipyridine $[(L)_4Ru(bpy)]^{m+}$ complexes have been extensively examined.¹¹⁻¹⁵ These complexes provide much important information on the properties of metal to ligand charge transfer excited states of potential transition metal sensitizers in which CI seems to be small to moderate.

Over the last decade, many potential photosensitizers have been identified based on metal donors and aromatic ligand acceptors; however, there is insufficient information to explain all the parameters that may lead to an understanding of either the photoionization phenomena and/or help design synthesis of complexes with longer lifetimes. Therefore, the design a system which enables optimization of sensitizer efficiencies for solar energy

conversion or other important applications requires an understanding of the changes in the molecular and electronic properties of the excited states when their coordination environments are changed.

CHAPTER 2. CHEMICAL SCAVENGING OF SHORT-LIVED PRODUCTS FROM THE VISIBLE LIGHT PHOTOIONIZATION OF THE TRIS-BIPYRIDINE-RUTHENIUM(II) TRIPLET METAL-TO-LIGAND CHARGE-TRANSFER EXCITED STATE

Photoionization is among the simplest possible kinds of excited state decomposition and the basic physical principles governing it have been understood for a long time:¹⁶ (a) photoionization occurs once the energy of an absorbed photon exceeds a threshold energy; (b) the threshold energy is a molecular property; (c) the energy of the photon that exceeds the threshold energy appears as kinetic energy in the photo-generated electron. This process is complicated in solutions because the electron's kinetic energy can be transferred to the solvent molecules and this can give rise to a number of electron-containing species. Acid scavenger experiments play a role in the characterization of the intermediate species that are generated from the excitation of a substrate in solution. Since there is relatively little detailed information available about the photoionization of transition metal cationic complexes it is useful to first consider some of the observations on iodide photoionization.

Solution phase photoionization of I^- ¹⁷ has been extensively investigated using both H^+ scavenging for the electron and short pulse laser transient absorption spectroscopy¹⁸. The excitation of iodide ion leads to the generation of charge transfer to solvent transition (CTTS) absorption, and the irradiation of this band give rise to the formation of the neutral iodine atom and the solvated electron. These species undergo a series of reactions in H_2O to form I_2 and H_2 gas. Stein and co-workers^{1, 19-20} used H^+ to scavenge for electrons and alcohols as H-atom scavengers. In addition, they demonstrated that the photogeneration of

electrons did not react with H^+ ions in simple manner, which lead them to postulate that the CTTS state decays into a solvated electron and iodine atom in a solvent cage. Later, Dainton and Logan and co-workers²¹⁻²³ used N_2O as electron scavenger to characterize the intermediate that formed, and they were trying to understand how electrons were formed, how the CTTS state decays and what is the quantum yield efficiency of the electron scavenging. Bradforth and co-workers¹⁷ have studied the photoionization of iodide CTTS system and their results confirmed the formation of short and long-range photo-ejection caged pair $\{I^\bullet, e^-\}_{IP}$ intermediate.

This previous work on I⁻ has suggested that there are three main spatial regimes that are important in the photoionization process: ¹⁷, (a) a contact ion pair $\{I^\bullet, e^-\}_{IP}$ where this solvent caged pair are still in contact with one another and “*Primary recombination*” of these pairs form the iodide ion is in the fs time regime and chemical scavenging is impossible; (b) ion pairs in which the photo-products are separated by one or more solvent molecules and “*Secondary recombination*” is slower (ps time regime) so that some chemical scavenging is possible; (c) the pairs have diffused so far apart that “*combination*” of the photo-products is in the ns time regime so that the free solvated electrons can be scavenged at lower acid concentrations. These processes are schematically illustrated in Figure 1.

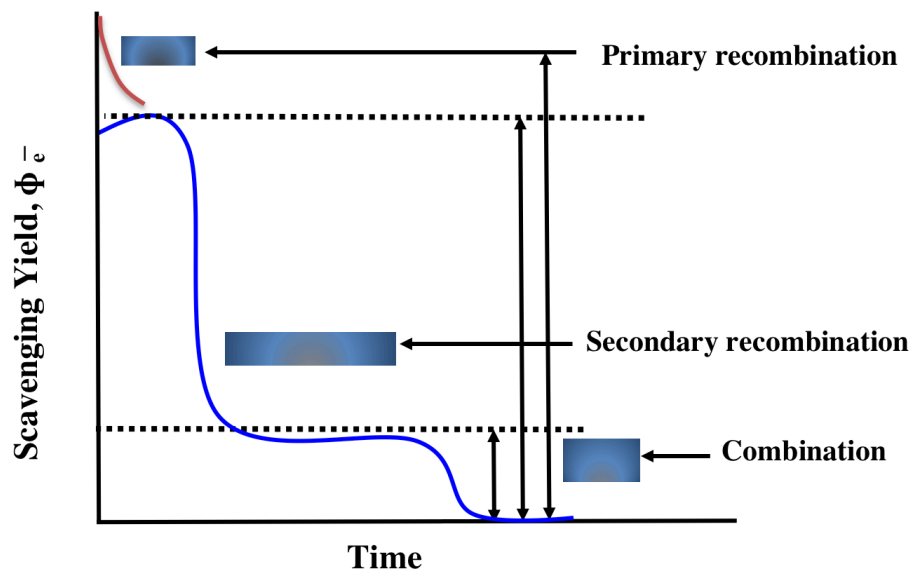


Figure 1: A qualitative illustration of the scavenging yield obtained from the formation of the caged pairs as the scavenger concentration is varied. The “*geminate recombination*”, which describes the caged pairs that successfully react, either through *primary* or *secondary recombination*. The time regimes for primary and secondary recombination are probably in the fs and ps, respectively. Only higher acid concentration can compete with the primary and secondary recombination processes. At lower acid concentration, free solvated electrons are scavenged in the ns time regime.

The photoionization of iodide illustrates the basis for the interpretation of our observations.¹⁷ Although information on the photoionization of anions is readily available, there are few studies on photoionization²⁴⁻²⁹ of cations, or more specifically, transition metal cationic complexes in solution. In previous work, the photoionization²⁵⁻²⁹ of $[\text{Ru}(\text{bpy})_3]^{2+}$ in solution has been based on the spectroscopic detection of free electrons, not associated with $[\text{Ru}(\text{bpy})_3]^{3+}$ in the bulk solution. This is in contrast to the interpretations of the photoionization of iodide in solutions summarized above.^{1, 17, 30-31} Our approach was to use chemical scavengers to probe the photoionization of the $[\text{Ru}(\text{bpy})_3]^{2+}$

complex in aqueous solution. One of the most important issues in characterizing the photoionization process is the value of the threshold energy, E_{th} , which can be based on thermodynamic parameters, and the nature of the photo-products formed. Photoionization of molecules occurs for photons with energy $h\nu > E_{th}$ and the excess photon energy, $E_{xs} = (h\nu - E_{th}) > 0$, in vacuum appears mostly as kinetic energy of the electron. This kinetic energy can be largely dissipated in solutions by means of interactions with solvent.

The rarity of the detailed reports on CTTS absorptions for cationic species may be due to competing absorptions of some states that are characteristic of these complexes since their absorption may obscure the CTTS absorptions. Our expectations were that the photoionization of these cationic complexes would lead to the generation of ion pairs and free solvated electrons as has been found in the photoionization of the iodide ion. Due to the electrostatic interactions of the photo-products, the separation of the photoionization products is likely to be more difficult for these cations than for I^- , the photo-generated electrons are likely to have shorter recombination lifetimes for similar separation distances and electron/ Ru^{3+} product attractions probably extend over a greater distance for cationic than for anionic substrates.

Matsubara and Ford studied the photoionization of the hexamine ruthenium(II) complex, $[Ru(NH_3)_6]^{2+}$ and they were able to efficiently scavenge for free solvated electron, e_{aq}^- ³²⁻³³ within an acid range of $0.001-0.01^{1-2}$ M H^+ . A significant optical absorption band of $[Ru(NH_3)_6]^{2+}$ has been assigned as (CTTS) transition^{32, 34-35} at 275 nm (4.5 eV). This corresponds to the energy required for a photon to promote an electron into the solvation sphere of the complex with the ground state nuclear coordinates fixed, but it

does not correspond to the minimum energy required to ionize the complex. The irradiation of the $[\text{Ru}(\text{NH}_3)_6]^{2+}$ CTTS absorption (at 254 nm) generates $[\text{Ru}(\text{NH}_3)_6]^{3+}$ and the solvated electron with a quantum yield of 0.36³³. In our study, we used H^+ ion as electron scavenger and find moderate acid dependent quantum yields for 405 nm photoionization of the $[\text{Ru}(\text{bpy})_3]^{2+}$ ³MLCT excited state in aqueous solution under ambient condition.

2.1 Experimental

2.1.1. Compound preparation

The following commercial chemicals were purchased from Sigma-Aldrich and used without further purification: tris-(2,2'-bipyridine)ruthenium(II) chloride; 2-Propanol ($\geq 99.5\%$); high purity trifluoromethylsulfonic acid ($\geq 99.5\%$). Spectroscopic grade acetone ($\geq 99.5\%$) and trifluoroacetic acid ($\geq 99.5\%$) were purchased from Alfa-Aesar. The $[\text{Ru}$ -tris-1,10-phenanthroline] $(\text{PF}_6)_2$ (95% purity) was purchased from Strem Chemical INC. Lithium carbonate, $[\{\text{Ru}(\text{bpy})_2\}_2(2,3\text{-dpp})](\text{PF}_6)_4$ was synthesized as reported previously³⁶ (a sample was also provided by Prof. Y. J. Chen).

In most of the photolysis experiments we used solutions of 10^{-4} M $[\text{Ru}(\text{bpy})_3]^{2+}$, various trifluoroacetic acid (TFA) or triflic acid (HOTf) ranging from 10^{-4} – 4 M and 0.1 M 2-propanol prepared in deionized water and transferred to the photolysis cell by means of a syringe. Samples were renewed after each irradiation sequence. All samples were deaerated with argon through the solution mixture using stainless steel needles, serum capped vessels and the effluent gas was vented through water in a beaker for 30 min. All the photolysis solutions were prepared in the dark. Photolysis experiments were performed

with individual 405 or with superimposed 405 and 532 nm irradiations of solutions in a 2 mm id cylindrical cell or/and 3 mm fluorescence cuvette cell.

Synthesis of $[(bpy)_2Ru(dpp)Ru(bpy)_2](PF_6)_4$ ³⁶

A solution of 0.42 g, 0.867 mmol, $[Ru(bpy)_2Cl_2] \cdot 2 H_2O$ and 0.1 g, 0.426 mmol, of 2,3-dpp were refluxed in 30 mL of deaerated 95% ethanol for 72 h. After this time the reaction mixture was filtered and evaporated to dryness. The solid was dissolved in a minimum of deaerated water and a saturated solution of NH_4PF_6 was added. The solid was isolated after washing with a little water and then with ether. The resulting material was dissolved in the smallest amount of 5:3(v/v) water/acetone, and the resulting solution was chromatographed on Sephadex-C-25 ion-exchange resin. Elution with 0.3 M NaCl gave the desired purple band. The solution was partly evaporated in vacuo, and solid NH_4PF_6 was added until the precipitation was completed. The product was recovered as a purple solid, dissolved in acetonitrile and precipitated with ethanol. It was then washed several times with ethanol and then once with ether, and eventually dried in vacuo. Typical yield ~ 56%. For $C_{54}H_{38}N_{12}P_4F_{24}Ru_2$ (calcd): C, 39.92 (39.61); H, 2.10 (2.32); N, 10.64 (10.26)%

2.2 Instrumentation

2.2.1. Ambient and 77 K Emission and absorption spectrophotometers

Ambient absorption spectra were determined with a Shimadzu UV-2101PC spectrophotometer (1 Nishinokyo Kuwabara-cho, Nakagyo-ku, Kyoto 604-8511, Japan). An Andor Shamrock 500 spectrometer with an Andor Newton DU920-BV CCD detector was used for the ambient and 77 K emission spectra. The Andor spectrometer was calibrated using an Oriel Model 6045 calibrated Xe pen lamp

emission lines and a NIST traceable Oriel model 63966 Quartz Tungsten Halogen (QTH) lamp for intensity. The Andor Newton detector was used for visible light detection in the wavelength range of 385 - 900 nm. The spectrometer was equipped with three gratings: 150 l/mm, 3001/mm; 800 nm blaze; 500 nm blaze; 1200 nm. Light was captured with ‘‘1’’ plano-convex optic and focused to an F/# matcher by a Thorlabs 3 mm Core Liquid Light Guide LLG0338-4. The function of F/# matcher is to match the emitted light to the optics of the Andor SR500i and has 6.5, numerical aperture (NA) of 0.077, acceptance angle of 8.8° and 2.9 magnification. The use of the liquid light guide and detector together resulted in a limit of 395 nm for the shortest wavelength of spectral detection.

2.2.2. Electrochemistry

Synthesized complexes were characterized in part with cyclic voltammetry. The electrochemical measurements were performed with several different solvents, all solutions were purged with argon, 0.1 M Bu₄NPF₆ was used as the electrolyte, sample concentrations ranged from 10⁻⁴-10⁻⁵ M. Tetrabutylammonium hexafluorophosphate was used as an electrolyte in a BAS 100B electrochemical system with a three-electrode system: Ag/AgCl reference electrode, a Pt wire counter electrode, and a Pt disk working electrode. 1 μM diamond polish was used to polish the working electrode on a Buehler polishing cloth. A scan rate was 150 mV/s, solutions were purged with argon. The measurements started from zero and swept in the negative direction, ferrocene was used as an internal reference.

2.2.3. Lifetime measurements

The ambient and 77 K emission lifetimes were determined using a Spectra Physics VSL-337ND-S nitrogen laser-pumped DUO-210 Dye laser system and a Jobin-Yvon H-

10 spectrometer for detection with PMT output digitized using a PC with a National Instruments NI PCI-5154, 2 GS/s, 1 GHz digitizer with 8 MB/ch on board memory PC card as described previously.³⁷⁻³⁸ For photolysis experiments, emission decay lifetimes were determined for aerated, deaerated, or oxygen saturated samples with the sample concentration of 10^{-4} M. The Dewar was only used in the 77 K lifetime measurements.

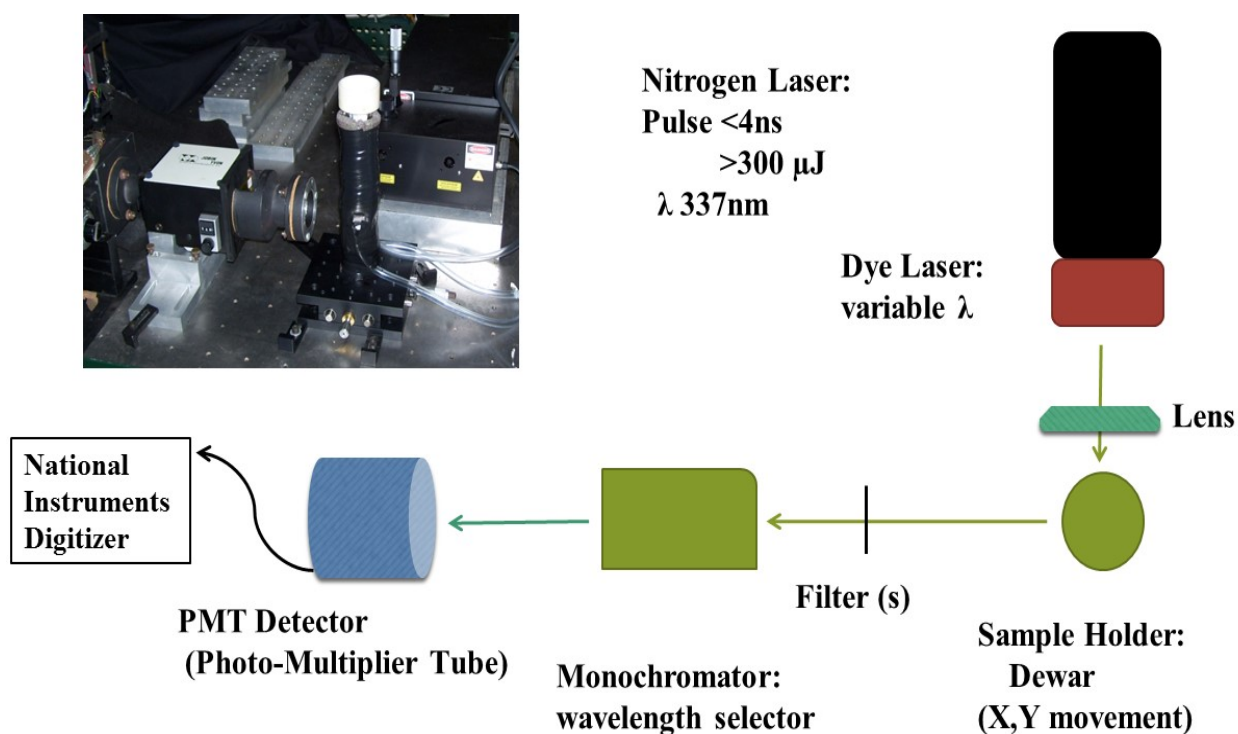


Figure 2: Ambient and 77K Lifetime measurements setup

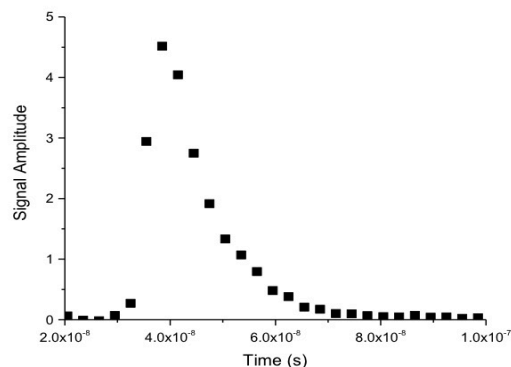


Figure 3. An example of the lifetime instrument response to scattered laser light with no sample. The instrument response function was determined prior to the lifetime measurements and it was determined to be about 11-12 ns.

2.2.4. Proton Nuclear Magnetic Resonance Spectroscopy (¹H NMR)

¹H NMR spectra were obtained with an Oxford 400 MHz magnet fitted with a default Varian 1H/19F/13C/31P PFG Auto Switchable 5mm, VT (-20°C to +80°C) probe in the Lumigen Instrumentation Center at Chemistry department, Wayne State University. The samples were dissolved in deuterated solvents, dimethylsulfoxide (C₂D₆SO), acetonitrile (CD₃CN), water (D₂O), and acetone (C₂D₆CO). The aliphatic protons of the complexes were spread in the upfield region and aromatic rings (bpy), (dpp), and quinoline ligands. protons were found in the downfield region of the spectra. The pure synthesized complexes were further characterized with other analytical techniques.

2.2.5. Light Sources used for photolysis experiments

Most irradiations were performed using continuous wave diode laser modules: (a) 405 nm (nominally ≥ 50 mW; Power Technologies, Inc.); (b) and/or 532 nm (nominally ≥80 mW; Laserglow Technology); 470 nm excitation nominally ≥ 10 mW; Changchun

New Industries Optoelectronics Tech.Co., Ltd. Laser output power was measured using a Coherent Fieldmate Laser Power meter; part number 1067353 with OM 10 Powermax sensor (provided by Professor Wen Li) and the output power of the 405 and 532 nm lasers was measured as 46 ± 2 and 139 ± 5 mW, respectively. Some irradiations were performed using the broad band output of an Oriel model 63966 Quartz Tungsten Halogen (QTH) lamp.

2.2.6. Photolysis cells and holders

Several different photolysis cells have been used: (a) A 3 mm id square fluorescence cell with internal dimensions of 3x3 mm (Starna catalog # 3-3.30-SOG-3). This cell was securely mounted on a specially designed cell holder to minimize the effects of building vibrations, and the cell holder was made of aluminum and was fixed securely by anchoring to the optical table, the shape of the cavity was square with a dimension of 0.4 cm for each side, and the depth of this cavity was 0.3 cm. The cell was fixed to a stack of 5 two inch of aluminum blocks bolted together and fixed to the Newport optical table; Figure 4 (b) A 2 mm id cylindrical fluorescence cell: This cell was also mounted on a specifically designed holder with holes in the top and the bottom, the diameters of the top hole is 0.3 cm and the bottom one is 0.2 cm, the depth of the top hole is about 3 cm and the bottom one is about 2 cm , this design allowed the 2 mm cell to be set tightly in the base of the holder and the holder was anchored in the table; Figure 5 (c) A Starna model 18-SOG-10 cuvette with internal dimensions of 10x4 mm mounted in a fabricated 1-cm cuvette holder.

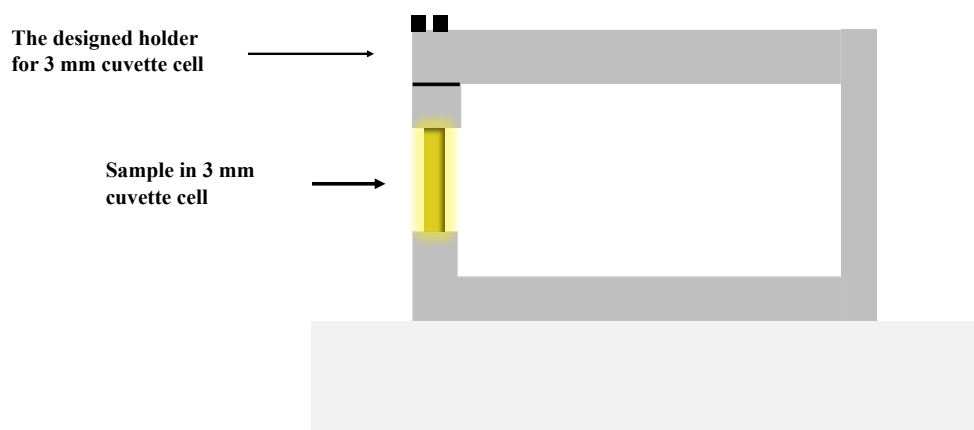


Figure 4: Schematic diagram shows the cell holder we designed to hold 3 mm cuvette cell for the ambient condition photolysis experiment.

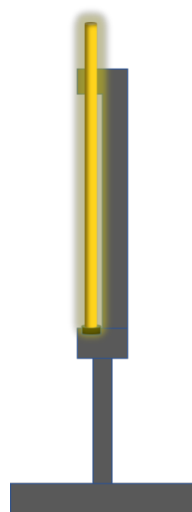


Figure 5. Schematic diagram shows the cell holder designed to hold 2 mm cylindrical cell for the ambient condition photolysis experiment.

2.2.7 Experimental set up for ambient photolysis study of various ruthenium complexes

The experiments employed a cut-off filter which only transmits wavelengths longer than 558 nm in the front of the liquid light guide to remove most of the scattered excitation light. A concentration of 10^{-4} M $[\text{Ru}(\text{bpy})_3]^{2+}$ was used to ensure uniform absorption of the

laser light through the cell. The emitted light was collected at approximately 90° to the excitation beam(s).

All the photolysis solutions were prepared in the dark. Most of the basic characterizations of the $[\text{Ru}(\text{bpy})_3]^{2+}$ photolysis were performed with 405 nm irradiations of solutions in a 2 mm id cylindrical cell. The two photon nature of the $[\text{Ru}(\text{bpy})_3]^{2+}$ photolysis was further characterized using superimposed 405 and 532 nm laser beams with sample solutions in a 3 mm id cuvette. For these studies the 532 and 405 nm lasers beams were aligned so that they were superimposed in solution with angles in the range of 137°-180° between their beams which were incident on opposite sides of the cell see Figure 6. This arrangement enabled the separation of the $^3\text{MLCT}$ generation step, by single photon 532 nm absorption, and its subsequent photolysis with 405 nm radiation. There was some uncertainty in the exact alignment of the laser beams inside the various cells we used. The diode laser radiation sources had 1 mm beam diameters. As a consequence, the volume of the photolysis region was smaller than the total solution volume and small volume cells to minimize the volume difference. 2 mm cylindrical cells were used in the characterization of the photochemical process because diffusion complications were relatively small. We used the 3 mm cuvette cell for quantum yield determinations.

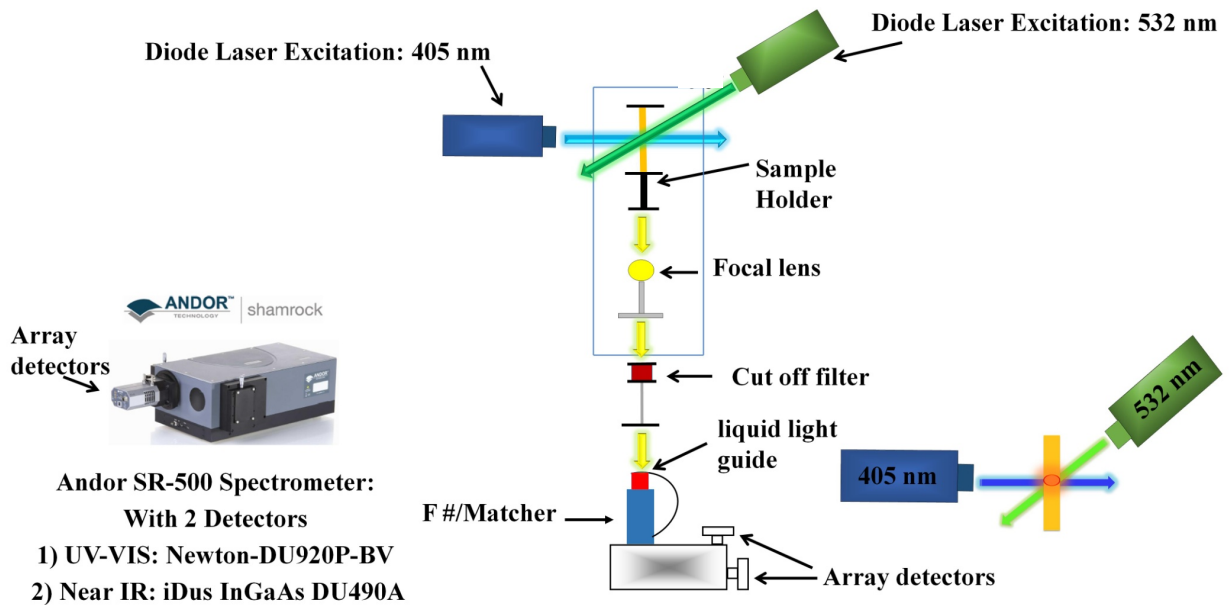


Figure 6: Schematic diagram of the photolysis experimental set up showing the relative positions of the 532 nm and 405 nm lasers and spectrophotometer used.

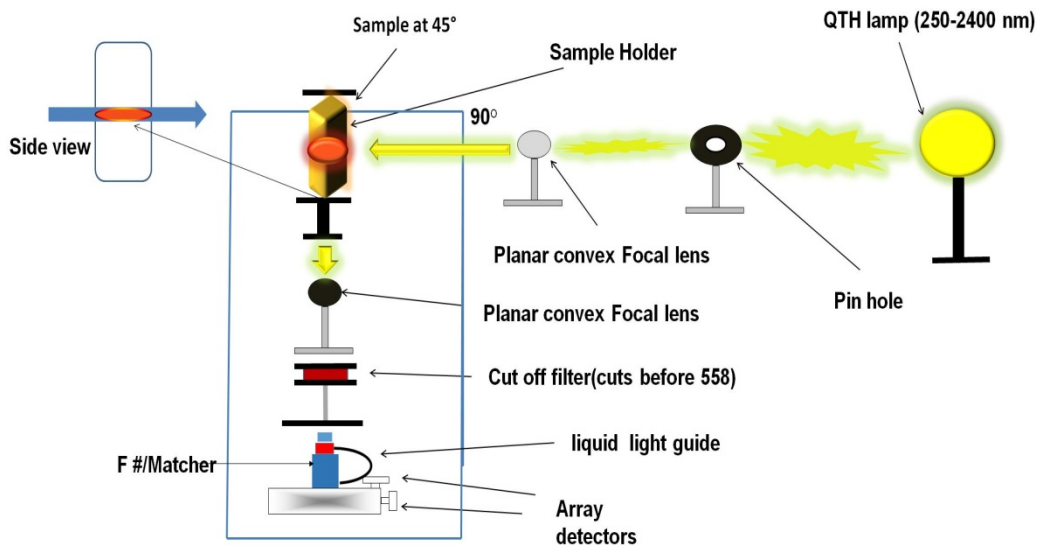


Figure 7: Experimental setup for the QTH lamp output; the sample cell was angled at 45 degrees to minimize the scatter light.

2.2.8. Data analysis

Emission intensity and absorption spectral data were transferred from the Andor Solis or Shimadzu data files, respectively, to a computer EXCEL file. For experiments in which intensity data were collected in the kinetic mode, the intensity data were converted to the fraction of intensity decrease, $F_t = (I_{t=0} - I_t)/I_{t=0}$, (where F_t is the fraction of photoproducts formed at time t ; $I_{t=0}$ is the emission intensity at zero time; and I_t is the emission intensity at time t) plotted as a function of the irradiation time, t . Since the time for opening the manual shutter was significant compared to the initial photolysis times, we estimated $I_{t=0}$ by extrapolating the initial intensities to the time at which the shutter was half open. The variations in F_t with irradiation time were fitted to eq 1.

$$F_t = F_{\infty}(1 - \exp(-k(t - t_0))) \quad (1)$$

where the parameters F_{∞} , k and t_0 were obtained by non-linear Least Square Fit (LSQ) fitting routines in either PSIPLOT or Origin.³⁹⁻⁴⁰ Equation 1 consistently gave excellent fits to the data obtained in each experiment when the kinetic plots were significantly curved. For most of the experiments, the fitted data were used to determine the “initial rate”, R_{init} , as $R_{init} = F_{\infty} \times k$, since $F_t \xrightarrow{t \rightarrow 0} F_{\infty} \times k$. Linear least squares fits were used for the initial slopes of F_t when the F vs. t plots had very little curvature.

The iodometric experiments involved measurements of small differences in absorbance determined in a partly filled semi-micro cuvette and there were occasional baseline problems. In order to minimize these, we adjusted the sample absorbancies in EXCEL to average zero in the 650-700 nm range. When the absorption of the KI solution was significantly different from zero at the shorter wavelengths it was subtracted from the

spectra of samples treated with KI. The depletion of $[\text{Ru}(\text{bpy})_3]^{2+}$ was determined from the difference in the absorption at 452 nm of the photolyzed and unphotolyzed solutions; the recovery was determined from the difference at 452 nm of these solutions after addition of an equal volume of aqueous KI.

2.3. Results

2.3.1. Characterization of experimental systems

a. The distortion of the laser beams by the walls of the photolysis cells has been examined by the beam shape at various distances after the cell. The observations are summarized in Table1. The 3 mm cuvette does not distort the beam significantly, but the 2 mm cylindrical cell does.

Table1. Contrast in 405 nm laser beam modification by photolysis cells

Distance past the cell	Diameter of the laser beam after the photolysis cell
2 mm cylindrical cell	
0.5 cm	Almost 1 mm
7 cm	1.2 cm (horizontal line)
17 cm	6.5 cm (horizontal line)
3 mm cuvette	
1 cm	1 mm
6 cm	1.2 mm
14 cm	1.5 mm

b. Estimation of initial intensity. Since the time required to open the manual shutter was significant it was necessary to estimate the initial intensity by extrapolation to the time when it was about half open as illustrated in Figure 8.

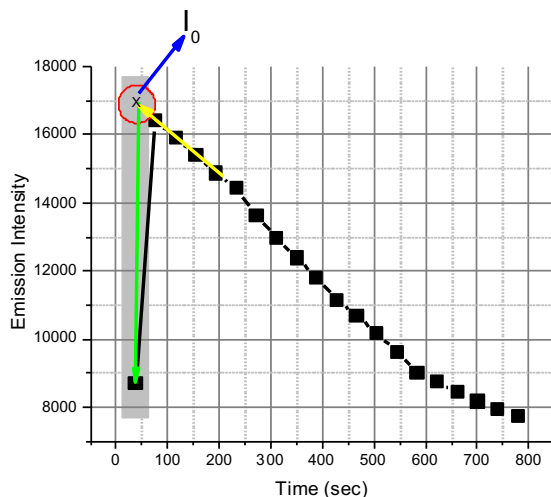


Figure 8: Typical extrapolation of the observed emission intensity, I_t , to an “effective intensity at zero-time”, I_0 in the photolysis of $[\text{Ru}(\text{bpy})_3]^{2+}$. The gray rectangle indicates the time where the shutter was partially opened.

c. An example of intensity increased by 532 nm irradiation

Small increases in emitted emission intensity was observed for 532 nm irradiations in aerated solutions as shown in Figure 9. No significant changes were observed for 532 nm irradiations of deaerated solutions of $[\text{Ru}(\text{bpy})]^{2+}$.

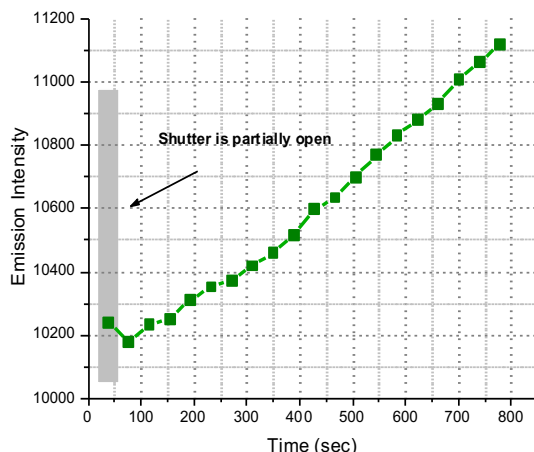


Figure 9. Illustrating the small increase in the emission intensity for 532 nm irradiation of 10^{-4} M $[\text{Ru}(\text{bpy})_3]^{+2}$ with 0.1 M 2-propanol and 0.5 M trifluoroacetic acid in aqueous solution (ambient conditions).

d. General observations of the 405 nm irradiation of $[\text{Ru}(\text{bpy})_3]^{2+}$ and illustration of data obtained in the kinetic observation mode.

The 405 nm irradiation of the $[\text{Ru}(\text{bpy})_2]^{2+}$ $^3\text{MLCT}$ excited state resulted in an efficient substrate decomposition while 532 nm irradiations alone did not show any photodecomposition. There are no significant changes in the $[\text{Ru}(\text{bpy})_2]^{2+}$ emission energy maximum or bandshape for the irradiation periods used; see Figure 10 for the observations. The calculated initial rates from these observations are based on the integrated intensities of the spectral scans obtained using the kinetic mode. Aqueous hydrogen ion, H^+ , was used for an electron scavenger and 2-propanol to scavenge H-atoms in order to observe significant photodecompositions. Strong acids were used whose anions are relatively unreactive towards the solvated electron.

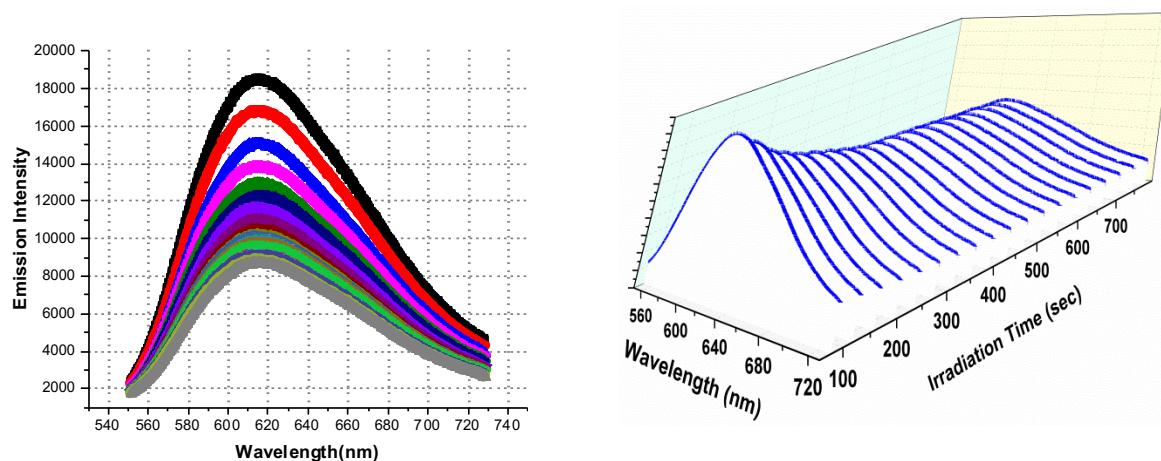


Figure 10: Example of the Andor Solis operating software readout using the kinetic mode: ambient condition photolysis experiment showing the changes in the emission intensity as a result of 405 nm irradiation of $[\text{Ru}(\text{bpy})_3]^{2+}$ in a 2 mm id cylindrical cell. The right panel shows the superimposed variations of the spectral scans at different irradiation times and the left shows the spectral scan variations displayed as the kinetic mode output. The solution contained 0.5 M acid, 0.1 M 2-propanol and 1.0×10^{-4} M $[\text{Ru}(\text{bpy})_3]^{2+}$. The spectral scans shown start at 117 s (which excludes the time for opening the shutter), have 39 s intervals and 13 min the time of irradiation.

e. Illustration of selection of points for LSQ treatment

The linear least squares fitting method was used for initial rate estimates when the observed intensity variations had little curvature as illustrated in Figure 11.

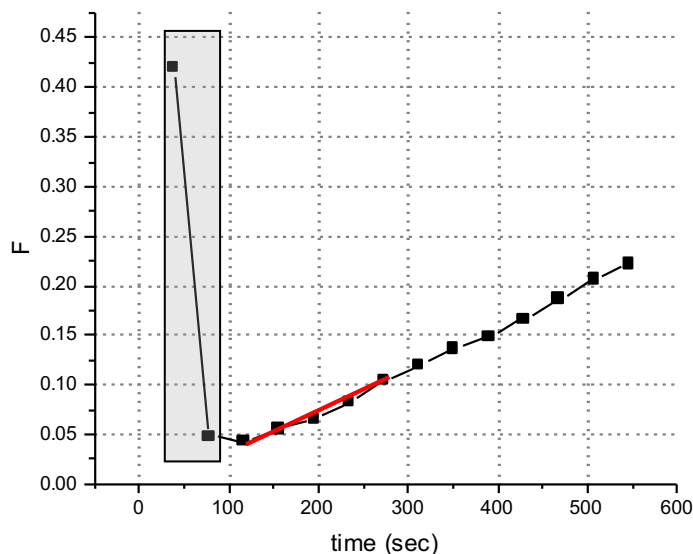


Figure 11. Procedure for selection of the initial points for LSQ fits; y-axis is the fractional change of emission after the designated period of photolysis and the x-axis is the irradiation time in seconds. The red line indicates the initial points that we used for the initial rate calculations.

f. Variations of R_{init} with the variation of [2-propanol] concentration. R_{init} increased with the increases of [2-propanol] > 0.1 M. The rate constant for the $H^{\bullet}/2$ -propanol reaction is reported to be $7.4 \times 10^7 \text{ M}^{-1}\text{s}^{-1}$,² and this reaction should have about a 140 ns mean lifetime in 0.1 M 2-propanol. Thus, 0.1 M 2-propanol is a good scavenger for the free H-atom. At [2-propanol] ≤ 0.1 M R_{init} is independent of [2-propanol] concentration which illustrates that the reactions of the free aqueous H-atom with either the substrate or with the $[Ru(bpy)_3]^{3+}$ photoproduct do not greatly complicate our observations. However, for [2-propanol] > 0.1 M the R_{init} was found to increase possibly as a result of a significant amount of 2-propanol in the solvation sphere of the substrate leading to either: (a) a smaller energy difference between the 3MC and 3MLCT excited states than with purely water solvation

and an enhancement of ligand substitution; or (b) that the H^\bullet that is formed in the $[\text{Ru}(\text{bpy})_3]^{3+}$ solvation sphere might reduce it to $[\text{Ru}(\text{bpy})_3]^{2+}$.

Table 2. Dependence of initial photolysis rates on 2-propanol concentration. ^a

[2-propanol], M	k, $\text{s}^{-1} \times 10^4$	F_∞	$R_{\text{init}},$ $\text{s}^{-1} \times 10^4$
0	$15 \pm 1^{\text{b}}$
0.1	35 ± 1	0.40 ± 0.01	14 ± 3
0.1	$14 \pm 1^{\text{b}}$
1	33 ± 2	0.79 ± 0.02	21 ± 3
1	39 ± 2	0.65 ± 0.02	26 ± 3
3	54 ± 3	0.72 ± 0.01	39 ± 4

^a Irradiated at 405 nm in a 2 mm id cylindrical cell; deaerated solutions contained 1.0×10^{-4} M $[\text{Ru}(\text{bpy})_3]^{2+}$ and 0.5 M HOTf; fitted to eq 1 except as indicated. ^b Linear LSQ fit of the initial data points. Error limits are standard deviation of replicate determination.

2.3.2 Fraction of $[\text{Ru}(\text{bpy})_3]^{2+}$ photodecomposition with irradiation time

532 nm irradiation did not result in $[\text{Ru}(\text{bpy})_3]^{2+}$ photodecomposition, however, there was a small increase in the emission intensity which arises from increases in the $^3\text{MLCT}$ photostationary state concentration as $[\text{O}_2]$ is decreased (due to local heating and/or electron scavenging). The 532 nm irradiations can be used to generate the $^3\text{MLCT}$ excited state that can then be photolyzed by 405 nm irradiation. The 405 nm irradiations also generate the $^3\text{MLCT}$ excited state from the ground state of the $[\text{Ru}(\text{bpy})_3]^{2+}$. The rate of the photodecomposition was approximately doubled when we used superimposed 405 and 532 nm laser irradiation compared to the sum of the individual laser contributions; see Figure 12.

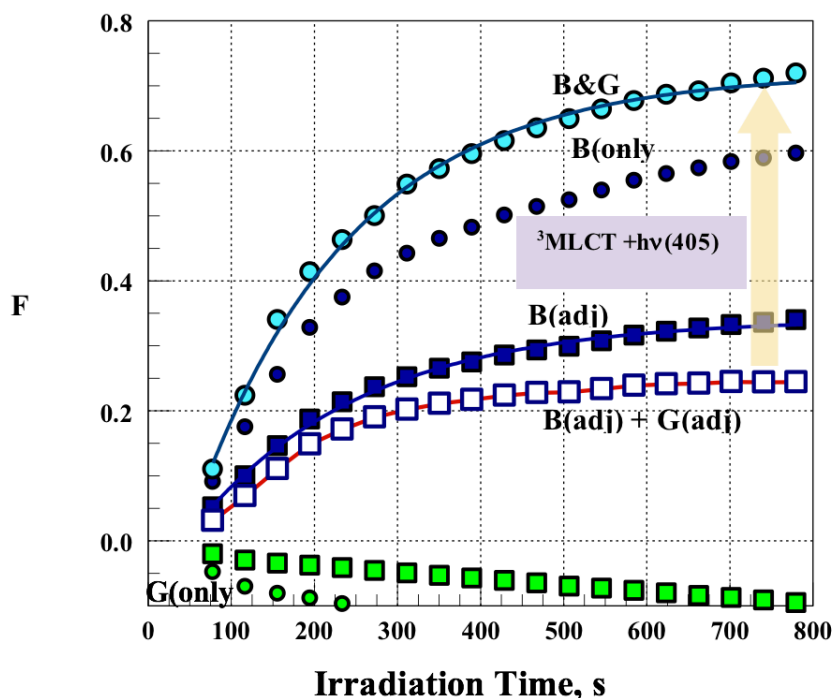


Figure 12. The contrasts between the photolysis rates in a 2 mm cylindrical cell of $[\text{Ru}(\text{bpy})_3]^{2+}$ using superimposed 532 & 405 nm irradiation or individual 405 or 532 nm irradianations. The individual 532 nm irradiation is represented by G; and that at 405 nm is represented by B. The fraction of product formed when the two laser beams were superimposed is represented by B&G. The circles are the fractions of product formed ($F_t = (I_{em}(t=0) - I_{em}(t))/I_{em}(t=0)$) in the separate photolysis experiments. The squares correspond to the individual laser photolyses with F adjusted for the fraction of the intensity that each individual laser contributed to the observed emission in the dual laser experiment (both lasers produce emission emitting $^3\text{MLCT}$ excited states); in the dual laser experiment $I_{em(B\&G)} = f_B I_{em(B)} + f_G I_{em(G)}$ where the experimental values are $f_B = 0.57$ and $f_G = 0.43$. The solid lines are fits to eq 1: for this set of experiments $R_{init}(B\&G) = (38 \pm 2)$, $R_{init}(B(\text{adj})) = (17 \pm 1)$ and $R_{init}(G(\text{adj})) = (-1.1 \pm 0.1) \text{ s}^{-1}/10^{-4}$ (B(adj) and G(adj) have been adjusted to account for the fractional contributions of the respective lasers to the observed emission); the open squares are for (B(adj) + G(adj)). The difference between $R_{init}(B\&G)$ and $R_{init}(B(\text{adj}) + G(\text{adj}))$, see the arrow in the figure, is ΔR_{init} for 405 nm photolysis of that portion of the $^3\text{MLCT}$ excited state that was generated by absorption of 532 nm light. The ratio of the two lasers used in these experiments were calculated from taking the differences in intensities between the two lasers when we irradiation the sample in 3 mm cuvette cell with the superimposed two lasers and the 405 nm irradiation was blocked each 3 minutes for several times.

Table 3. Laser intensity ratios based on measured emission intensities

Segment/Experiment	$I_t(\text{B\&G})/I_t(\text{G})$			$I_t(\text{B\&G})/I_t(\text{B})$	
	216	217	218	219	220
1	2.34	2.42	2.40	2.20	1.79
2	2.54	2.74	1.98	1.69	1.59
3	2.12	2.09	2.45	1.93	1.5
4	2.41	2.4	2.5	1.68	1.68
5			1.96	1.62	
Experiment Average	2.4±0.2	2.41±0.27	2.26±0.27	1.84±0.24	1.64±0.12
Overall average	2.34±0.23			1.74±0.21	
	$I_t(\text{B})/I_t(\text{G}) = 1.33 \pm 0.3 = \epsilon_{405(\text{S})} I_{405}^{\text{in}} / \epsilon_{532(\text{S})} I_{532}^{\text{in}}$				

In the correction of $R_{\text{obs}(\text{B\&G})}$ for intensity contributions of the individual lasers, $f_{\text{B}} = 0.57 \pm 1.8$ and $f_{\text{G}} = 0.43 \pm 0.13$.

2.3.3. The dependence of initial rates on light intensity

The photodecomposition induced by 405 nm irradiation of $[\text{Ru}(\text{bpy})_3]^{2+}$ complex for our experimental conditions is second order in light intensity as illustrated by Figure 13.

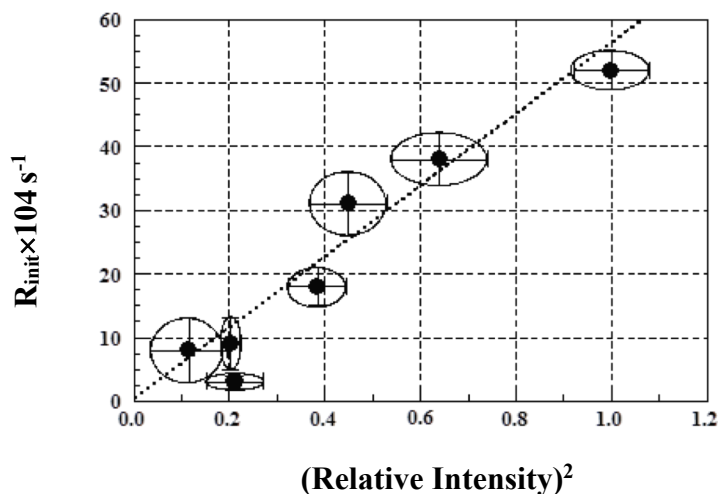


Figure 13. The dependence of the initial photodecomposition rate, R_{init} , of $[\text{Ru}(\text{bpy})_3]^{2+}$ on the square of the incident intensity of 405 nm radiation; the error bars correspond to standard deviations of replicate determinations. The sample contained a deaerated solution of 0.5 M $[\text{H}^+]$, 0.1 M isopropanol and 10^{-4} M substrate. The samples were irradiated in 2 mm id cylindrical cells for 6 min and stacks of microscope slides were used as filters. The dashed line is the LSQ fit ($r^2 = 0.95$): $R_{\text{init}} \times 10^4 = (56 \pm 5)(I_n/I_0)^2 + 0.4 \pm 2.4$.

Table 4 shows the relative intensity of 405 nm irradiation that was absorbed by $[\text{Ru}(\text{bpy})_3]^{2+}$ complex, this intensity was calculated as the intensity observed for the complex when there were no slides divided by the intensity observed when there are different numbers of the microscope slides in the front of 405 nm lasers.

Table 4. Average relative intensity of 405 nm radiation absorbed by $[\text{Ru}(\text{bpy})_3]^{2+}$.

Slides in stack	I(scattered light)	I(Ru emission) ^a
0	1	1
2		0.8
3	0.72	
4		0.67
7	0.66	0.66
10	0.34	0.34
Average Intensity abs./slide	0.07	0.07

^aFrom Table 5.

The data was fit using equation 1 for the acid concentration > 0.01 and LQS fits was used to fit the data for the acid concentration < 0.001 and the summary of fitting parameters are shown in Table 5.

Table 5. Fitting parameters of the initial rates of [Ru(bpy)₃]²⁺ photodecomposition using 405 nm irradiations in 2 mm cylindrical cell with different light intensities.

Experiment	I _{t=0} , counts	Filter	I _{abs(S)(Filter)} ÷ I _{abs(no Filter)}	Exponential fit; F=			R _{obs} × 10 ⁴ , s ⁻¹		
				F _∞ (1-exp(-k(t-t ₀)))					
				F _∞	k	t ₀			
MA274	11200	none	1.00±0.04 ^c	0.68(1) ^a	0.076(2)		52±3		
				0.65(4)	0.0081(1)	28(1)	53±4		
Averages			1.00±0.04	66(3)	0.0078(3)		52±4		
MA300	16000	2 slides	0.88±0.14	0.95(15) ^a	0.0040(3)		38±6		
MA318	13000			0.59(1)	0.0067(3)	10(2)	40±6		
MA317	13000			0.63(9)	0.0061(2)	13(1)	38±6		
Averages			0.88±0.14	0.7(2)	0.006(1)		39±6		
MA301	14100	4 slides	0.79±0.07	0.73(5) ^a	0.0045(4)		32±8		
MA315	11000			0.56(1) ^a	0.0062(3)		32±7		
				0.55(2)	0.0069(6)	3(4)			
Averages				0.79±0.07	LSQ: ^b				
MA316 ^a	11750			0.63(1) ^a	0.0058(2)		36±1		
MA316 ^b	12000			0.59(1)	0.0069(4)	-3(3)	41±4		
MA328	10600	0.86(5)	0.0024(2)	16(3)	21±4				
Averages			0.79±0.07	0.6(1)	0.006(1)		32±6		
MA273	8250	6 slides	0.6±0.07	0.23(1) ^a	0.050(3)		22±10		
MA302	12500			0.57(4)	0.006(10)	22(14)			
				MA313	10500	1.1(3) ^a	0.0020(6)		22±9
Averages				0.6±0.07	0.9	0.002(1)		19±2	
Averages				0.6±0.07	LSQ:				
MA313	11600			0.56(1)	0.0048(4)	1(3)	27±4		
MA329	10600			1.1(2)	0.0016(5)	10(5)	18±6		
MA330	11000	0.74(4)	0.0030(2)	23(2)	22±3				
Averages			0.6±0.07	0.7(3)	0.004(2)		22±6		
MA545 ^a	2500	8 slides	0.52±0.10	0.36(6)	0.0028(8)	122(7)	3±2		
MA545 ^a	2100			0.122(1)	0.0021(8)	-15(5)	2.6±0.8		
Averages				0.52±0.10	0.24(12)	0.0026(8)		6±4	
MA275	11200	9 slides	0.45±0.03	LSQ ^b			13±5		
				0.46(4)	0.0036(7)	20(10)			
Averages			0.45±0.03	0.46(4)	0.0036(7)		13±5		
MA546 ^a	2800	10 slides	0.30±0.15	0.16(1) ^a	0.0078(8)	66±5	12±1		
MA546	2500			0.11(1) ^a	0.0030(2)	120±15	3±1		
Averages			0.30±0.15	0.14(2)	0.0054(20)		8±5		

^a Fitted to $F = F_{\infty}(1 - \exp(-k \times t))$. ^bLSQ fits

2.3.4. Iodometry

The relative yields of the Ru(III) photoproducts that were generated from the 405 nm laser irradiations were determined by the oxidation of iodide at various acid concentration with various irradiation times. The solutions used consisted of 10^{-4} M $[\text{Ru}(\text{bpy})_3]^{2+}$ and 0.1 M 2-propanol and 10^{-3} - 4 M acid. The samples were deaerated with argon and irradiated with 405 nm for various times. The absorbance at 452 nm ($\epsilon_{\text{max}} = 14,600 \text{ M}^{-1}\text{cm}^{-1}$) was used to determine the concentration of $[\text{Ru}(\text{bpy})_3]^{2+}$ before and after photolysis and with and without KI added to the photolyzed solution after photolysis. The results are shown in Figure 14 and the summary of the recovered yield of Ru^{2+} for those experiments are shown in Table 6. Figure 14 also shows that most of the bleached $[\text{Ru}(\text{bpy})_3]^{2+}$ absorption was recovered as a result of the $[\text{Ru}(\text{bpy})_3]^{3+}$ oxidation of iodide. These observations demonstrate that most of the photo-oxidized product is $[\text{Ru}(\text{bpy})_2]^{3+}$ and the overall average of the recovered absorption of $[\text{Ru}(\text{bpy})_2]^{2+}$ over an acid variation was calculated to be $80 \pm 20\%$. There could be a minor photosubstitution reaction pathway ($16 \pm 10\%$; Table 6) even at higher acid concentration where our uncertainties are relatively small.

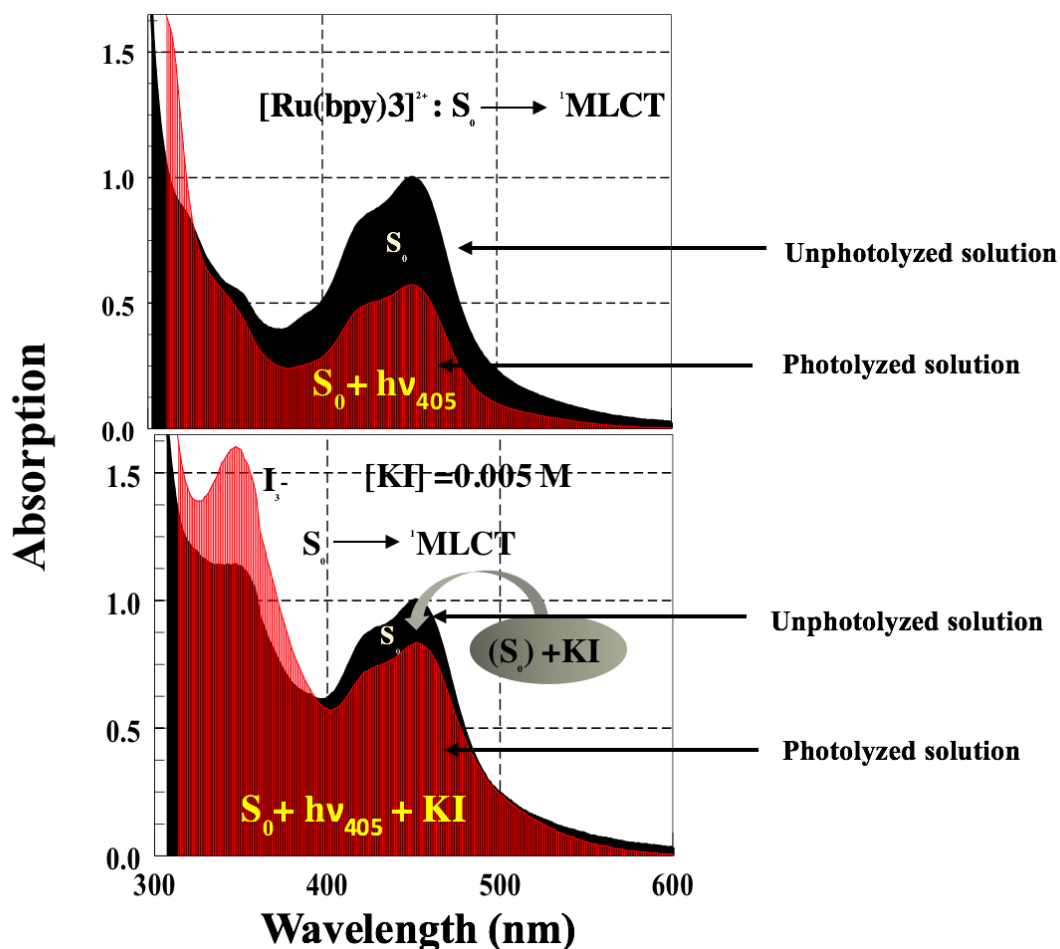


Figure 14. The figure shows the changes in the absorption of $[\text{Ru}(\text{bpy})_3]^{2+}$ that result from 405 nm irradiation (upper panel) and the recovery of Ru^{2+} absorbance after adding an equal volume of 0.01 M KI to the photolyte (compared to the unphotolyzed solution absorbance after adding KI (lower panel). The black area are the unphotolyzed solutions absorbance and red area is the photolyzed solution absorbance in both figures. The solutions contained of 1×10^{-4} M $[\text{Ru}(\text{bpy})_3]^{2+}$ and the acid concentration was 4 M. The solution was irradiated with 405 nm for 30 min. The dilution errors were determined from comparisons of the unphotolyzed solution absorbance with and without KI and averaged to be about 10%. The generation of the photo-product ($[\text{Ru}(\text{bpy})_3]^{3+}$) was accompanied by the oxidation of I^- , and we were not able to determine the stoichiometric relationship between them due to the background absorbancies in the UV region. In addition, the photolysis resulted in a small blue shift in the $\text{bpy}-\pi\pi^*$ absorption at about 250-300 nm.

Table 6. Summary of iodometric yield determinations

[H ⁺], M	[Ru ^{II} B ₃] _{init.} μM	Photolyte Vol., mL	Abs. 405 nm	Irradiation time, min	Δ[Ru ^{II} B ₃] _{de} μM ^a	Δ[Ru ^{II} B ₃] _{rec.} μM ^b	Fraction Recovered ^c	~ 2×[I ₃ ⁻], μM ^d
4.0	76	0.30	0.63	30	32	27	0.85	≥17
4.0	74	0.30	0.62	30	28	23	0.82	≥18
4.0							0.84±0.02	
2.0	35	0.30	0.25	30	14	12	0.86	≥11
2.0	41	0.30	0.34	30	18	12	0.67	≥11
2.0	42	0.30	0.28	30	8	8	1.0	≥4
2.0							0.84±0.17	
0.5	72	0.30	0.57	5	7	9	1.3	≥2
0.5	97	0.30	0.71	10	15	13	0.9	4
0.5	88	0.30	0.68	20	35	40	1.1	≥8
0.5	65	0.30	0.51	20	7	5	0.7	≥4
0.5	55	0.30	0.41	30	13	15	1.1	≥9
0.5	94	0.30	0.73	30	7	10	1.4	≥1
0.5	55	0.30	0.40	30	18	18	1	≥8
0.5	98	0.60	0.74	30	9	10	1.1	≥3
0.5	92	0.30	0.77	60	20	12	0.6	≥13
0.5							1.0±0.3	
0.20	58	0.30	0.44	30	5	3	0.6	≥5
0.20							0.6	
0.10	91	0.60 ^y	0.70	30	8	5	0.62	≥4
0.10	83	0.30	0.54	30	8	6	0.75	≥10
0.10							0.68±0.06	
0.05	63	0.30	0.49	30	7	8	1.1	≥3
0.05							1.1	
0.010	114	0.30	0.85	30	15	14	0.93	≥1
0.010	94	0.30	0.69	30	10	5	0.5	≥12
0.010	63	0.30	0.45	30	5	2.4	0.5	≥5
0.010							0.6±0.3	

^aThe determination of the amount of the photodecomposition from the differences in the amplitude of 452 nm ³MLCT absorption maxima in the spectra of the initial solution and the photolyzed solution. ^b The amount of Ru²⁺ recovery calculated from the difference between 452 nm ³MLCT absorption maxima in the spectra of the initial solution and the photolyzed solution after added 0.3 ml of KI solution; $\epsilon_{\max} = 14,500 \text{ M}^{-1}\text{cm}^{-1}$.⁴¹ ^c The difference between 350 nm MLCT absorption maximum of I₃⁻ ($\epsilon_{\max} = 23,200 \text{ M}^{-1}\text{cm}^{-1}$) in the spectra of the initial solution and the photolyzed solution after each was mixed with an equal volume of 0.010 M KI was used for crude estimate of [I₃⁻]; the 350 nm absorbance in the absence if I₃⁻ is not the same before and after photolysis.

2.3.5. Acid dependence of photodecomposition rate

The initial rate of the photodecomposition was acid dependent for $[\text{Ru}(\text{bpy})_3]^{2+}$ photolysis experiments that were performed under ambient conditions. The photolysis rate, R_{init} , increased about 10-fold when the acid concentration was increased from $[\text{H}^+] = 0.001$ M to $[\text{H}^+] = 4$ M. In addition, the observations of the changes of the initial rate with acid concentration were similar to those in 3mm cuvette and in a 2 mm i.d. cylindrical cell, but the initial rate R_{init} was larger in the cylindrical cell than in the 3 mm cuvette; see Figures 15 and 16 and Table 7. The acid dependence of the initial rate for photodecomposition of $[\text{Ru}(\text{phen})_3]^{2+}$ showed similar trend but R_{init} was smaller compared to $[\text{Ru}(\text{bpy})_3]^{2+}$, with $(R_{\text{init}})_{\text{Ru-phen}} \approx R_{\text{init}}(\text{Ru-bpy})/3$. However, the photodecomposition rate of $[\{(\text{bpy})_2\text{Ru}\}_2\text{pZ}]^{4+}$ complex was acid independent for the range of the acid concentrations used.

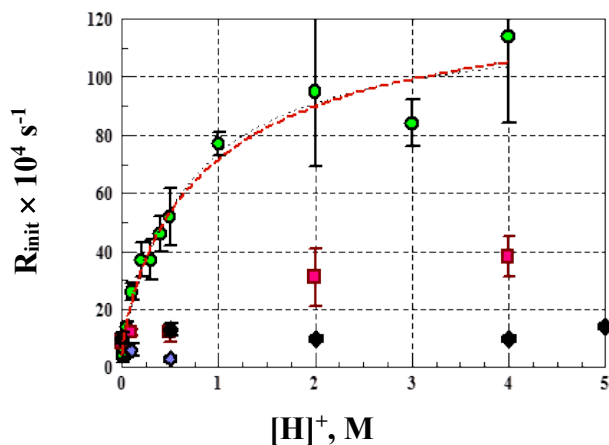


Figure 15. The dependence of the photodecomposition rate on, R_{init} , on acid concentration for various Ru^{II} complexes in ambient aqueous solutions with 0.1 M 2-propanol in a 2 mm cylindrical cell: The green circles is for $[\text{Ru}(\text{bpy})_3]^{2+}$, the red squares are for $[\text{Ru}(\text{phen})_3]^{2+}$ and the black diamonds are for $\{[\text{Ru}(\text{bpy})_2]_2(2,3\text{-dpp})\}$ with the 532 nm irradiation and the light blue diamonds for 405 nm irradiation. The errors are the standard deviations of replicate determinations. The dashed curve is the non-linear least squares fit of eq 2 to the $[\text{Ru}(\text{bpy})_3]^{2+}$ data and the red-dashed curve is the fit of eq 3 for a large number of scavengable ion pair species. The best fit in both cases required a small positive intercept. The data are for from Table 8.

Two models were used for the H^+/e^- scavenging for acids concentration ($[\text{H}^+] > 0.1$ M; section 2.6 1B): The first model for only one ion-pair species scavenged; and the second model for many ion-pair species scavenged. The competition kinetics of the first model predicts that the initial rate of product formation from the H^+/e^- scavenging has the algebraic form in eq 2,

$$R_{\text{init}} \approx (\phi_{\text{U}} G(\lambda)) \frac{[\text{H}^+]}{(f_{\text{R,h}} + [\text{H}^+])} + C \quad (2)$$

Fit to eq 2: $(\phi_U G(\lambda)) \times 10^4 = 114 \pm 8 \text{ s}^{-1}$, $f_{R,h} = 0.7 \pm 0.2 \text{ M}$ and $C \times 10^4 = 6 \pm 4 \text{ s}^{-1}$; where f is the ratio of recombination and scavenging rate constants; ϕ_U is the photoionization quantum

$$\text{yield}; G(\lambda) = \frac{\kappa_{\lambda(S)} \kappa_{\lambda(E)}}{k_{\text{obsd}}} ; \kappa_{(S)} = \varepsilon_{S(\lambda)} d_{\text{pth}} I_{\lambda}^{\circ} ; \kappa_{(E)} = \varepsilon_{E(\lambda)} d_{\text{pth}} I_{\lambda}^{\circ}$$

The origin of this equation is shown in section 2.6. The second idealized model, model 2 considers the possibility that the chemical scavenger used can react with several ion pair species with different recombination rates by treating $f_{R,h}$ as a variable and integrating eq 2 from $f_{R,h} = 0$ to $f_{R,h} = f_{\text{max}}$ resulting in eq 3. The parameters ⁴⁰⁴⁰⁴⁰⁴⁰found for the fit to eq 3 (red dashed curve) shown in Figures 15 and 16 are $(\phi_U G(\lambda)) \times 10^4 = 59 \pm 14 \text{ s}^{-1}$, $f_{\text{max}} = 2.6 \pm 0.6 \text{ M}$ and $C \times 10^4 = 5 \pm 4 \text{ s}^{-1}$.

$$R_{\text{init}} = \phi_U G(\lambda) [H^+] \ln \left(\frac{f_{\text{max}} + [H^+]}{[H^+]} \right) + C \quad (3)$$

Figure 16 expands the low acid range from Figure 15 and the fit to eq 2. That the best fit requires an intercept is consistent with more than one species being scavenged. The initial rate dependence of acid $[H^+]$ for $[\text{Ru}(\text{phen})_3]^{2+}$, Figure 15, was similar to that of $[\text{Ru}(\text{bpy})_3]^{2+}$, however, the initial rate of R_{init} was about $30 \pm 10\%$ of those of the Ru-bpy complex; and this illustrates that $[H^+]/(B + [H^+])$ is about the same for both complexes while $\phi_U G_{\lambda}$ is significantly smaller for the Ru-phen complex. This is consistent with the scavenging behavior being dependent only on the radicals scavenged and not on their origin. In contrast, the initial rate of the photodecomposition of $[\{(bpy)_2\text{Ru}\}_2\text{dpp}]^{4+}$ was acid independent when we irradiate the sample with either 405 or 532 nm lasers which suggests that this complex was not photoionized, and the yield of the product was higher

with 532 nm than with 405 nm irradiation. Thus, this complex might photodecompose through an excited state thermal substitution.

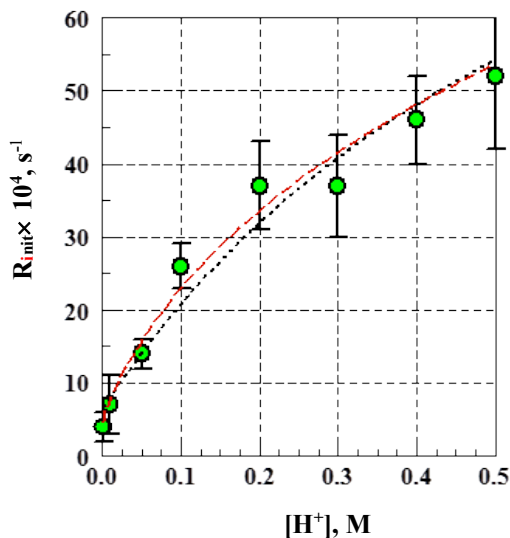


Figure 16. The photodecomposition of $[\text{Ru}(\text{bpy})_3]^{2+}$ at low acid concentration. See the caption of Figure 15 for details.

The scavenging model and the kinetic analysis shown in 2.6 indicates that R_{init} is independent of diffusion and the extrapolation to $t = 0$ eliminates the problems associated with product formation. However, the parameters F_{∞} and k , that result from the fittings to the experimental data by eq 1, are diffusion dependent (section 2.5, eq B19).

$$k \approx R_{\text{init}} + k_{\text{D}} \quad \text{and} \quad F_{\infty} \approx \frac{R_{\text{init}}}{k_{\text{D}} + R_{\text{init}}} \quad (4)$$

Table 7 shows the average experimental value $k_{\text{D}} = (k - R_{\text{init}})$ that was calculated from the experimental observation of the irradiations of $[\text{Ru}(\text{bpy})_3]^{2+}$ in a 2 mm id cell in the acid range of 0.001- 4 M; the diffusion rate values were independent for the $[\text{H}^+] \geq 0.01$ with $k_{\text{D}(\text{ave})} = 25 \pm 7 \text{ s}^{-1}$.

Table 7. Initial rates of $[\text{Ru}(\text{bpy})_3]^{2+}$ photodecomposition resulting from the 405 nm irradiation in acidic 2-propanol solutions in a 2 mm cylindrical cell.

$[\text{H}^+]$, M	k , ^a $\text{s}^{-1} \times 10^4$	F_∞ ^a	$R_{\text{init}} =$ $k \times F_\infty \times 10^4$, ^a s^{-1}	$k_D = k - R$, ^b s^{-1}
0.0001	LSQ fit		2 ± 1 ^c	
0.001	13 ± 1	0.5 ± 0.1	4 ± 2	6 ± 3
0.01	34 ± 5	0.28 ± 0.03	8 ± 2	26 ± 7
0.05	30 ± 4	0.52 ± 0.02	16 ± 2	18 ± 6
0.1	46 ± 5	0.57 ± 0.04	26 ± 3	20 ± 8
0.2	64 ± 9	0.58 ± 3	37 ± 6	27 ± 15
0.3	51 ± 10	0.72 ± 0.07	37 ± 7	14 ± 17
0.4	69 ± 8	0.66 ± 0.01	46 ± 6	23 ± 15
0.5	80 ± 16	0.65 ± 0.03	52 ± 10	28 ± 26
1	114 ± 5	0.69 ± 0.01	77 ± 4	34 ± 9
2	120 ± 30	0.79 ± 0.02	95 ± 26	25 ± 56
3	118 ± 3	0.71 ± 0.04	84 ± 8	34 ± 11
4	143 ± 34	0.80 ± 0.12	114 ± 30	29 ± 64

^a Data were fitted to eq 1, and the values reported are the averages of several determinations; for the experiments that show very little curvature, the F_t vs. t plots fitting using this equation did not converge and we used linear least squares (LSQ) fits. ^b The results based on our kinetic model in section 2.6. The empirical parameter related to the rate of diffusional replacement of the photolyte by bulk solution is expressed as k_D ; $k = R_{\text{init}} + k_D$, our fits resulted in $(k_D)_{\text{ave}} = 25 \pm 7 \text{ s}^{-1}$ for $[\text{H}^+] \geq 0.01 \text{ M}$. ^c The slope of LQS fits.

Table 8. Summary of the fitting^a parameters for the acid dependent $[\text{Ru}(\text{bpy})_3]^{2+}$ photodecomposition rate in various aqueous acidic solutions in a 2 mm cylindrical cell with 405 nm radiation (Ar deaerated).

Laser Wavelength, nm	$[\text{H}^+]$ M	t_0 , s	k , $\text{s}^{-1} \times 10^4$	F_∞	Initial Intensity, $I_{t=0}$ counts	$R_{\text{obs}} =$ $k \times F_\infty \times 10^4$, s^{-1}	LSQ fits $R_{\text{obs}} \times 10^4$, s^{-1b}
405	E-4		LSQ		35000		2
405	E-4				35000		2.5
405	E-4				30300		1
2 ± 1							
405	E-3	59	14 ± 10	0.41 ± 0.22	20300	6 ± 5	

405	E-3	7	14±1	0.52±0.03	20300	7±1	
405	E-3	13	12±1	0.57±0.04	20400	7±1	
Averages			13±1	0.5±0.1		7±2	7±7
405	E-2	18	42±7	0.653±0.005	23000	27±5	
405	E-2	15	50±3	0.59±0.01	23000	30±3	
405	E-2	24	52±1	0.614±0.004	20450	32±1	
Averages			48±5	0.62±0.03		30±4	24±5
405	0.05	21	26±1	0.55±0.02	30000	14±1	10±0.3
405	0.05	24	33±9	0.50±0.01	29000	16±5	12±1
405	0.05	31	31±1	0.52±0.01		16±1	15±1
Averages			30±4	0.52±0.02		16±2	13±1
405	0.1	32	44±0.1	0.566±0.007	27000	25±1	
405	0.1	24	54±2	0.535±0.007	26000	29±2	
405	0.1	22	40±1	0.62±0.01	29000	24±1	
Averages			46±5	0.57±0.04		26±3	
405	0.2	24	59±2	0.61±0.007	30200	36±2	
405	0.2	24	59±3	0.55±0.01	29500	32±2	
405	0.2	29	75±4	0.568±0.004	30000	43±2	
Averages			64±9	0.58±3		37±6	27±6
405	0.3	23	60±0.9	0.65±0.004	20700	39±1	
405	0.3	27	41±4	0.78±0.04	20300	32±2	
405	0.3	25	51±1	0.725±0.003	20400	37±1	
Averages			51±10	0.72±0.07		37±7	29±5
405	0.4	28	61±2	0.67±0.007	30000	41±3	
405	0.4	30	77±2	0.647±0.005	29000	50±2	
Averages			69±8	0.66±0.01		46±6	36±5
405	0.5	22	88±2	0.640±0.002	28500	56±2	
405	0.5	58	57±2	0.704±0.006	17000	40±3	
405	0.5	31	70±2	0.690±0.007	28500	48±2	
405	0.5	30	88±2	0.644±0.004	27000	57±2	
405	0.5	28	98±3	0.622±0.008	29000	61±2	
Averages			80±16	0.65±0.03		52±10	38±3
405	1	27	109±2	0.677±0.003	29000	74±2	
405	1	24	113±3	0.700±0.005	30000	79±3	
405	1	23	119±2	0.682±0.003	30000	81±2	
Averages			114±5	0.69±0.01		77±4	51±1
405	2	20	96±2	0.800±0.004	34000	77±2	
405	2	24	97±3	0.768±0.004	28000	74±3	
405	2	23	154±4	0.791±0.003	30000	121±4	
Averages			120±30	0.79±0.02		95±26	60±10
405	3	26	116±3	0.65±0.04		75±3	
405	3	22	117±4	0.684±0.003		80±3	
405	3	25	122±5	0.700±0.003		85±4	
Averages			118±3	0.71±0.04		84±8	

405	4	28	132±3	0.870±0.004	30000	144±5	
405	4	29	182±4	0.860±0.003	30000	156±5	
405	4	26	116±3	0.655±0.004	30000	76±2	
Averages			143±34	0.80±0.12		114±30	

^a Photodecomposition data fitted to eq 1; ^bLSQ fits in parentheses.

2.3.6. Superimposed dual laser irradiations

a. Irradiation with dual 405 & 532 nm irradiation in 2 mm cylindrical cell

The observed rate the photodecomposition of $[\text{Ru}(\text{bpy})_3]^{2+}$ 532 and 405 nm lasers superimposed is much larger than the 405 nm alone or the weighted sum of photolysis rates found for the individual lasers. The calculated values of R_{int} obtained in 2 mm i.d. cylindrical cells were about 5 times larger than those obtained in the 3 mm i.d. cuvette. Argon gas deaeration resulted in doubling of the initial rate, R_{int} , which is in proportion to the increase in the photo-stationary state concentration of $^3\text{MLCT}$. Greater rate of intensity decrease observed for the superimposed lasers resulted from the two-photon dependence of the photodecomposition. The larger values of R_{int} and the cylindrical cell were a result of curvature which resulted in some focusing of the laser beam width, decreasing the effective photolysis volume and increasing the photon density within the photolysis volume.

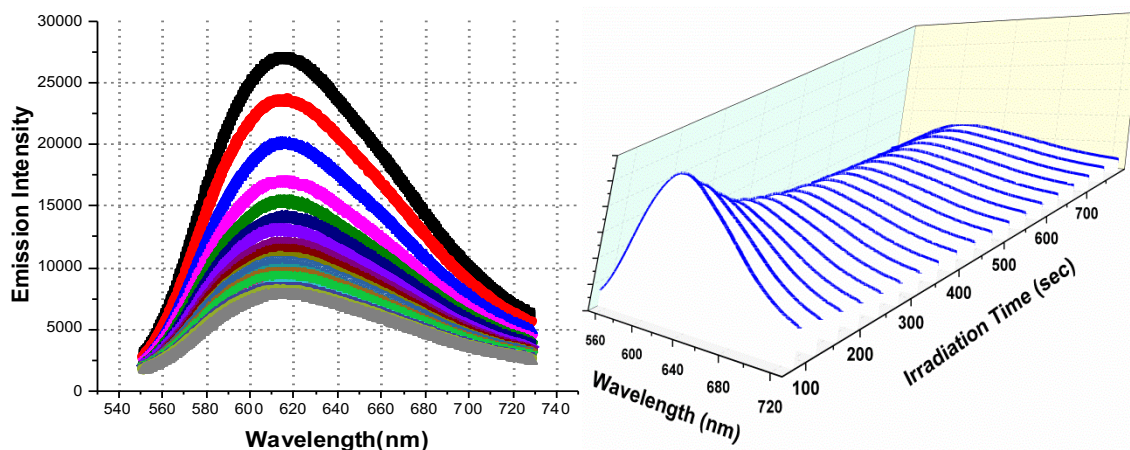


Figure 17. The changes in $^3\text{MLCT}$ emission intensity that accompany irradiation of $[\text{Ru}(\text{bpy})_3]^{2+}$ with superimposed 405 & 532 nm laser beams. The left panel shows the superimposed variations of the spectral scans as a function of irradiation time and the right panel shows the spectral scan variations displayed as the kinetic mode output. The solutions contained 0.5 M acid, 0.1 M 2-propanol and initial concentrations of $[\text{Ru}(\text{bpy})_3]^{2+} = 1.0 \times 10^{-4}$ M. The irradiation times represented start at 117 s (which excludes the time for opening the shutter; the kinetic mode timing is internal in the spectrometer software) with spectral scans at 39 s intervals and 13 min total time of irradiation. The experimental data points were obtained as the intensities of the kinetic mode spectral scans.

An example of the observed changes in the $[\text{Ru}(\text{bpy})_2]^{2+}$ emission spectrum with irradiation time using overlapped 405 and 532 nm lasers in 3 mm cuvette cell is shown in Figure 18. The emission energy maximum or the band shape do not change when the intensity changed. Also displayed in Figure 18 are the emission spectral intensity changes that are observed for this complex using 405 nm excitation only. The emission intensity (in counts per second) on the Y-axis was determined in EXCEL as the average intensity of each spectral scan, $I_{\text{ave}} = \left(\sum_{\lambda} I_{\lambda} \right) / N_{\lambda}$ (I_{λ} the intensity recorded at wavelength λ ; N_{λ} the number of wavelength increments, about every 3 nm, in the EXCEL record of the scan).

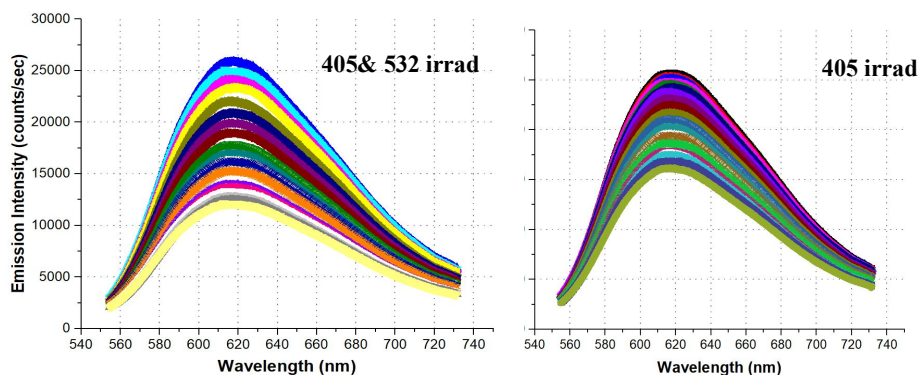


Figure 18: Experiments illustrating the contrasting fractional decreases in $^3\text{MLCT}$ emission intensity induced by the simultaneous 532 and 405 nm laser irradiations of $[\text{Ru}(\text{bpy})_3]^{2+}$ in ambient acidic solution with those of the 405 nm laser alone in a 3 mm id cuvette (13 min total irradiation time): superimposed 532 and 405 nm laser beams in the left panel and 405 nm laser only in the right panel. The conditions and procedures are as described in the caption of Figure 17.

Table 9. Summary of the calculated initial rate of the photodecomposition of [Ru(bpy)₃]²⁺ in a 3 mm id cuvette cell with individual 405 and 532 or the laser beams superimposed.

Complex ^a	Conditions			λ Irradiation, nm	Average	
	[TFA], M	[2-propanol], M	other		10 ⁴ ×R _{in} , ^b s ⁻¹	
[Ru(bpy) ₃] ²⁺	0.5	0.1		532	-1.0±0.3	
				405	3.6±1	
				532&405	8.0±1.0	
				532	-0.8±0.5	
				405	4.5±1.7	
				532&405	5.5±0.8	
[Ru(bpy) ₃] ²⁺ ^d	0.5	0.1	30% I ₀ ^c	532&405	12±4	
				405	1.5±1.2	
				532&405	1.9±0.3	
[Ru(bpy) ₃] ²⁺				QTH	2.6±0.4	
				560nm cutoff filter	QTH	0.6±0.1
[Ru(bpy) ₃] ²⁺				Ar Deaerated	405	6.9±0.6
	O ₂ saturated	405	3.9±0.1 ^g			
	Ar Deaerated	532	0.008±0.004			
	O ₂ saturated	532	-0.7±0.5			
[Ru(bpy) ₂ (CN) ₂]	0	0	0.5 M acetone	532	-0.22±0.05	
				405	8±1	
				532&405	12±1	

^a Ambient solutions in a 3 mm square fluorescence cell with [Ru(bpy)₃]²⁺ = 1.0×10⁻⁴ M except as indicated. The measured cw laser power outputs were 46±2 mW (405 nm laser) and 139±5 mW (532 nm laser). ^b Average calculated initial using LSQ fits. ^c 30% neutral density filter. ^d 0.55×10⁻⁴ M [Ru(bpy)₃]²⁺.

The initial photolysis rates for these experiments were calculated using the least square fits, the initial few points of the fraction of the product formed after the shutter was open up to 300 second were chosen for the fits.

2.3.7. Ambient condition photolysis of $[\text{Ru}(\text{bpy})_3]^{2+}$ with the quartz halogen tungsten lamp (QTH) lamp

An example of the emission changes of $[\text{Ru}(\text{bpy})_2]^{2+}$ with the QTH lamp in ambient condition in a 3 mm cuvette cell, a cut off filter that cuts before 558 nm was used in the front of liquid light guide. The cell was placed at about 45° to the laser beam to minimize the scattered light. The result of this irradiation is shown in Figure 19. The initial rates of the photodecomposition calculated from least square fits are shown in Table 10.

Table 10. Summary of the calculated initial rate of the photodecomposition of $[\text{Ru}(\text{bpy})_3]^{2+}$ in a 3 mm cuvette using QTH as irradiation source under ambient condition.

Code	Laser Wavelength, nm ^a	Initial Intensity, I _{t=0} counts/s ^b	Initial rate $10^4 \times dF/dt$, s ^{-1c}	r ²	Special Conditions
MA145	QTH	8,320	2.6 ± 0.4	[0.92]	RuB ₃
MA146	QTH w/uv filter	10,870	0.6 ± 0.03	[0.99]	RuB ₃

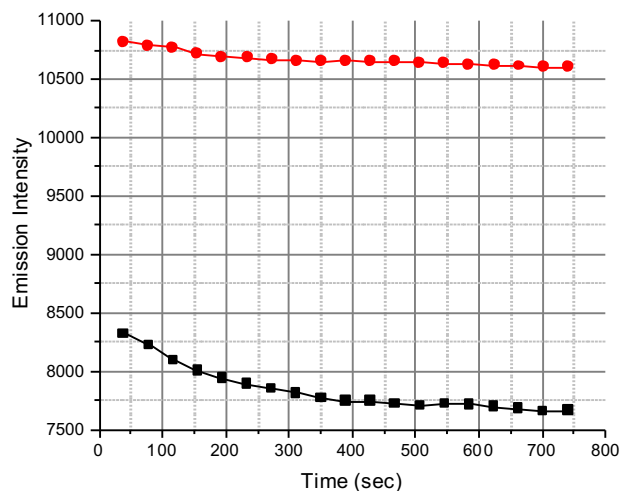


Figure 19. Observed photochemistry of 10^{-4} $[\text{Ru}(\text{bpy})]^{2+}$ in aqueous solution with 0.5 M trifluoroacetic acid and 0.1 M 2-propanol using QTH lamp as irradiation source at ambient condition. Red line is the variation of the emission intensity with a < 558

nm cut off filter. The black line is the variation of the emission intensity without using the cut off filter.

2.3.8. Comparison of the absorption spectra of the $[\text{Ru}(\text{bpy})_3]^{2+}$ ground state and $^3\text{MLCT}$ excited state to the relative intensity distributions in the global solar spectrum and QTH lamp spectra

The net photoionization yields are more significant when a combination of long and short wavelength visible radiation is used, the relative amounts of QTH radiation absorbed by the ground state; less than ten percent of the light absorbed by the $[\text{Ru}(\text{bpy})_3]^{2+}$ $^3\text{MLCT}$ excited state results in most of the photoionization, and the visible radiation can be absorbed by the ground state to generate more $^3\text{MLCT}$ that can be ionized by 405 nm radiation. Thus, it should be possible to achieve a significant photoionization with any broadband irradiation of a substrate such as $[\text{Ru}(\text{bpy})_3]^{2+}$ if the absorption of both the ground and excited state overlap with that radiation; see Figure 20.

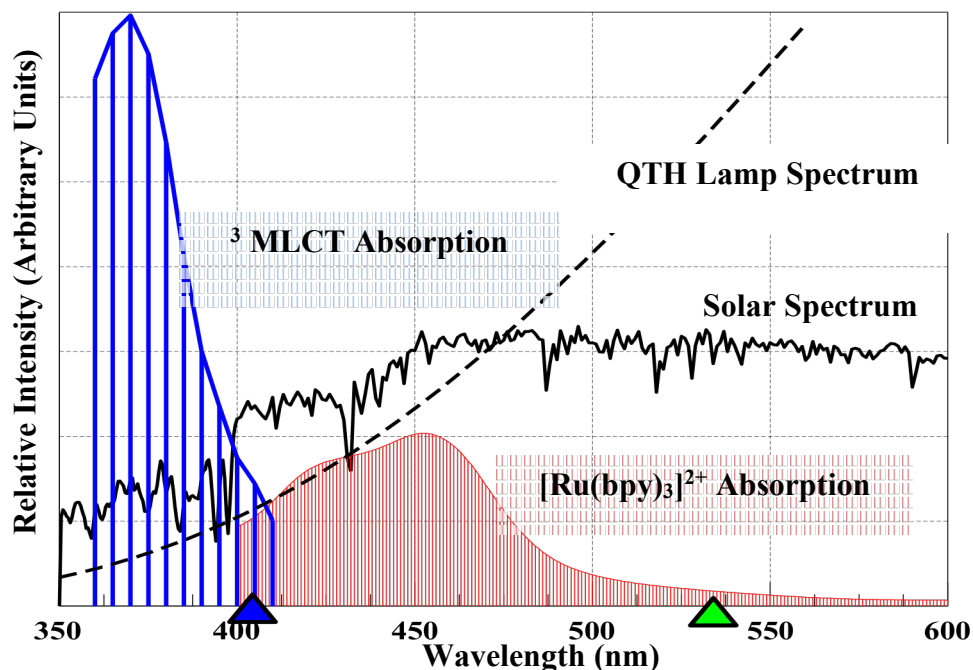


Figure 20. Comparison of the absorption spectra of the ground state and $^3\text{MLCT}$ excited state of $[\text{Ru}(\text{bpy})_3]^{2+}$ to the relative intensity distributions in the global solar and QTH lamp spectra. The green triangles represent the 532 nm and blue is for 405 nm. The amplitudes of the spectra have been adjusted for convenient comparison; the $^3\text{MLCT}$ absorptivity at 405 nm is about three times that of the ground state. The standard global solar spectrum was downloaded from PVEducation.org, (www.pveducation.org/pvcdrom/appendices/standard-solarspectra) as an EXCEL file.

2.3.9. Estimates of photoionization quantum yields. We were able to estimate the quantum yields of scavengeable electrons and the fits of eqs 2 and 3 provide slightly different estimates of $(\phi_e^-)G(\lambda)$, these estimates are in Table 11; the parameters used in these estimates are in Table 12.

Table 11. Photoionization quantum yield estimates

Parameter	Model	
	Single Ion Pair	Many Ion Pairs
$f_{R,h}$, M	0.7 ± 0.2^a	2.1 ± 0.6^b
ϕ_U ($[H^+] = 0.5$ M)	0.026 ± 0.002^c	0.013 ± 0.006^d
ϕ_{e^-} (free only) ^e	~ 0.003	~ 0.001

^a Value used in calculation from fit of eq 2 to data in Table 8. ^b Value used in calculation from fit of eq 3 to data in Table 8. ^c From R_{init} in a 3 mm cuvette (Table 9) and

$$\phi_{U(h)} = \frac{(f_{R,h} + [H^+])}{[H^+]} \frac{R_{init}}{G(\lambda)} \quad (\text{eq 2}). \quad \text{d From } R_{init} \text{ in a 3 mm cuvette (Table 9) and}$$

$$\phi_{U(m)} = \frac{R_{init}}{\ln\left(\frac{f_{max} + [H^+]}{[H^+]}\right) [H^+] G(\lambda)} \quad \text{e Based on the ratio of the average of } R_{init} \text{ for } [H^+] = 0.001$$

and 0.01 M ($R_{ave} = 0.0006 \text{ s}^{-1}$) to $R_{init} = 0.0052 \text{ s}^{-1}$ for $[H^+] = 0.5$ M (data from Table 8).

Table 12. Parameters for quantum yield estimate of $[Ru(bpy)_3]^{2+}$ ^a

Parameter	S_0		3MLCT	
	532	405	532	405
I_{λ}^0 , ein $s^{-1} \times 10^7$	6.3	1.56	6.3	1.56
V_{phot} , μL ^b		2.4	≈ 2	
I_{λ}^0 , ein/L-s ^c		0.065	0.32	0.09
$\epsilon_{X(\lambda)}$, $M^{-1} cm^{-1}$ ^d	1330	7330	< 1000	22,200
d_{pth} , cm	0.3			
k_{obsd} , μs^{-1} ^e	2.6 (aerated)			
Irradiation at:	405 nm only		(405 + 532)	
$\kappa_{\lambda(S)}$, s^{-1e}		140	(130) ^f	
$\kappa_{\lambda(E)}$, s^{-1e}			< 90	500
$G(\lambda)$ ^g		0.027	0.025 ^f	
R_{init} , $s^{-1} \times 10^4$ (0.5 M H^+) ^h		4 ± 1	8 ± 2	
ΔR , $s^{-1} \times 10^4$ (0.5 M H^+) ^h			5 ± 2 ⁱ	

^a Solutions contain $[H^+] = 0.5$, and 0.1 M 2-propanol. ^b The intersection volume of photolysis: the 405 nm laser beam volume that passed through the cell and the intersection volume of the two beams in the dual beam experiments. ^c The photons/sec in the photolysis volume. ^d From $[Ru(bpy)_3]^{2+}$ absorption spectrum and analysis of excited state spectra.⁴¹⁻

⁴² $\epsilon_{\lambda(X)} = \epsilon_{X(\lambda)} d_{pth} I_{\lambda}^0$. ^f For the superimposed lasers. ^g $G(\lambda) = \frac{k_{\lambda(S)} k_{\lambda(E)}}{k_{obsd}}$. ^h From Table 9. ⁱ

For the amount of ³MLCT generated by 532 nm irradiation and photolyzed by 405 nm

radiation. ^j $\phi_{U(h)} = \frac{(f_{R,h} + [H^+])}{[H^+]} \frac{R_{init}}{G(\lambda)}$; $f_{R,h} \approx 1$.

2.3.10. Preliminary observations of the photolysis of various ruthenium complexes under ambient conditions.

Some preliminary photochemical studies of the $[Ru(phen)_3]^{2+}$, $[{(bpy)_2Ru}_2dpp]^{4+}$ (dpp = 2,3-(dipyridyl)pyrazine) and $[Ru(bpy)_2(CN)_2]$ complexes were made with the same photolysis procedure as in section 2.3.6 (a) in the experimental, and the acid concentrations ranging from 10^{-3} - 4 M for the first two complexes. No acid was used in the photolysis of $[Ru(bpy)_2(CN)_2]$. The photodecomposition yields were found to be small for all complexes, but behavior similar to that of $[Ru(bpy)_3]^{2+}$ was found only for the $[Ru(phen)_3]^{2+}$ complex; the Ru-dpp complex shows an acid independent photochemistry. The photolysis rates of Ru-dpp complex were larger for 532 nm than for 405 nm irradiations, see Figure 21 for the observations. The initial rate data are summarized in Tables 13 and 14.

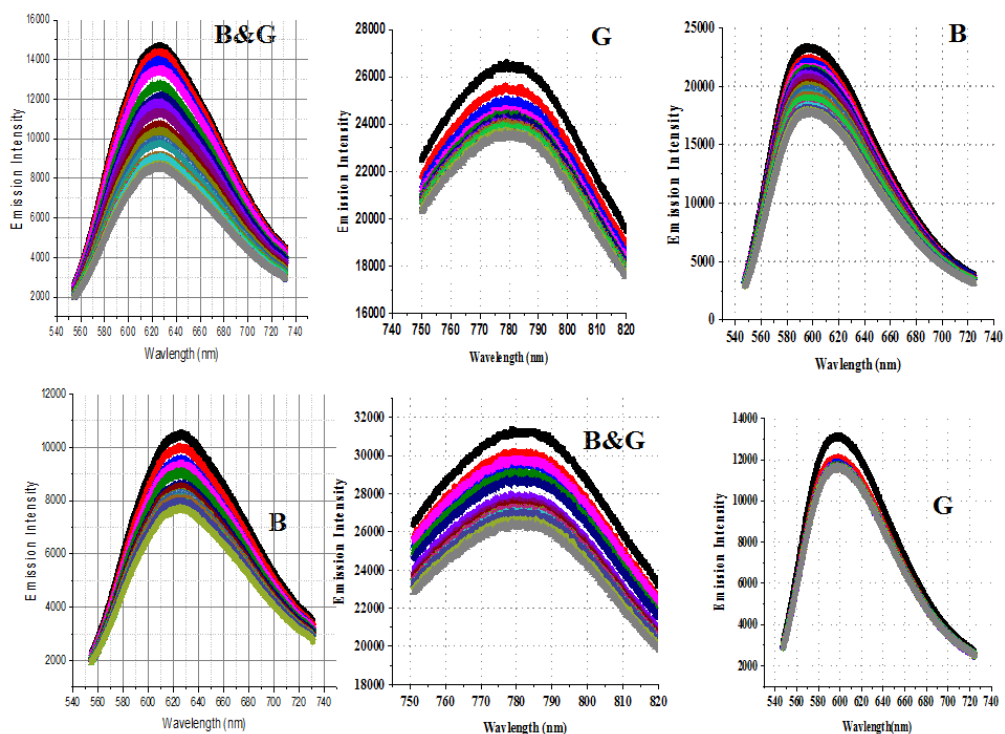


Figure 21. Ambient condition photolysis of $[\text{Ru}(\text{bpy})_2(\text{CN})_2]$, $[\{\text{Ru}(\text{bpy})_2\}_2(2, 3\text{-dpp})](\text{PF}_6)_4$, and Tris(1,10-phenanthroline) ruthenium(II). The photolysis solution contained $2 \times 10^{-4} \text{M}$ $[\text{Ru}(\text{bpy})_2(\text{CN})_2]$, 0.5 M acetone. The photolysis of $[\{\text{Ru}(\text{bpy})_2\}_2(2, 3\text{-dpp})](\text{PF}_6)_4$, and Tris(1,10-phenanthroline) ruthenium(II) contain $10 \times 10^{-4} \text{M}$ complex and 0.1 M 2-Propanol, and 0.5 M triflic acid. The irradiation of $[\text{Ru}(\text{bpy})_2(\text{CN})_2]$ was done in 3 mm cuvette, while the irradiation of $[\{\text{Ru}(\text{bpy})_2\}_2(2, 3\text{-dpp})](\text{PF}_6)_4$, and Tris(1,10-phenanthroline) ruthenium(II) were done in a 2 mm cell.

2.3.11. Fitting parameters of other complexes

Table 13. Summary of fitting parameters for Tris(1,10-phenanthroline) ruthenium(II) photodecomposition rate in various aqueous acidic solutions in a 2 mm cylindrical cell with 405 nm radiation (Ar deaerated).^a

Code	λ , nm	$[H^+]$, M	k , $s^{-1} \times 10^4$	F_{∞}	$k \times F_{\infty} \times 10^4$, s^{-1}
MA620D	405	0.001	123±4	0.0707±0.005	8.7±0.4
[Ru(phen) ₃] ²⁺ Average	405	0.001	123±2	0.0707±0.005	8.7±0.4
MA615 (A)	405	0.1	LSQ		(5±1)
MA615(B)	405	0.1	23±2	0.55±0.08	12±1
[Ru(phen) ₃] ²⁺ Average	405	0.1	23±2	0.55±0.08	12±1
MA376	532	0.5	82±3	0.160±0.003	13±1
MA342	405	0.5	53±6	0.243±0.002	13±2
MA616 (A)	405	0.5	20±2	0.55±0.04	11±2
MA616 (B)	405	0.5	33±2	0.37±0.01	12±3
[Ru(phen) ₃] ²⁺ Average	405	0.5	26±6	0.46±0.09	12±3
MA617 (A)	405	2	94±4	0.380±0.004	36±4
MA617 (B)	405	2	106±3	0.247±0.002	26±3
[Ru(phen) ₃] ²⁺ Average	405	2	100±6	0.31±0.07	31±10
MA627A	405	4	104±3	0.437±0.003	45±3
MA627B	405	4	80±3	0.389±0.003	31±2
[Ru(phen) ₃] ²⁺ Average	405	4	92±12	0.413±0.024	38±7

^a Data fitted to: $F = F_{\infty}[1 - \exp(-k(t - t_0))]$; LSQ fits in parentheses.

Table 14. Fits of photodecomposition rates found for 405 and 532 nm irradiations of $[(\text{bpy})_2\text{Ru}]_2(2,3\text{-}(\text{dipyridyl})\text{pyrazine})$.^{4+a}

Code	λ , nm	$[\text{H}^+]$, M	k	F_∞	t_0	R_{init}^b
620b	532	0.001	163(4)	0.0715(3)	28	12±1
620c	532	0.001	123(4)	0.0707(5)	27	9±1
Average						10±2
623b	405	0.1	391(111)	0.015(1)	28	6±2
Average						6±2
243	405	0.5	52(5)	0.0309(5)	107	1.6±0.2
623a	405	0.5	166(17)	0.0223(1)	16	3.7±0.4
623c	405	0.5	169(13)	0.0211(6)	26	2.6±0.3
Average						2.6±0.7
242	532	0.5	89(7)	0.099(1)	75	9±1
615	532	0.5	206(8)	0.0756(3)	17	16±1
615	532	0.5	174(4)	0.0752(3)	30	13±1
Average						13±2
616a	532	2	149(5)	0.077(4)	25	11±1
616b	532	2	118(4)	0.80(1)	35	9.5±0.3
Average						10±1
620	532	4	179(3)	0.0588(19)	29	10.5±0.8
620d	532	4	150(5)	0.0684(5)	32	10±1
Average						10±1
250	532	5	165(14)	0.085(1)	12	14±1

^a We have used equation 1 for the fits summarized in this table, and LSQ fits for those experiments that show small curvature. ^b Expected ratio for 1st order in light intensity:

$$\frac{R_{532}}{R_{405}} = \frac{(1 - e^{-\text{Abs}(532)})}{(1 - e^{-\text{Abs}(405)})} \times \frac{I_{532}^0}{I_{405}^0} = \frac{(1 - e^{-0.392})}{(1 - e^{-0.216})} \times \frac{139}{46} = \frac{0.324}{0.194} \times \frac{139}{46} = 5.0. \text{ Observed ratio for}$$

$$[\text{H}^+] = 0.5 \text{ M: } \frac{R_{532}}{R_{405}} \approx \frac{13}{2.6} = 5 \pm 3$$

If the observed acid-independent photodecomposition of the Ru-dpp complex were first order in light intensity and due to a ³MLCT thermal reaction, then the relative rates at 532 and 405 nm should be equal to the ratio of the intensities of light absorbed at the two wavelengths.

2.3.12. Absorption spectra of ruthenium complexes.

a. Ambient absorption of [Ru-Tris-1, 10-(1,10-phenanthroline)] complex

Figure 22 represents the ambient UV-vis absorption for the 10^{-4} M [Ru-Tris-1, 10-(phenanthroline)] complex in aqueous solution, 0.5 M triflic acid and 0.1 M Iso-propanol, this complex has $^3\text{MLCT}$ absorption has band at 470nm.

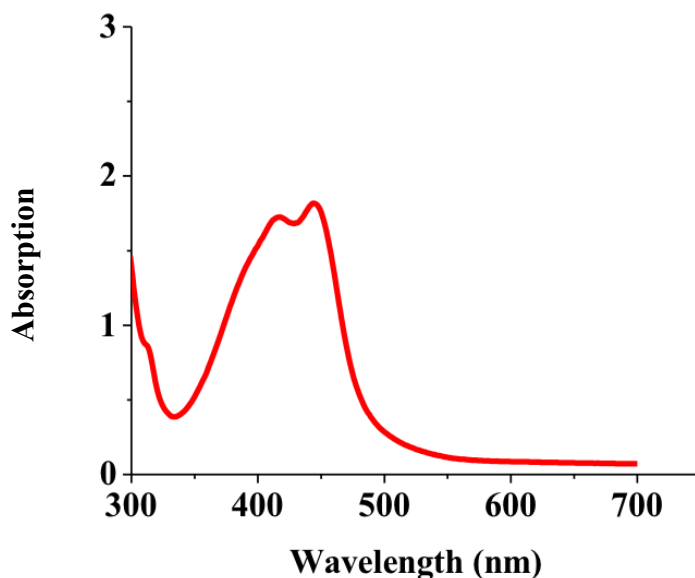


Figure 22: Ambient absorption of 10^{-4} [Ru-Tris-1, 10-(phenanthroline)] in 0.5 M triflic acid and 0.1 M Iso-propanol in 4:1 Ethanol: Methanol.

b. Ambient absorption of [(Ru(bpy)₂)₂-2, 3-dpp] complex

The ambient UV-vis absorption for the 10^{-4} M [(Ru(bpy)₂)₂-2, 3-dpp] complex in butyronitrile, this complex has $^3\text{MLCT}$ absorption band at 530 nm.

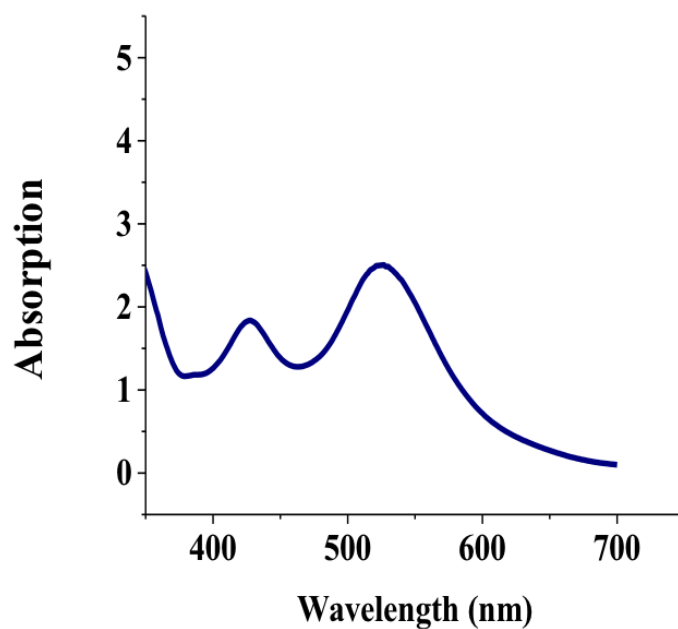


Figure 23: Ambient absorption of 10^{-4} [(Ru(bpy)₂)₂-2,3-dpp] complex in butyronitrile

2.3.13. Emission spectra of ruthenium complexes.

a. 77 K emission spectrum of [(Ru(bpy)₂)₂-2,3-dpp]⁴⁺

The 77 K emission of [(Ru(bpy)₂)₂-2,3-dpp]⁴⁺ contains vibronic structure at 790 nm and this vibronic band is well resolved at 77K; this vibronic structure is not resolved in the ambient emission.

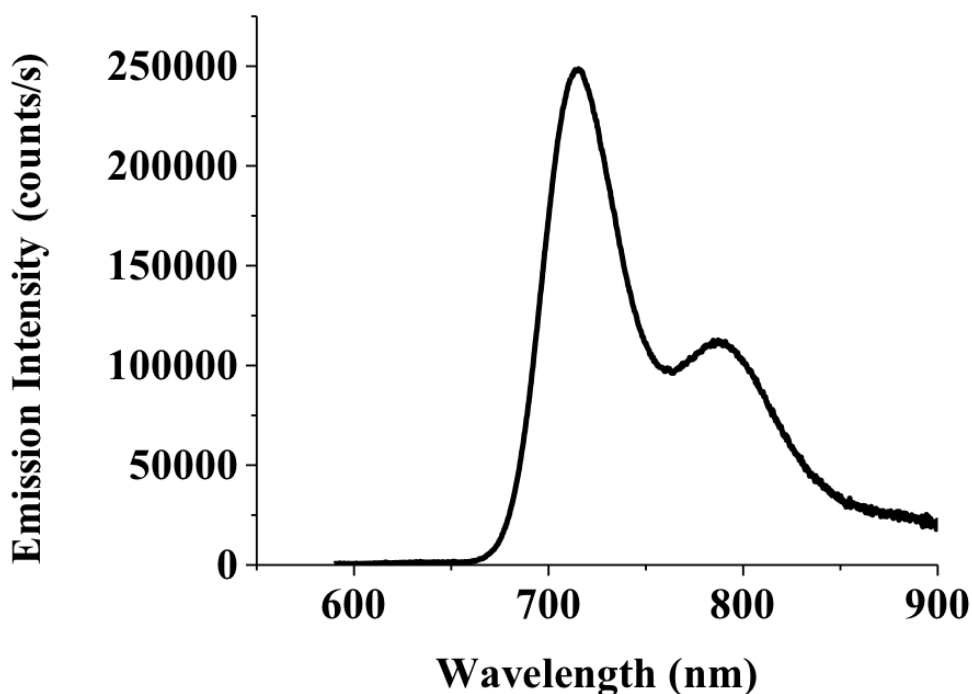


Figure 24. 77 K emission spectrum of $[(\text{Ru}(\text{bpy})_2)_2\text{-}2,3\text{-dpp}]^{4+}$ in butyronitrile

2.3.14. Excited state lifetimes

a. Ambient and 77 K lifetimes

The ambient emission decay for $[\text{Ru}(\text{bpy})_3]^{2+}$ in various aqueous solutions is shown in Figure 25. The decay measurement was done with mono exponential fit. In this experiment we used a control of aqueous solution of 10^{-4} $[\text{Ru}(\text{bpy})_3]^{2+}$ and we varied the acid and 2-Propanol concentrations in some experiments to compare the effect of the scavengers on the life-times of the complex. All measurements were done using cut off filter that cuts <470 nm excitation, and the emission decay was monitored at 610 nm. The lifetime of the three measurements was averaged the same to each individual measurement.

Example of the observed emission decays are shown in Figure 25-27 and summarized in Tables 15 and 16.

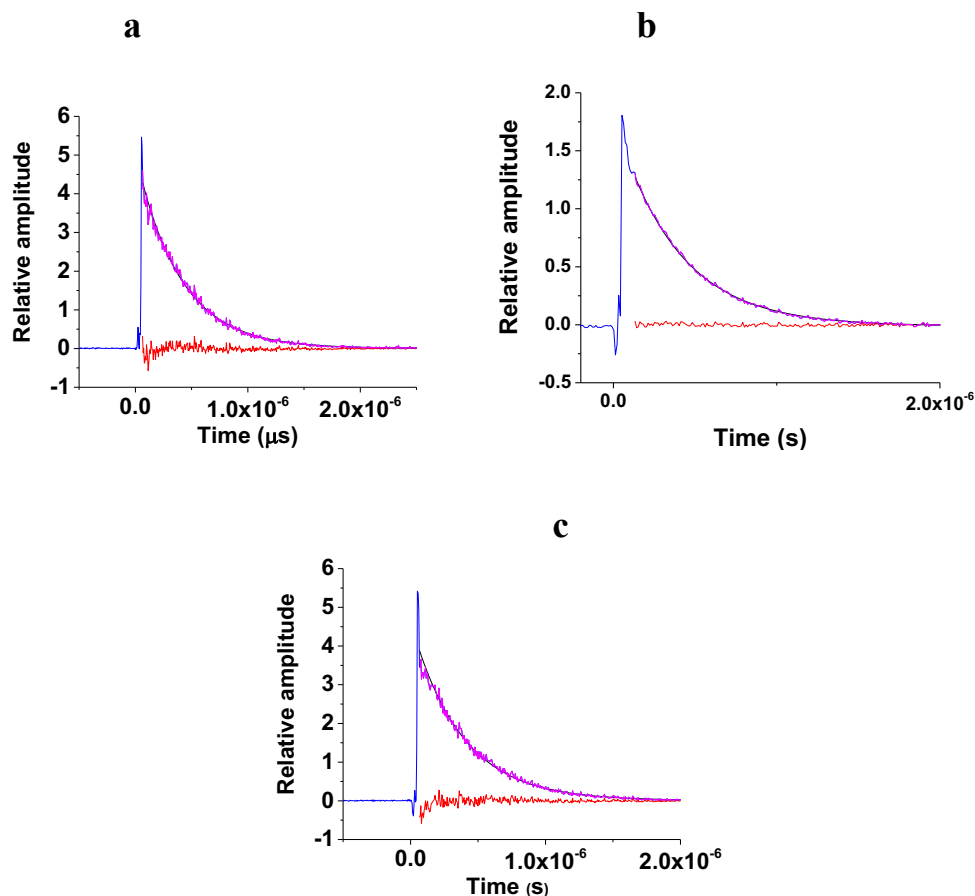


Figure 25. Emission decay of $[\text{Ru}(\text{bpy})_3]^{2+}$ in aqueous solution using 337 nm pulsed excitation monitored at 610 nm. The mono exponential fit (black) and the extracted data (pink) are indistinguishable; residuals are in red, the raw data shows in blue. (a) monoexponential fit for an aqueous solution of 10^{-4} $[\text{Ru}(\text{bpy})_3]^{2+}$ in 0.1 M 2-Propanol and 0.5 M trifluoroacetic acid; (b) fits for an aqueous solution of 10^{-4} $[\text{Ru}(\text{bpy})_3]^{2+}$ (control); (c) emission decay fits for an aqueous solution of 10^{-4} $[\text{Ru}(\text{bpy})_3]^{2+}$ with 0.1 M 2-Propanol.

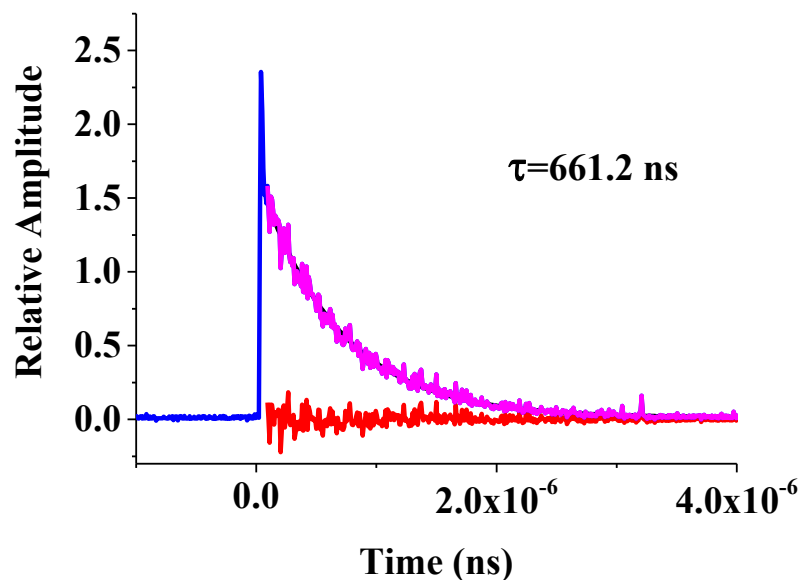


Figure 26. Ambient Emission decay of 10^{-4} M [Ru-Tris-1,10-phenanthroline] in 0.5 M aqueous acidic solution and 0.1 M Iso-propanol, emission decay was monitored at 470 nm.

The ambient emission life-times of [Ru-tris-1,10-phenanthorine] were quite long in solutions dereated with argon, and the decays were fitted to single exponentials. All measurements were done using a cut-off filter in the front of the PMT that cuts < 470 nm excitation and the emission decay was monitored at 610 nm. The solution conditions are shown in the caption of Figure 26.

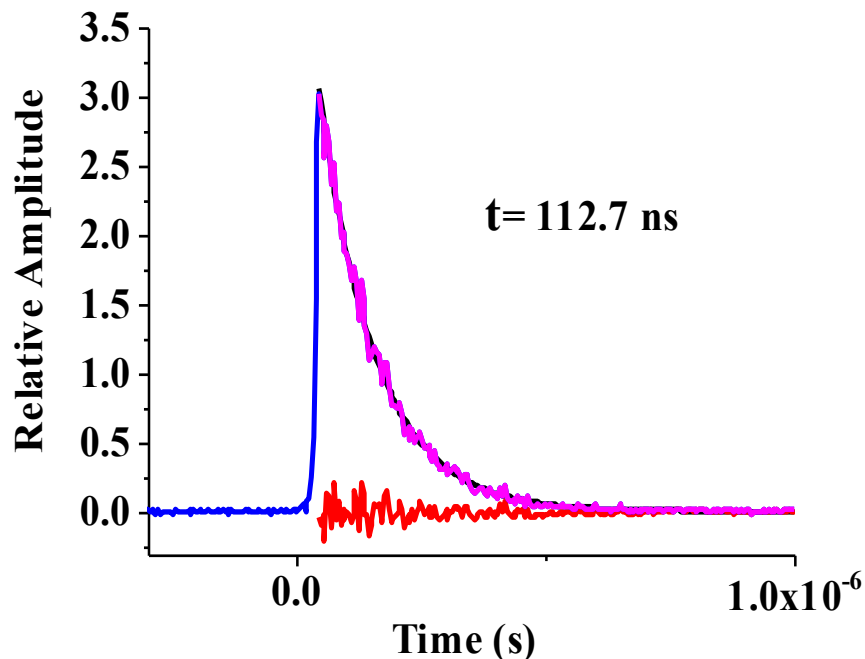


Figure 27. 77 K Emission decay of $[(Ru(bpy)_2)_2(2,3-dpp)]$ in acetonitrile, emission decay was monitored at 530 nm.

The 77 K emission decay of $[(Ru(bpy)_2)_2(2,3-dpp)]$ in acetonitrile is shown in Figure 27. The decay measurement was done with mono exponentials fit, cut off filter was used to cut the excitation wavelength and the emission decay was monitored at 710 nm.

b. The effect of oxygen on the observations. The effects of dissolve oxygen on the observations were investigated. Based on the observed results, it was found that the dissolved O_2 quenched the 3MLCT excited state and reduced its lifetime. The results are summarized in Table 15.

Table 15. Initial photodecomposition rates and emission lifetimes for solutions of $[\text{Ru}(\text{bpy})_3]^{2+}$ in a 2 mm cylindrical cell with different amounts of oxygen.^a

$R_{\text{obs}} \times 10^4, \text{ s}^{-1}$	$\tau_{\text{obs}}, \text{ ns}$	Comments
$45 \pm 5^{\text{b}}$	534 ± 2	deareated
22 ± 4	380 ± 1	aereated
$-5 \pm 3^{\text{c}}$	179 ± 1	O_2 saturated

^a Aqueous solutions with $1.0 \times 10^{-4} \text{ M}$ $[\text{Ru}(\text{bpy})_3]^{2+}$, 0.5 M TFA, 0.1 M 2-propanol

c. Medium dependence of the lifetime

Table 16. Life-time data for $[\text{Ru}(\text{bpy})_3]^{2+}$ and $[\text{Ru}(\text{bpy})_2(\text{CN})_2]$ for the experimental conditions employed.

Complex	[TFA], M	[2-propanol], M	$\tau_{\text{ave}}(\text{X}),$ μs^{b}
$[\text{Ru}(\text{bpy})_3]^{2+ \text{a}}$	0	0	0.377(4)
	0.5	0.1	0.392(4)
	0	0.1	0.373(4)
Overall Average:			0.38(1)
$[\text{Ru}(\text{bpy})_2(\text{CN})_2]^{\text{c}}$	0	0	0.17(1) ^d

^a Dye laser excitation wavelength at 470 nm; monitored at 610 nm; aqueous solutions with 10^{-4} M $[\text{Ru}(\text{bpy})_3]^{2+}$. ^b Average of three life-time determinations; standard deviation (in the last digit) in parenthesis. ^c Dye laser excitation wavelength was 431 nm; aqueous solutions with $1.2 \times 10^{-4} \text{ M}$ $[\text{Ru}(\text{bpy})_2(\text{CN})_2]$. ^d Overall average of 3 determinations.

Table 17. Summary of the initial rates determined for superimposed 532 and 405 nm, individual 405 and 532 nm laser irradiations in 3 mm cuvette using the linear fit for [Ru(bpy)₂(CN)₂]; complexes in aqueous solutions; ambient conditions.

Code	Laser Wavelength, nm ^a	Initial Intensity, I _{t=0} counts/s ^b	Initial rate 10 ⁴ ×dF/dt, s ^{-1c}	r ²	Special Conditions
MA118	532	1,870	-0.22±0.05	[0.74]	RuB ₂ (CN) ₂
MA117	405	10,300	7.9±0.3	[0.99]	RuB ₂ (CN) ₂
MA119	532+405	8,300	12±1	[0.9]	RuB ₂ (CN) ₂

^aFits performed in the Origin program. ^b In counts/sec. ^cLSQ = least squares fit, error limits are one standard deviation; Initial rate estimates based on fits of the initial points after the shutter is open. The numbers in the square brackets are the correlation coefficients (r²).

The initial rate of [Ru(bpy)₂(CN)₂] complex was calculated using the least square fits, the initial few points of the fraction of the product formed at time where the shutter was open to 300 second were chosen for the linear fits.

2.3.15. Diffusion effects.

The effect of diffusion has also been examined for photolysis in the 3 mm id cuvette (see Table 18). For the evaluation of the effect of diffusion in the 3 mm cuvette we used the observed emission intensities before (bef) and after (aft) shuttering the 405 nm laser: $\Delta I_D = I_{aft} - I_{bef}$, I_{bef} was the last point of a regular photolysis sequence with time t_{bef} , I_{aft} was the first point of the next regular photolysis sequence; $\Delta t = t_{aft} - t_{bef}$, t_{bef} determined as time of the last reading before the shutter started to close; alternatively Δt was determined as the time interval between the half closed and half opened shutter as illustrated in this figure. It is assumed that the effect of diffusion is to replace the photodecomposed substrate and that the rate for this process (k_D) is directly proportional to the difference between the

concentration of substrate in the photolysis region and the bulk solution; this is determined in terms of the intensity differences, $\Delta I_0 = (I_{t=0} - (I_{aft} + I_{bef})/2)$. The intensity $I_{t=0}$, corresponding to the bulk solution [S] was determined by the extrapolation procedure. The intensity data used for ΔI in this table were the last (or first) points of a regular, monotonic sequence of decreasing intensities; shuttered segments for which one or both of I_{aft} or I_{bef} deviated from a regular sequence were discarded.

Table 18. Estimation of diffusion effects ^a

Segm't	ΔI_D , ^b counts	Δt , ^c s	I_0 , counts	$(I_s)_{ave}$, counts	$\Delta I_{0(s)}$, ^d counts	$I_{ave(s)}$, ^e counts	$\Delta I_{ave(s-1)}$, ^g counts	Δt_{s-1} , ^e s	$\Delta I_{adj(s)}$, ^h counts	$\Delta I_D/\Delta I_{adj(s-1)}$
4	1236	171	18,000	14,832	3168	13841	3119.00	-133.0	4010	0.308
4	1176	152	18,000	13,025	2975	13724	2547.00	-114.0	3396	0.346
2	454	300	11,600	9,321	1928	9824	1361.00	-150.0	2722	0.166
4	998	300	11,600	8,238	3362	8437	1396.00	-230.0	1820	0.548
2	544	300	11,400	9,964	1436	10273	1162.00	-180.0	1936	0.280
2	579	300	12,400	9,210	3190	9861	1879.00	-120.0	4697	0.123
4	611	300	12,400	7,974	4426	8406	1255.00	-120.0	3137	0.194
2	1532	300	12,000	10,235	1765	9804	1478.00	-120.0	3695	0.414
4	932	300	12,000	10,235	1865	10130	1743.00	-150.0	3486	0.2673
Summary: Averages of $\Delta I_D/\Delta I_{adj(s-1)}$: (a) segment 2, 0.25 ± 0.13; (b) segment 4, 0.33 ± 0.13; (c) all segments, 0.29 ± 0.13.										

^a Experiments with superimposed 405 and 532 nm laser irradiations in which the 405 nm laser was shuttered for 1-3min (Δt). Segments numbered as below. ^b ΔI_D = the increase in emission intensity between the end of a dual photolysis segment and the beginning of the next one (before and after shuttering the 405 nm laser); see below. ^c Δt = photolysis time in the segment considered; see below. ^d $\Delta I_{0(s)} = I_0 - (I_s)_{ave}$; $(I_s)_{ave}$ = average of the emission intensity between the end of a dual photolysis segment and the beginning of the next one. This assumes that the extent of diffusion is too small to dilute the bulk substrate concentration; thus, there is no statistically meaningful difference between the 2nd and 4th segments even though the net photolysis time is about twice as long for the latter. ^e For the linear part of the preceding segment. ^f Average of initial and final points of the linear part of the preceding segment. ^g Difference between the initial and final points of the linear part of the preceding segment. ^h $\Delta I_{ave(s-1)}$ adjusted for segment time differences = $\Delta I_{ave(s-1)} \times (\Delta t_s/\Delta t_{s-1})$.

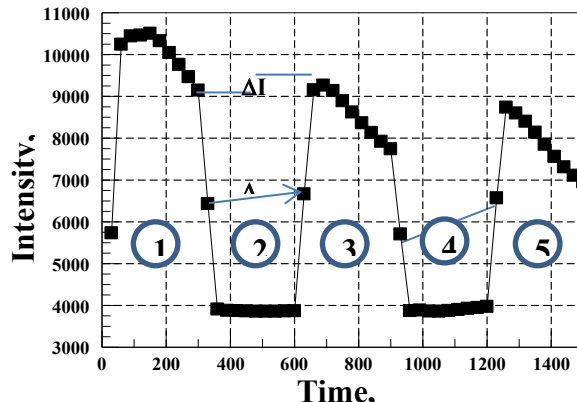


Figure 28. The parameters used in k_D calculations for the 3mm id cuvette. Segment numbers are circled. I_0 is selected as illustrated in this section 2.3 and/or by comparison to other experiments in the same series. The manual shutter opening (or closing) can complicate the initial intensity determination for a segment and when this happens, we used a short extrapolation as illustrated at the beginning of segment 3 (note that some photochemistry occurs during the opening and closing of the shutter).

2.3.16. An example of the effect of diffusion

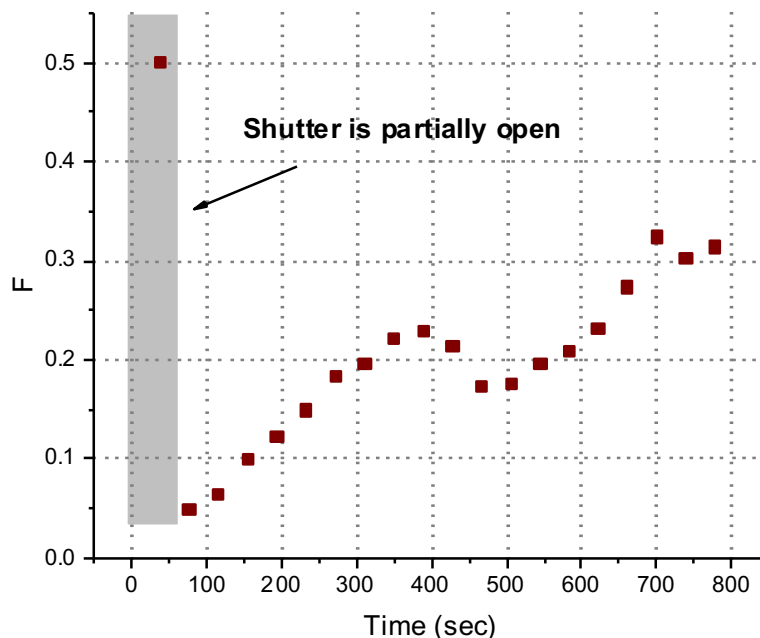


Figure 29. An example of the effect of vibration and diffusion on the observed emission intensities. The anomaly at 400 s was generated by tapping the photolysis cell. The gray rectangle indicates the time during which the shutter was being opened.

2.4. DISCUSSION AND CONCLUSION

This study has used the acid concentration dependent initial photodecomposition rate of the $[\text{Ru}(\text{bpy})_3]^{2+}$ $^3\text{MLCT}$ excited state with 405 nm irradiation to demonstrate that it is photoionized with high energy visible light and that the dominant photo-products are electron-containing, ion-pair precursors to the formation of free solvated electrons. Free energy considerations suggest that this should be the case and this work sets an upper limit of 3.06 eV for the photoionization energy of this complex. The net photoionization quantum yield is apparently of the order of 10% and much larger than previously suspected based on the spectroscopic detection of free electrons because the very rapid recombination reactions within the ion-pair species makes them very hard to detect. This kind of behavior is expected to be common for redox active substrates with long-lived, visible light absorbing excited states.

2.4.1. The $[\text{Ru}(\text{bpy})_3]^{2+}$ $^3\text{MLCT}$ excited state photoionization

The observation that products of the 405 nm irradiation of the $^3\text{MLCT}$ excited state oxidizes iodide to regenerate most of the photo-decomposed substrate complements the spectroscopic observations of the free solvated electrons generated by its higher energy, short pulse irradiations.⁴³⁻⁴⁵ That the predominant metal-containing photoproduct is $[\text{Ru}(\text{bpy})_3]^{3+}$ for all acid concentrations in the 0.001-4 M range while the photodecomposition yield increases in a somewhat complex way by more than 10-fold in this range indicates that: (a) H^+ scavenges more than one electron containing species; and (b) back electron recombination with $[\text{Ru}(\text{bpy})_3]^{3+}$ is very rapid for the species that are scavenged at the higher acid concentrations. Since the free solvated electron reacts with H^+

in water with a diffusion limited rate constant of $2.3 \times 10^{10} \text{ M}^{-1}\text{s}^{-1}$,⁴⁶ the scavengeable short lived species is most likely an ion pair, $[\text{Ru}(\text{bpy})_3]^{3+}$ and a solvated electron, trapped by their electrostatic attraction. The intermediacy of ion pairs has been well documented in the photoionization of the iodide ion.

2.4.2. Significance and implications of $[\text{H}^+]$ -dependent photoionization yields

The acid dependent electron scavenging for the $^3\text{MLCT}$ photoionization products is very similar in general form to that for the photoionization of I^- ,¹ as is shown in Figure 30. For this figure the initial rates from Table 8 have been converted to quantum yields relative to $\phi_{e^-} = 0.026$ for $[\text{H}^+] = 0.5 \text{ M}$, scaled to make the comparison to the I^- data easier and plotted vs. $-\log([\text{H}^+])$.¹

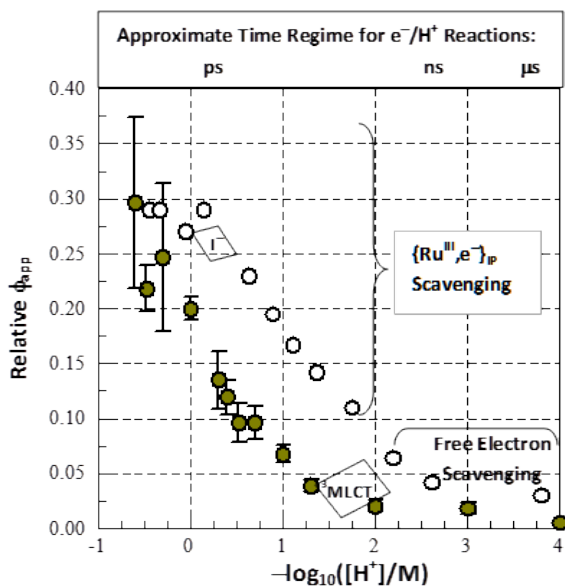
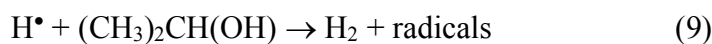
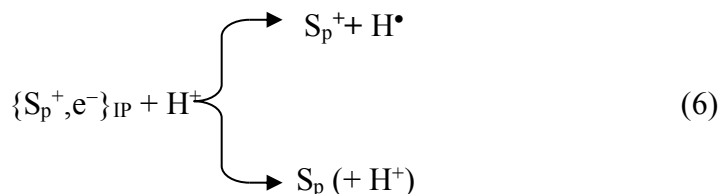
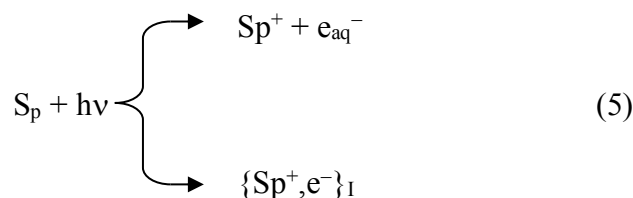
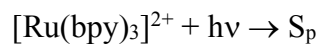


Figure 30. The initial rate of photodecomposition, R_{init} , replotted as function of $\log_{10}([\text{H}^+])$ for the photoionization of $[\text{Ru}(\text{bpy})_3]^{2+}$ $^3\text{MLCT}$ excited state (green circles) and estimated photoionization yields for the 254 nm irradiation of I^- (white circles). The photoionization yields for the $[\text{Ru}(\text{bpy})_3]^{2+}$ $^3\text{MLCT}$ excited state were relative to ϕ for $[\text{H}^+] = 0.5 \text{ M}$ in Table 11 and were calculated as $\phi_{\text{rel}} = 3.4 \times R_{\text{init}} \times (0.026/52)$; R_{init} data are from Table 7. The photoionization yields for I^- are from Figure 1 of ref. ¹.

The time regime for the e^-/H^+ reaction in aqueous solution is based on the rate constant, $= 2.3 \times 10^{10} \text{ M s}^{-1}$ and $\tau_{\text{react}} = 1/([H^+])^2$.

The basic chemical reactions involved in these systems can be represented simply as (with $S_p = {}^3\text{MLCT}$ or I^- ; and $S_p^+ = [\text{Ru}(\text{bpy})_3]^{3+}$ or I^\bullet),



The hydrogen ion/electron scavenging kinetics can be treated as a competition between the scavenging reaction, eqs 5 and/or 7, and the recombination reaction, eqs 6 and/or 8. This treatment is simplest for a single scavenging reaction, and for strongly acidic solutions the reactions in eqs 5 and 6 are dominant. For this condition the initial rate can be represented as eq 2 and $R_{\text{init}} \approx \phi_e G(\lambda) \{ [H^+] / (f_{R,h} + [H^+]) \}$. This equation represents the initial rate as the product of a factor, $\phi_e G(\lambda)$ that depends only on the properties of the substrate S and a factor, $[H^+] / (f_{R,h} + [H^+])$, that depends on the details of the scavenging

kinetics. The variable, $f_{R,h}$ is the ratio of the first order rate constant for the recombination reaction to the second order rate constant for the reaction of $\{S^+, e^-\}_{IP}$ with H^+ .

The different $[H^+]$ regimes for the scavenging of the photo-generation of electrons from $[Ru(bpy)_3]^{2+}$ and I^- illustrated in Figure 27 are a consequence of the large differences in values of $f_{R,h}$ in the kinetic factor. Since k_h should be nearly the same in both systems, this contrast arises from differences in the recombination rate constants with $k_R(^3MLCT) \sim 10 \times k_R(I^-)$. This is in accord with the expectation that $k_R(^3MLCT) > k_R(I^-)$ due to the larger number of acceptor electronic states and the cationic charge of $[Ru(bpy)_3]^{3+}$. The large number of electronic states with different energies is important in determining k_R since the electron transfer rate constant depends strongly on the driving force for the reaction, ΔG_{et} : $k_R = Z \times \exp(-\lambda_{reorg}[1 - (\Delta G_{et}/\lambda_{reorg})]^2)$; λ_{reorg} is the reorganizational energy associated with the electron transfer process.⁴⁷

The kinetic competition between the scavenging and recombination rate as obtained from the rate equations, gives a simple dependence of R_{init} on $[H^+]$ when there is a single radical pair species involved: $R_{init} \propto [H^+]/(f_{R,h} + [H^+])$; section 2.5. The fits of the data in Table 8 to this function gave $f_{R,h} \approx 0.7 \pm 0.2$. This resulted in $k_R \sim 0.7 \times 2.5 \times 10^{10} \text{ s}^{-1} = 180 \text{ ps}^{-1}$ in contrast to the value of $k_{h,e}$ resulted in $k_R \approx 0.02 \text{ ps}^{-1}$ for the bulk solution combination reaction. The recombination lifetime for the reaction of these species is much shorter than that of the solvated electrons reacting with this substrate (k_R is estimated to be greater than 150 ns for e_{aq}^- when $[Ru(bpy)_3]^{3+} < 10^{-4} \text{ M}$).^{2, 26} in section 2.5, the mechanistic arguments and the fitting in Figure 12 (dashed line) shows that there is only

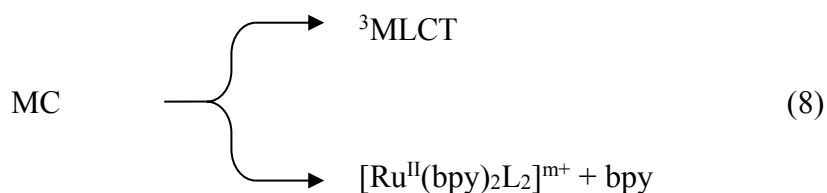
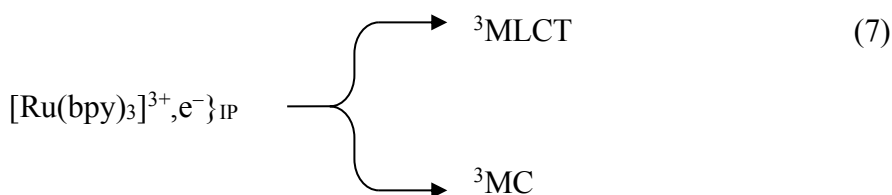
one $\{[\text{Ru}(\text{bpy})_3]^{3+} e^{-}\}_{\text{IP}}$ species for $[\text{H}^+] > 0.1 \text{ M}$ and this is not likely to be the case. Based on CTTS recombination to generate the iodide in fs time regime¹⁷ it is likely that the ionized species formed close to $[\text{Ru}(\text{bpy})_3]^{3+}$ complex recombined too efficiently (i.e., with $f_{\text{R,h}} \gg 4 \text{ M}$) to be detected by the chemical scavenging that we used. Thus, we interpret that the fitted parameter $f_{\text{R,h}}$ representing an average of the contributions of the many species scavenged under our conditions and that the species detected are limited by the rate of H^+ diffusion.

2.4.3. Photoionization yields and threshold energy. We have estimated the quantum yield of scavengeable photoelectrons to be in the range of 0.01-0.03 based on the model used for $[\text{H}^+] = 0.5 \text{ M}$ (TABLE 11), and we were not able to determine the maximum scavenging yield because the rate of H^+ diffusion and maximum feasible $[\text{H}^+]$ limit the lifetimes of scavengeable species to longer than 10 ps. The observations summarized in Table 19 suggest that the primary photoionization quantum yield is greater than 0.1. The yield inferred for free electrons from 405 nm irradiation is about 0.005, and smaller than Goetz's value of 0.02 for 355 nm irradiation which is consistent with $E_{\text{th}} \leq 3.06 \text{ eV}$.

An important implication of these considerations and Figures 9 and 35 is that the net photoionization yield is much greater than implied by the detection of free solvated electrons: the largest values found for R_{init} are about ten times larger than those attributed to e_{aq}^{-} scavenging and chemical scavenging is unlikely to detect all of the $\{[\text{Ru}(\text{bpy})_3]^{3+}, e^{-}\}_{\text{IP}}$ species.

2.4.4. Possible complications from the generation of photo-substitution products

Our 405 nm photodecomposition of $[\text{Ru}(\text{bpy})_3]^{2+}$ may have resulted in small percentages of photo-induced ligand substitution which is a well-known process for the ^3MC excited state of this complex.^{26, 48-60} The reaction of e_{aq}^- with $[\text{Ru}(\text{bpy})_3]^{3+}$ has been reported to result in the formation of $^3\text{MLCT}$ and ^3MC $[\text{Ru}(\text{bpy})_3]^{2+}$ excited states and substitution of a bpy ligand through such population of the ^3MC excited state (eqs 7 and 8) is expected when the generated ion pair recombines. However, the $[\text{Ru}(\text{bpy})_3]^{3+}$ was found to be the dominant ruthenium product and we were not able to identify any other photoproduct that formed by the 405 nm irradiation even at low acid concentrations. .



Our observations indicate the photolysis of $[\{(\text{bpy})_2\text{Ru}\}_2\text{dpp}]^{4+}$ did not result in the photoionization by either 405 or 532 nm irradiation. Since the ratio of the products of the substrate absorptivities and incident light intensities is close to the ratio of the photoproducts resulted from 532 and 405 nm irradiations, as result, the photoionization of this complex might result in ligand substitution.

2.4.5. Some other related considerations

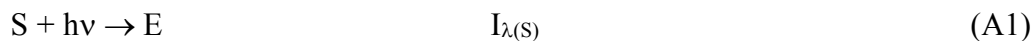
This study was initiated because the values estimated for E_{th} estimated for the $[\text{Ru}(\text{bpy})_3]^{2+}$ photoionization²⁸ was much larger than the values of ΔG_{th} . Lever and coworkers⁶¹⁻⁶² have discussed the relationships between electrochemical potentials and of charge transfer absorption spectra to the substrate's ionization and affinity energies. The energy requirements for the photoionization of chemical species is a matter of thermodynamics, and once the thermodynamic energy requirements are met the product yields depend on some system specific details such as the efficiencies of crossing from the potential energy (PE) surfaces of high energy excited states to the dissociative photoionization PE surface and/or the diffusive separation of products. However, the condensed phase photoionization process has been difficult to investigate because of the interactions of the electron with the solvent even for simple species like the iodide ion. The free energy parameters (electrode potentials) are available for a variety of redox active complexes and can be used to estimate of the photoionization threshold free energy, ΔG_{th} . E_{th} is more difficult to determine since the entropy contributions are often not available, but the entropy contributions seem to be relatively small in magnitude ($T\Delta S$ of a few hundred meV at 300 K).^{2, 63} Many divalent ruthenium complexes have comparable ΔG_{th} values to that of $[\text{Ru}(\text{bpy})_3]^{2+}$. Contrary to that, G_{th} tends to have smaller magnitude for ruthenium complexes with lower charges. In support of these points, the spectroscopic and electrochemical properties of $[\text{Ru}(\text{phen})_3]^{2+}$ are very similar to those of $[\text{Ru}(\text{bpy})_3]^{2+}$ and it shows a similar photoionization behavior but with 1/3 smaller values of $\phi G(\lambda)$ probably

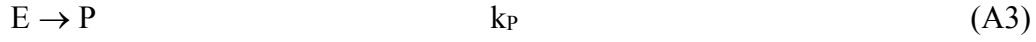
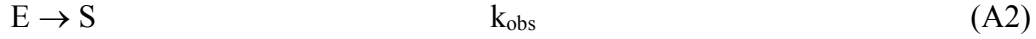
because of a smaller 405 nm excited state absorptivity and/or photoionization quantum yield.

2.5. Basic mechanistic treatment (treatment by J. F. Endicott): (2.5.1) ³MLCT thermal reactions and (B) photoionization

Since the incident 405 nm light intensity is constant throughout the experiment and since the concentrations of intermediates (and of products) are necessarily extremely small for the short irradiation times where R_{init} is determined, the photostationary state concentrations of these species are used to simplify the photolysis rate equations. For sufficiently small concentrations of a species X the absorbance of X $\ll 1$ and the intensity of radiation with a wavelength λ that it absorbs is $I_{\lambda(X)} \approx \epsilon_{X(\lambda)} d_{\text{pth}} [X] I_{\lambda}^{\circ} = \kappa_{\lambda(X)} [X]$; where $\epsilon_{X(\lambda)}$ = molar absorptivity of X at λ , d_{pth} = effective pathlength of the radiation through the photolysis cell, and I_{λ}° = intensity of the radiation incident on the cell. For brevity, S = Ru(II) substrate, E = ³MLCT and P = photo-reaction products. We assume that the quantum yield for forming the ³MLCT excited state by light absorption in the ground state is 1.0.⁶⁴ We have express the photolysis rates in terms of the fraction of substrate decomposed, F, where: $F = ([S]_{t=0} - [S]_t) / [S]_{t=0}$; $[S]_{t=0}$ = initial substrate concentration; t = irradiation time.

2.5.2. ³MLCT excited state reactions for generating a substitutional product: 1. The chemical equations representing the simplest mechanism for the formation of products directly from a ³MLCT thermal reaction are





2.5.3. The rate laws and photostationary states:

$$\frac{d[S]}{dt} = -\kappa_{\lambda(S)}[S] + k_{\text{obs}}[E] \quad \kappa_{\lambda(S)} \approx \epsilon_{X(\lambda)} d_{\text{pth}} I_{\lambda}^{\circ} \quad (\text{A4})$$

$$\frac{d[E]}{dt} = \kappa_{\lambda(S)}[S] - (k_{\text{obs}} + k_P)[E] \quad (\text{A5})$$

A very simple way to express the effect of diffusion on our observations is to represent it as a constant, k_D , multiplied by the difference between the substrate concentration in the bulk and photolysis regions. Then

$$\frac{d[P]}{dt} = k_P[E] - k_D[P] \quad (\text{A6})$$

If $k_{\text{obs}} \gg k_P$, then the photostationary state (ps) approximation is

$$\frac{d[E]}{dt} = \kappa_{\lambda(S)}[S] - (k_{\text{obs}} + k_P)[E] \approx 0 \quad (\text{A7})$$

$$[E]_{\text{ps}} \approx \frac{\kappa_{\lambda(S)}}{k_{\text{obs}} + k_P} [S] \quad (\text{A8})$$

$$\frac{d[P]}{dt} \approx k_P \frac{\kappa_{\lambda(S)}[S]}{k_{\text{obs}} + k_P} - k_D[P] \quad (\text{A9})$$

$$\frac{dF}{dt} \approx k_P \frac{\kappa_{\lambda(S)}(1-F)}{k_{\text{obs}} + k_P} - k_D F = k_P \frac{\kappa_{\lambda(S)}}{k_{\text{obs}} + k_P} - \left(k_D + \frac{k_P \kappa_{\lambda(S)}}{k_{\text{obs}} + k_P} \right) F \quad (\text{A10})$$

This is of the form, $\frac{d[F]}{dt} \approx A - BF$ with $A = \frac{\kappa_{\lambda(S)}}{k_{\text{obs}} + k_P} k_P$ and $B = (k_D + A)$. For $\lambda = 405$ nm in

the 3 mm cuvette, $\kappa_{405(S)} = \epsilon_{S(405)} d_{\text{pth}} I_{\lambda}^{\circ} = (7330)(0.3)(7.4 \times 10^{-2}) = 163 \text{ s}^{-1}$. The integral form

of eq A10 is $\left(\frac{\ln(A - BF)}{-B} = t\right)_0^\infty$. Since $F = 0$ for $t = 0$ and in the absence of diffusion ($k_D = 0$) F

= 1 at $t = \infty$

$$F = \frac{A}{B}(1 - e^{-Bt}) = F_\infty(1 - e^{-kt}) \quad (\text{A11})$$

Or, $F_\infty = A/B$, $k = B$.

2.5.4. The reduced initial rates. From eq A11, $R_{\text{init}} = A = F_\infty \times k$. Note that k is a pseudo-first order rate constant for the observed process (including diffusion, as in B below) for the observed process and $(A/B) \times B = R_{\text{init}}$ is the first order or pseudo-first order rate constant for the chemically important process (such as k_p in eq A3); for conciseness we have referred to R_{init} as the “initial rate”.

$$R_{\text{init}} \approx \frac{\kappa_{\lambda(S)}}{k_{\text{obs}} + k_p} k_p; \quad (\text{A12})$$

$$\text{Rearranging eq A12: } k_p \approx \frac{k_{\text{obs}}}{\kappa_{\lambda(S)} - R_{\text{init}}} R_{\text{init}}$$

$$\text{Thus, } F_\infty \approx \frac{k_p \frac{\kappa_{\lambda(S)}}{k_{\text{obs}} + k_p}}{k_D + \frac{k_p \kappa_{\lambda(S)}}{k_{\text{obs}} + k_p}} = \frac{k_p \kappa_{\lambda(S)}}{k_D (k_{\text{obs}} + k_p) + k_p \kappa_{\lambda(S)}} \quad (\text{A13})$$

$$\text{and, } k \approx k_D + \frac{k_p \kappa_{\lambda(S)}}{k_{\text{obs}} + k_p} = \frac{k_D (k_{\text{obs}} + k_p) + k_p \kappa_{\lambda(S)}}{k_{\text{obs}} + k_p} = k_D + R_{\text{init}} \quad (\text{A14})$$

From A14 and for $F \ll 1.0$ (as for the $[(\text{bpy})_2\text{Ru}\{2\text{dpp}\}]^{4+}$ photodecomposition) and for $k_{\text{obs}} \gg k_p$, $k_p \kappa_{\lambda(S)} \ll k_D (k_{\text{obs}} + k_p)$ and

$$F_\infty \approx \frac{k_p \kappa_{\lambda(S)}}{k_D k_{\text{obs}}} \quad (\text{A15})$$

For the other limit, $k_{\text{obs}} \ll k_p$,

$$F_{\infty} \approx \frac{\kappa_{\lambda(S)}}{k_D + \kappa_{\lambda(S)}} \sim 1 \quad (\text{A16})$$

2.5.5 Quantum yield. For $k_{\text{obs}} \gg k_p$ and $\kappa_{\lambda(S)} \gg R_{\text{init(d)}}$ in eq A12,

$$\phi_p = \frac{dP/dt}{d[\text{photons}]/dt} \approx \frac{k_p \left(\frac{\kappa_{\lambda(S)}}{k_{\text{obs}} + k_p} [S] \right)}{\kappa_{\lambda(S)} [S]} \approx \frac{R_{\text{init}}}{\kappa_{\lambda(S)}} \quad (\text{A17})$$

2.6. Acid dependent, two photon photoionization and the photoionization quantum yield expressed in terms of experimental rate parameters.

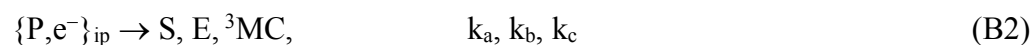
2.6.1. Some general considerations and simplifying assumptions:

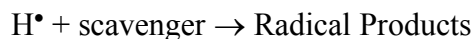
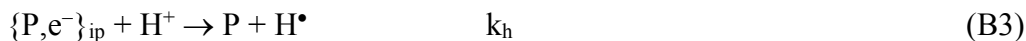
We consider only the acid dependent processes leading to products. Since the total ruthenium species ($S + P + \dots$; P = the electron product species) is orders of magnitude smaller than $[H^+]$ in strongly acidic solutions ($[H^+] \geq 0.01$ M), the diffusion limited e^-/P and e^-/S reactions of the “free” solvated electron would not be competitive with the e^-/H^+ reaction. The increases of R_{obs} with increasing acid for $[H^+] > 0.01$ M, where the predominant Ru-containing photoproduct species can be reduced by I^- results in the recovery of most of the photo-bleached $[Ru(\text{bpy})_3]^{2+}$ absorbance leads us to postulate that the proton-dependent photodecomposition of $[Ru(\text{bpy})_3]^{2+}$ in highly acidic solutions predominately results from some proton scavenging of $\{P.e^-\}_{IP}$ species, similar to related observations for I^- .^{1, 28} For this limit, the excited state photolysis products that contribute to the initial rate can be formulated as an associated pair of product species (or as an “ion pair”).

In principle the H^+ scavenging of the $\{P, e^-\}_{IP}$ species could involve either the direct scavenging of the ion pair (as appears to be the case for the $\{I^\bullet, e^-\}_{IP}$ ion pair)¹⁷ and/or scavenging of the electrons that escape from it (eqs B3 and B4). Our experiments do not distinguish between these or other details of ion pair behavior and we develop only the general aspects of the competition kinetics. Similarly, the treatment below assumes that the 2-propanol scavenging for the free aqueous proton is complete, that the radicals produced do not complicate the rate of photodecomposition of the substrate and we ignore any very fast reaction of H-atoms which are produced adjacent to the oxidized substrate and react by electron transfer to regenerate the substrate (which will be convoluted into a simple rate parameter, k_R). We consider a simple scavenging limit in which the only process that competes with the H^+ /electron scavenging results is the regeneration of the substrate either directly or by means of a series of chemical steps.

The mechanistic algebra applicable to the proton scavenging of the free solvated electron, at least for simple mechanisms, is summarized below.

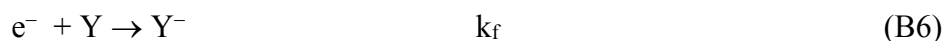
2.6.2. Basic reactions ($S = [Ru(bpy)_3]^{2+}$; $E = {}^3MLCT$; $P = [Ru(bpy)_3]^{3+}$) and kinetic parameters; for the proton induced photodecompositions of $[Ru(bpy)_3]^{2+}$ observed at high acid concentrations ($[H^+] > 0.1$ M):





Where k_a , k_b , and k_c are the rate constants for electron/Ru(III) recombination reactions that regenerate the substrate and different excited states (E and 3MC) and Y^{-} is some reduced species such as $[Ru(bpy)_3]^{+}$ or O_2^{-} . For simplicity we consider only one $\{P, e^{-}\}_{ip}$ species, but one expects several, probably not easily distinguished electron / $[Ru(bpy)_3]^{3+}$ “ion pair” species, each with a different recombination rate constant(s). Reactions B4-B5 are not considered further here.

Slower back reactions of the type B6 and B7 where Y is some species, such as S, propyl radicals, etc., can in principle complicate the long term kinetic details. Since we deal with the initial rate behavior, such reactions will not be considered here.



2.6.3. Rate equations. Our observations in strongly acidic solution correspond to the limit in which the contributions of reaction B5 are much smaller than those of B3 and we will only treat this limit. The rate equations for electron scavenging of the intermediate, $\{P, e^{-}\}_{ip} = U$, ($k_R = k_a + k_b + k_c + k_s$) are

$$\frac{d[S]}{dt} = -\kappa_{\lambda(S)}[S] + k_{obsd}[E] + k_a[U] \quad (B8)$$

$$\frac{d[E]}{dt} = \kappa_{\lambda(S)}[S] - k_{\text{obsd}}[E] - (k_b + k_c)[U] \quad (\text{B9})$$

$$\frac{d[U]}{dt} = \phi_U \kappa_{\lambda(E)}[E] - k_R[U] - k_h[H^+][U] \quad (\text{B10})$$

These reactions are a very simple expression of the photoionization behavior of this system. It has been reported that the free solvated electron/ $[\text{Ru}(\text{bpy})_3]^{3+}$ favors the regeneration of MLCT and MC excited states over $[\text{Ru}(\text{bpy})_3]^{2+}$ in its ground state²⁵⁻²⁶ and this possibility has been included in eqs B1, B9 and B10, with the assumption that the MC excited state populations mostly relax to the ³MLCT excited state.^{26, 65} Neglecting eqs B4 and B5,

$$\frac{d[P]}{dt} \approx k_h[H^+][U] - k_D(P) \quad (\text{B11})$$

Since $[S] \gg [E] \gg [U]$, we use the photostationary states (ps) in $[E]$ (eq A8) and $[U]$:

$$[E]_{\text{ps}} \approx \frac{\kappa_{\lambda(S)}[S]}{k_{\text{obsd}}} \quad (\text{A8})$$

$$\frac{d[U]_{\text{ps}}}{dt} = \phi_U \kappa_{\lambda(E)}[E]_{\text{ps}} - k_R[U]_{\text{ps}} - k_h[H^+][U]_{\text{ps}} \approx 0 \quad (\text{B12})$$

Equation B12 can be combined with eq A8 to obtain,

$$[U]_{\text{ps}} \approx \frac{\phi_U \kappa_{\lambda(E)}[E]_{\text{ps}}}{k_R + k_h[H^+]} \approx \frac{\phi_U \kappa_{\lambda(S)} \kappa_{\lambda(E)}[S]}{k_{\text{obsd}} \{k_R + k_h[H^+]\}} \quad (\text{B13})$$

Therefore, combining eqs B11 and B13,

$$\frac{d[P]}{dt} \approx k_h[H^+] \frac{\phi_U \kappa_{\lambda(S)} \kappa_{\lambda(E)}[S]}{\{k_R + k_h[H^+]\} k_{\text{obsd}}} - k_D(P) \quad (\text{B14})$$

Setting $F = [P]/[S]_{t=0}$ and $[S] = (1 - F)[S]_{t=0}$, eq B14 leads to

$$\frac{d[F]}{dt} \approx k_h [H^+] \frac{\phi_U \kappa_{\lambda(E)}}{k_R + k_h [H^+]} \frac{\kappa_{\lambda(S)} (1-F)}{k_{obsd}} - k_D F \quad (B15)$$

Rearranging eq B15,

$$\frac{d[F]}{dt} \approx \frac{\kappa_{\lambda(S)} \phi_U \kappa_{\lambda(E)} k_h [H^+]}{k_{obsd} (k_R + k_h [H^+])} - \left(k_D + \frac{\kappa_{\lambda(S)} \phi_U \kappa_{\lambda(E)} k_h [H^+]}{k_{obsd} (k_R + k_h [H^+])} \right) F \quad (B16)$$

Setting $G(\lambda) = \frac{\kappa_{\lambda(S)} \kappa_{\lambda(E)}}{k_{obsd}}$, which is a constant for each experiment, the reduced rate of

product formation is expressed as,

$$\frac{d[F]}{dt} \approx \phi_U G(\lambda) \frac{k_h [H^+]}{(k_R + k_h [H^+])} - \left(k_D + \phi_U G(\lambda) \frac{k_h [H^+]}{(k_R + k_h [H^+])} \right) F \quad (B17)$$

It is convenient to further simplify eq B17 by setting $k_R/k_h = f_{R,h}$,

$$\frac{d[F]}{dt} \approx \phi_U G(\lambda) \frac{[H^+]}{(f_{R,h} + [H^+])} - \left(k_D + \phi_U G(\lambda) \frac{[H^+]}{(f_{R,h} + [H^+])} \right) F \quad (B18)$$

This is in the same algebraic form as eqs A10 and A11 and leads to

$$\text{where } F_\infty \approx \frac{\phi_U G(\lambda) \frac{[H^+]}{(f_{R,h} + [H^+])}}{k_D + \phi_U G(\lambda) \frac{[H^+]}{(f_{R,h} + [H^+])}}, \quad k \approx k_D + \phi_U G(\lambda) \frac{[H^+]}{(f_{R,h} + [H^+])} \quad (B19)$$

In order to exhibit an acid independent plateau $[H^+]_{F(\infty)} > f_{R,h}$ and

$$F_\infty \approx \frac{\phi_U G(\lambda)}{k_D + \phi_U G(\lambda)} \quad (B20)$$

Note that eq B20 corresponds to the limit for relatively high acid concentrations where $k_h[H^+] > k_R$, and it is applicable in the region where $[H^+]$ variations do not result in significant variations in R_{init} . More generally,

$$R_{init} = A \approx \phi_U G(\lambda) \frac{[k_h H^+]}{(k_R + k_h [H^+])} = \phi_U G(\lambda) \frac{[H^+]}{(f_{R,h} + [H^+])}$$

(B21)

and

$$F_\infty \approx \frac{R_{init}}{k_D + R_{init}}$$

2.6.4. Quantum yields. The representation of the quantum yield in terms of measurable quantities for the photoionization processes discussed here is not simple. The absorption of photons whose energies exceed E_{th} will generate electrons distributed in solvent regions of the substrate's solvation sphere of the substrate and the bulk solvent. By analogy with the photoionization of I^- ,³¹ those electrons that are generated in the solvent immediately adjacent to the oxidized substrate (in a CTTS "state") are expected to recombine in the fs time regime and would not be detectable with a diffusion limited chemical scavenger. In contrast, ns lifetimes are expected for free solvated electrons in bulk solution² and these species are readily scavengeable with moderately dilute acids.^{1, 33} Clearly there is a wide range of oxidized substrate/photo-generated electron species with a correspondingly wide range of recombination lifetimes so the definition of the quantum yield for these species generally depends on the experimental approach used for their determination. These considerations indicate that the parameters in eq B21 are averages over a range of e^- species

scavenged. With these points in mind, the photoionization quantum yield based on H^+/e^-

scavenging with $G(\lambda) = \frac{\kappa_{\lambda(S)}\kappa_{\lambda(E)}}{k_{\text{obsd}}}$ and $[H^+] > 0.1 \text{ M}$ is,

$$\phi_{U(h)} = \frac{(f_{R,h} + [H^+]) R_{\text{init}}}{[H^+] G(\lambda)} \quad (\text{B22})$$

2.7. Conclusions

Our 405 nm irradiations resulted in moderate photoionization of $^3\text{MLCT}$ excited state of $[\text{Ru}(\text{bpy})_3]^{2+}$ at ambient condition in aqueous solution. In addition, the initial rate, R_{init} , of the photodecomposition increases as the acid concentration increases and our $[H^+]$ scavenger may intercept the electrons at an early stage of its evolution where it is still associated with $[\text{Ru}(\text{bpy})_3]^{3+}$. In addition, the calculated initial rate of the photodecomposition was almost doubled when the superimposed of 405 and 532 nm laser beams were used.

The photoionization quantum yield of $[\text{Ru}(\text{bpy})_3]^{2+}$ is much larger and its threshold energy corresponds to much longer wavelengths than it was previously believed. Similar low energy photoionization threshold energies are predicted for the $^3\text{MLCT}$ excited states of many $(\text{Ru}^{\text{II}}\text{-bpy})^{2+}$ chromophores since many divalent ruthenium complexes have values of ΔG_{th} comparable to that of $[\text{Ru}(\text{bpy})_3]^{2+}$.

CHAPTER 3. STUDIES OF THE PHYSICAL AND CHEMICAL EXCITED STATE PROPERTIES OF RUTHENIUM (II) COMPLEXES CONTAINING AROMATIC LIGANDS

[Collaborative project with Jeremy Kodanko's lab]

3.1. INTRODUCTION

Ruthenium(II) complexes with aromatic ligands (Ar) that have long-lived $^3\text{MLCT}$ excited states have been very important as photosensitizers; for example, these complexes often have been utilized in dye-sensitized solar cells^{13, 66} and photodynamic therapy.^{67,68,69,70} To efficiently promote electron transfer from or to the sensitizer's excited state, other competing decay pathways must be minimized. These competing decay pathways determine the lifetimes of the complexes and this issue has been extensively studied and reported in the literature.¹⁻¹⁵ Despite the large number of previous reports the choices of ligands that give rise to the desired excited state properties are most often based on extrapolations from the well characterized ground state species using idealized, often one electron models, and various empirical and/or trial and error approaches. Such approaches are not efficient, and they are often misleading. The problems arise in part because this class of transition metal complexes typically contain a few dozen electronic excited states with different molecular orbital distributions of electrons within a relatively narrow energy range. The actual electronic configurations of these excited states often has to be described in terms of mixtures of the extrapolated, idealized configurations. This mixing results in excited states with a corresponding mixture of the idealized chemical and physical properties that might be expected based on experience with electronic ground states. However, the excited state electronic configurations can be unique with few or no

ground state precedents so that properties extrapolated from those of ground states can be unreliable. The preferred approach is to model the excited state electronic configurations using a high level density functional theory calculation and to correlate the observed excited state properties with this model. While the transition metal electronic excited states are short lived species, usually with sub-millisecond lifetimes even at low temperatures, and therefore not easily characterized using conventional ground state-based methods, the characterization of these excited states can be approached in a systematic way by using a combination of emission spectroscopy and density functional theory modeling.

Many of the most investigated potential sensitizers involve a Ru^{II} center and at least one aromatic acceptor ligand and have a low energy electronic excited state which is most simply described as having an electronic configuration in which an electron has been promoted from the highest energy filled molecular orbital (HOMO), a mostly non-bonding Ru^{II} centered “dπ” orbital to the lowest energy unoccupied aromatic ligand orbital (LUMO). This simple, idealized electronic configuration is referred to as a metal-to-ligand charge transfer excited state (MLCT). The chemical and physical properties of the lowest energy MLCT excited states are generally discussed in terms of this idealized model, sometimes with small perturbation theory-based corrections to it. In most cases the triplet (³MLCT) excited states emit in the visible or near infrared spectral region, and their emission bands often have resolved vibronic sidebands.⁷¹⁻⁷⁸ The relative intensities of these vibronic sidebands are correlated with excited state molecular distortions with the most intense vibronic sidebands corresponding the most distorted bond lengths or bond angles in the excited state; thus, the vibronic sidebands of an emission spectrum contain

information about the molecular structure of the emitting excited state and the excited state distortions are related to the molecular moieties which differ in excited state and ground state electron density. The distribution of excited state electron density and the associated bond distortions can be modeled using DFT approaches^{58, 79-82} and this can be compared to the structural implications of the vibronic sidebands of the emission spectrum. So far this approach has only been used on a number of complexes with relatively simple aromatic ligands.^{58, 79-82} Complexes with relatively long excited state lifetimes have been of some interest as potential sensitizers in some applications, but the strategies for their synthesis have relied mostly on extrapolations of experience with ground state systems and there has been very little systematic study of the ligand properties that might give rise to such behavior. There have been suggestions that ligands with extensively delocalized electron density in their LUMOs might result in increased ³MLCT excited state lifetimes and we have undertaken the study of the excited state properties of some Ru^{II} complexes with quinoline-based ligands in order to find out how such excited state electronic delocalization affects the physical properties of Ru-quinoline ³MLCT excited states.^{58, 79-85}

Most Ru-Ar complexes with a wide variety of ancillary and acceptor ligands can be easily synthesized. Previous work from this laboratory, partly in collaboration with Professor Y. J. Chen's lab, has involved systematic emission spectroscopic studies and DFT modeling of Ru-bpy and Ru-MDA chromophores (MDA = monodentate aromatic ligand such as pyridine, phenylpyridine, pyrazine, etc.).^{38, 58, 79-84} The Ru-bpy and Ru-MDA chromophores have distinctly different 77 K emission characteristics which can be attributed to differences in their ³MLCT excited state mixing with other excited states:

(a) The vibronic sidebands of the Ru-bpy chromophores increase in relative intensity with increasing $^3\text{MLCT}$ excited state energy. This feature correlates with increased $(^3\text{MLCT})_{\text{ideal}}/\pi\pi^*$ configurational mixing in the triplet manifold.^{79, 84, 86} The radiative rate constants, k_{RAD} , for these chromophores are also energy dependent and in the range of $(0.5-8)\times 10^4, \text{ s}^{-1}$.

(b) The vibronic sidebands of the Ru-MDA chromophores have not been resolved at 77 K and $k_{\text{RAD}} \approx (3\pm 2)\times 10^3 \text{ s}^{-1}$ is nearly energy independent in the range examined. The 77 K emission lifetimes for this class of chromophores are slightly longer than those of the Ru-bpy chromophores at the same energy.

3.2. EXPERIMENTAL SECTION

3.2.1. Compounds prepared for the study of the chemical and physical properties of $^3\text{MLCT}$ excited states of ruthenium quinoline complexes

Potassium phthalimide, 1-(chloromethyl)isoquinoline, and hydrazine monohydrate, were purchased from Oakwood Chemical (West Columbia, South Carolina, SC) and used without further purification. Ethyl acetate and hexane ($\geq 99\%$) were purchased from Fisher Scientific (Pittsburgh, Pennsylvania, PA) for spectroscopic experiments. The [1 or 3-Ru(iso-TQA)(X)₂] complexes were provided by Professor Jeremy Kodanko's research group; tris (isoquinolin-1-ylmethyl) amine (TQA) was synthesized as described elsewhere⁸⁷ and [1-Ru(TQA)(CN)₂] was synthesized using a literature procedure.⁸⁸ Chloropentaamineruthenium(III) chloride 98% was obtained from Strem. The isoquinoline ligand was obtained from Oakwood Chemical. The [Ru(NH₃)₅-isoquinoline]

complex was synthesized using literature procedures.⁸⁹ $[(Ru(bpy)_2)_2(2, 3-dpp)](PF_6)_4$ was synthesized as reported previously.³⁶

Syntheses of these compounds were done under a flow of argon gas using a Schlenk line in the dark. Vapor diffusion and recrystallizations of these complexes were the main purification techniques. Column chromatography (Al_2O_3) techniques were also used.

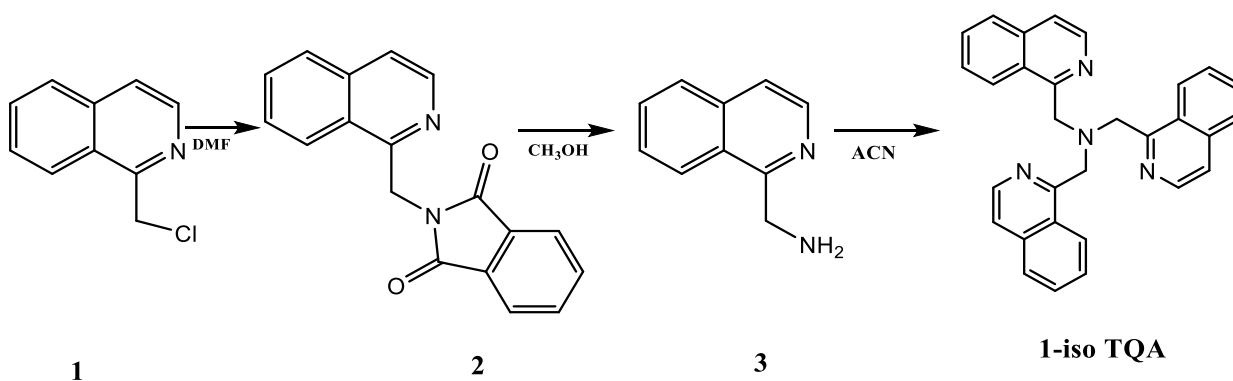


Figure 31. Synthesis of 1-iso TQA

Synthesis of N-(1-isoquinolylmethyl) phthalimide (2)⁸⁷

To the DMF solution (11 mL) of 1- (265 mg, 1.49 mmol) potassium phthalimide (278 mg, 1.50 mmol) was added and stirred overnight at room temperature. After the addition of chloroform, the organic layer was washed with water and 10% NaOH. The organic layer was dried, evaporated, and washed with hot ethanol to give 2 as white powder. Yield: 303 mg (1.05 mmol, 70%). ¹H NMR (CDCl₃): δ (d, J=5.7Hz,1H),8.21(d,J=7.8Hz, 1H), 7.90–7.93 (m, 2H), 7.83 (d, J = 8.4 Hz, 1H), 7.65–7.76 (m, 4H), 7.52 (d, J = 5.7 Hz, 1H), 5.54 (s, 2H). ¹³C NMR (CDCl₃): δ 168.5, 153.0, 141.9, 136.1, 133.9, 132.5, 130.1, 127.5, 125.9, 123.7, 123.5, 120.3, 40.7.

Synthesis of 1-Aminomethylisoquinoline (3)⁸⁷

To the methanol solution (11 mL) of N-(1-isoquinolylmethyl) phthalimide (2) (132 mg, 0.46 mmol) hydrazine monohydrate (0.38 mL, 7.8 mmol) was added and refluxed for 1.5 h. After the addition of water, the insoluble materials were filtered off. The filtrate was acidified with hydrochloric acid and filtered. The filtrate was neutralized with aqueous NaOH and extracted with ethyl acetate. The organic layer was dried and evaporated to give **3** as yellow oil. Yield: 6 mg (0.29 mmol, 63%). ¹HNMR(CDCl₃): δ 8.45 (d, J=5.4 Hz, 1H), 8.08 (d, J=8.1 Hz, 1H), 7.81 (d, J = 7.8 Hz, 1H), 7.50–7.70 (m, 3H), 4.49 (s, 2H). ¹³C NMR (CDCl₃): δ 159.9, 141.2, 135.7, 129.7, 127.1, 127.0, 125.7, 123.8, 119.6, 44.6.

Synthesis of Tris(1-isoquinolylmethyl)amine (1-isoTQA)⁸⁷

To the acetonitrile solution (90 mL) of 1-chloromethylisoquinoline (1) (501 mg, 2.82 mmol) and 1-aminomethylisoquinoline (3) (223 mg, 1.41 mmol) potassium carbonate was added (1.05 g, 7.60 mmol) and stirred for 4 days under reflux. After removal of the solvent, the residue was extracted with a chloroform/water mixture. The organic layer was dried, evaporated, and washed with acetonitrile to give 1-iso-TQA as white powder. Yield: 70 mg (0.39 mmol, 27%). ¹HNMR(CDCl₃): δ 8.49 (d, J=5.7 Hz, 3H), 7.75 (d, J=8.4 Hz, 3H), 7.58 (d, J = 6.0 Hz, 3H), 7.47 (dd, J = 6.9, 8.1 Hz, 3H), 6.98 (d, J = 8.7 Hz, 3H), 6.58 (dd, J = 6.9, 8.4 Hz, 3H), 4.35 (s, 6H). ¹³C NMR (CDCl₃): δ 158.0, 141.4, 136.0, 129.5, 127.3, 126.5, 125.9, 120.6, 60.0.

Synthesis of [Ru (tris(isoquinolin-1-ylmethyl)amine)(NC)₂]²⁺⁸⁸

TQA (47.2 mg, 0.11 mmol), which was prepared by a known procedure⁸⁷ was dissolved in 10 mL of dry MeOH under inert atmosphere in a pressure flask. To this Ru(DMSO)₄Cl₂ (52.0 mg, 0.11 mmol) was added and the solution was purged with Argon for 10 min at room temperature. The reaction mixture was refluxed for 5 h. The reaction mixture changed in color from pale yellow to dark red. The dark red reaction mixture was cooled to room temperature and concentrated under reduced pressure. To the flask NaCN (53.9 mg, 1.1 mmol) and 1:1 mixture of EtOH: H₂O (10 mL) were added and the mixture was refluxed for 16 h under inert atmosphere. Ice cold water (20 mL) was then added to the reaction mixture which resulted in the formation of dark red precipitate which was filtered, washed with ice cold water (300 mL), stirred with Et₂O, filtered and dried under reduced pressure to give the title complex as a dark red solid (39 mg, 61%): mp = 194 °C (decomp); ¹H NMR (400MHz (CD₃)₂SO) δ 9.64 (d, 1H, *J* = 6.0 Hz), 8.66 (d, 2H, *J* = 6.4 Hz), 8.14-8.16 (m, 2H), 7.90-7.82 (m, 3Hz), 7.77-7.70 (m, 6H), 7.65-7.62 (m, 3H), 7.51 (t, 1H, *J* = 8.0 Hz), 5.94 (d, 2H, *J* = 15.6 Hz), 5.54-5.49 (m, 4H); IR (KBr) ν_{max} (cm⁻¹) 3852, 3744, 3726, 3673, 3528, 3432, 3252, 2994, 2947, 2891, 2063, 2043, 1693, 1650, 1594, 1553, 1503, 1453, 1394, 1376, 1317, 1294, 1262, 1236, 1198, 1145, 1099, 955, 827, 748, 679, 668, 660; UV-vis λ_{max} = 470 nm (ε = 9600 M⁻¹cm⁻¹); LR-ESMS Calcd for C₃₂H₂₅N₆O₃Ru *m/z* = 595, Found 595; Anal. Calcd for C₃₄H₃₁N₁₂ORu: (2·0.5 H₂O·0.5 Et₂O) C, 63.74; H, 4.88; N, 13.12. Found: C, 63.49; H, 4.54; N, 13.29.

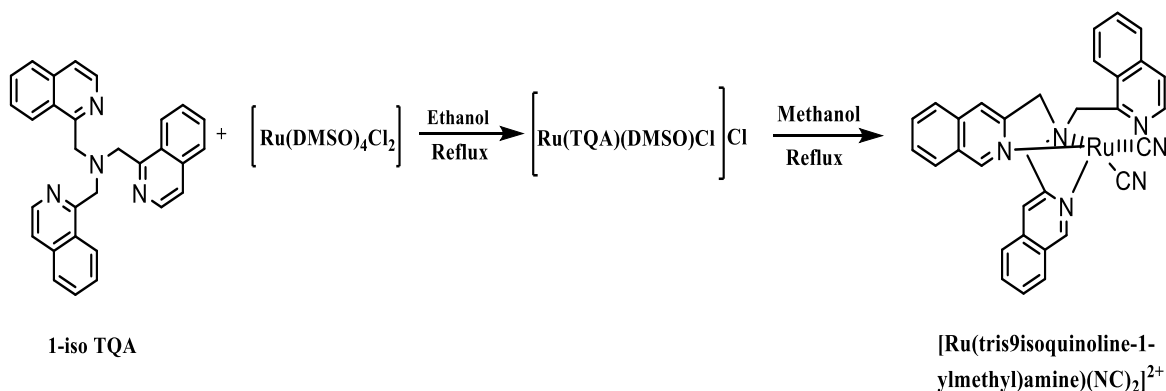


Figure 32. Synthesis of [Ru (TQA)(CN)₂]

Synthesis of [dicyano-bis-2(2,2'-bipyridine) ruthenium (II)dihydrate [Ru(CN)₂(bpy)₂.2H₂O

The complex Ru(bpy)₂Cl₂.2H₂O (0.320 g) in methanol (10 mL) and water (10mL) was heated under reflux with sodium cyanide (2g). The purple solution turned orange and after 1 h was filtered and methanol evaporated using rotary evaporator. The orange solid was washed with cold water and diethyl ether, respectively and then dried in vacuum overnight to realize a pure orange compound suitable for analysis. Yield: 0.300g. ¹H NMR (400MHz, methanol-d₄): δ 9.64,8.51, 8.45, 8.07, 7.91, 7.65, 7.59, 7.28. ¹H NMR (400MHz, methanol-d₄): δ 158.6, 157.1, 156.3, 155.1, 148.9, 137.1, 136.2, 126.5, 126.2, 123.3, 122.8. CV in butyronitrile. E_{1/2} mV (ΔE_p, mV): +841(54), 1573(50). Ferrocene/ferrocenium {+464 mV (60 mV)}. Absorption in ethanol/methanol (1:1 v/v): MLCT absorption at 462 nm (21645 cm⁻¹).

Synthesis of 2-(chloromethyl)nicotinonitrile⁹⁰. To 2-methylnicotinonitrile (2.0 g, 16.9 mmol) in chloroform (30 mL) at reflux was added trichloroisocyanuric acid (1.57 g, 6.75 mmol) and the mixture was heated at reflux overnight. After cooling, the mixture was filtered, and the filtrate was diluted with dichloromethane, washed with sodium hydroxide

solution and then brine, dried (MgSO_4), and evaporated to give 1.5 g of pure product which by NMR contained ~19% starting material and 7% dichlorinated product: ^1H NMR (360 MHz, CDCl_3) δ 4.85 (2H, s), 7.43 (1H, dd, J) 7.9 and 4.9 Hz), 8.02 (1H, dd, J) 7.9 and 1.7 Hz), 8.81 (1H, dd, J) 4.9 and 1.7 Hz).

Synthesis of $[\text{Ru}(\text{NH}_3)_5(\text{iso-quinoline})](\text{PF}_6)_2$ ⁸⁹

A 0.2-g sample of the $[\text{Ru}^{\text{III}}(\text{NH}_3)_5\text{Cl}]\text{Cl}_2$ starting material in 5 mL of H_2O was reduced by 1 g zinc amalgam in the dark with argon-bubbling agitation for 30 min and then transferred to an argon-degassed solution of 1.2 eq of the ligand, (iso-quinoline, L), in 10 mL of water. After 2 h, filter the mixture and the crude $[\text{Ru}^{\text{II}}(\text{NH}_3)_5(\text{L})](\text{PF}_6)_2$ product was precipitated by adding 5 mL of a saturated solution of $(\text{NH}_4)\text{PF}_6$ in water to the filtrate. Yields were typically 60-70%. This material was purified in the following manner: The crude product was dissolved in a minimum volume (ca. 1 mL) of either Spectro quality or reagent grade acetone and cooled to 0°C in the freezer. On top of this was then carefully layered 2-3 mL of anhydrous ether, or until turbidity just started to occur in the upper part of the acetone layer. The resulting double-layered system was allowed to stand quietly and mix by diffusion in the ice bath for at least 12 h, at which point more ether was added if no solid had precipitated. For optimum purity, a recovery of no more than 40-50% was attempted. A second crop of reasonable quality could be obtained by repeating this procedure on the mother liquor after the first crop of dark, semicrystalline material had been collected. ^1H NMR (360 MHz, CDCl_3) δ 2.1 (s, 2H), δ 2.8 (d, 2H), δ 3.3 (s, 1H), δ 7.8 (m, 3H), δ 8.0 (m, 2H), δ 8.6 (s, 1H), δ 9.6 (s, 1H).

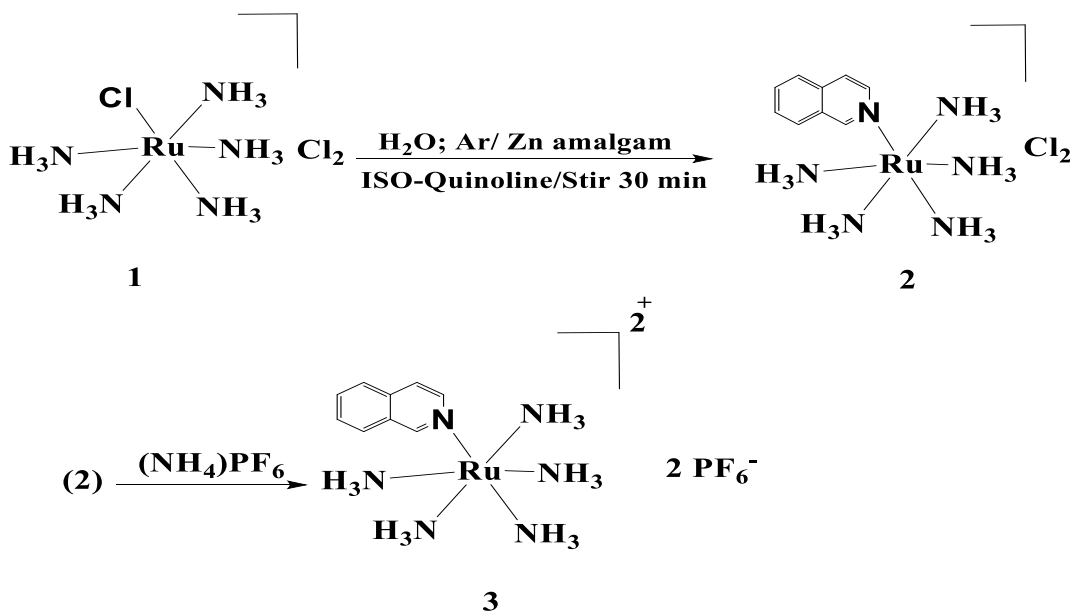


Figure 33. Synthesis of $[\text{Ru}(\text{NH}_3)_5(\text{Iso-Quinoline})]^{2+}$

3.2.2 Light sources for the study of the chemical and physical properties of $^3\text{MLCT}$ of ruthenium quinoline complexes

In these experiments we used the same light sources, except for the QTH lamp, that are described in Chapter II in addition to a 470 nm diode laser, which has a power nominally ≥ 10 mW (Changchun New Industries Optoelectronics Tech.Co., Ltd).

3.2.3. Instrumental system used for 77 K Emission spectroscopy set up for ruthenium quinoline complexes

The techniques used for emission spectroscopy have been described in Chapter II. The major modification for low temperature emission is that the sample in a 2 mm id cylindrical fluorescence cell was immersed in liquid nitrogen contained in a Dewar flask as shown in Figure 34.

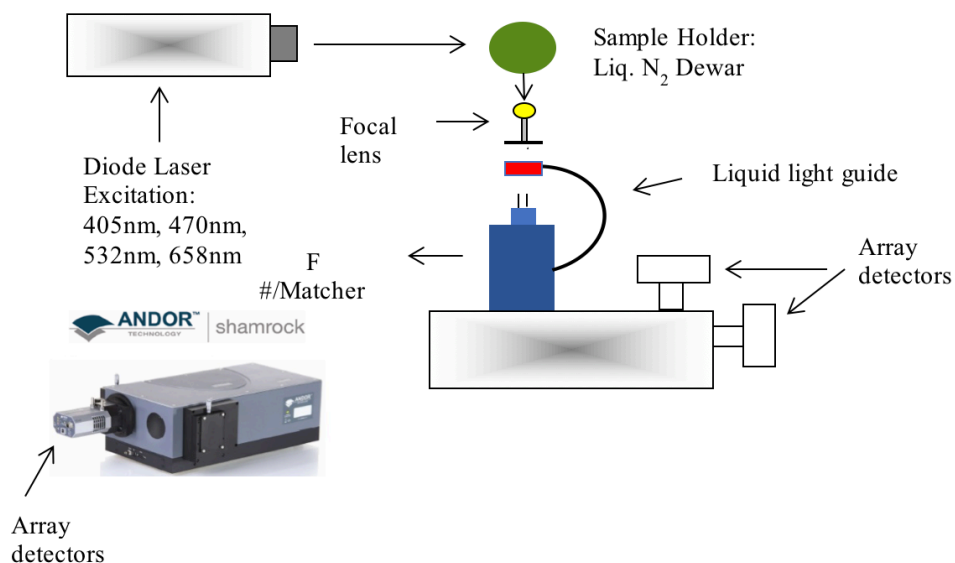


Figure 34: Ambient and 77K emission spectroscopy setup

3.2.4. Instrumental system used for low temperature absorption spectroscopy of Ru-quinoline chromophores

In order to determine quantum yields at low temperatures it is necessary to know the substrate's absorptivity at low temperatures. The absorption spectra of transition metal complexes are temperature dependent largely due to the temperature dependence of component bandwidths. The determinations of absorptivity are most readily determined in a cuvette, but rapid cooling of a cuvette, as happens when it is immersed in liquid nitrogen in a Dewar flask, causes the cuvette to break. However, it is possible to achieve reasonably low temperatures (87-90 K) for samples in a cuvette by slow cooling in a cryostat. The spectra of both ambient and low temperature absorptions were obtained using NSG Precision Cells, Inc. cryogenic square 1 cm quartz cuvettes with an ANDOR Shamrock

500 spectrometer in an Oxford Instruments OptistatCF Static Exchange Gas Continuous Flow Cryostat. Both detector and the liquid light guide and the Newton array detector contributed to a shortest wavelength spectral detection limit of $\lambda_{\text{obsd}} \geq 350$ nm.

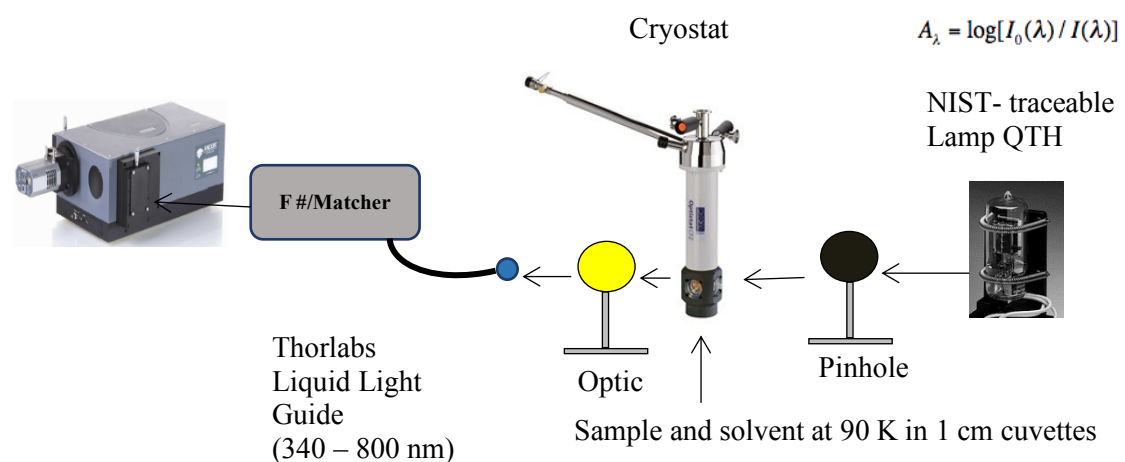


Figure 35: 90 K absorption spectroscopy set up for ruthenium quinoline complexes

The low temperature absorption spectra were collected using an Oxford Instruments OptistatCF Static Exchange Gas Continuous Flow Cryostat with liquid nitrogen as the cryogen was used at 90 K with NSG Precision Cells, Inc.).^{38, 80} The system used for this purpose is represented in Figure 35.

The temperature in the cryostat was controlled by an Oxford Instruments Intelligent Temperature Controller (ITC) 503S. Temperature was gradually decreased from ambient temperature to 90 K to prevent the quartz cuvette from fracturing and solvent-glass cracking. The cryostat requires two pumps: 1) Roughing pump (1×10^{-4} torr) for the inner

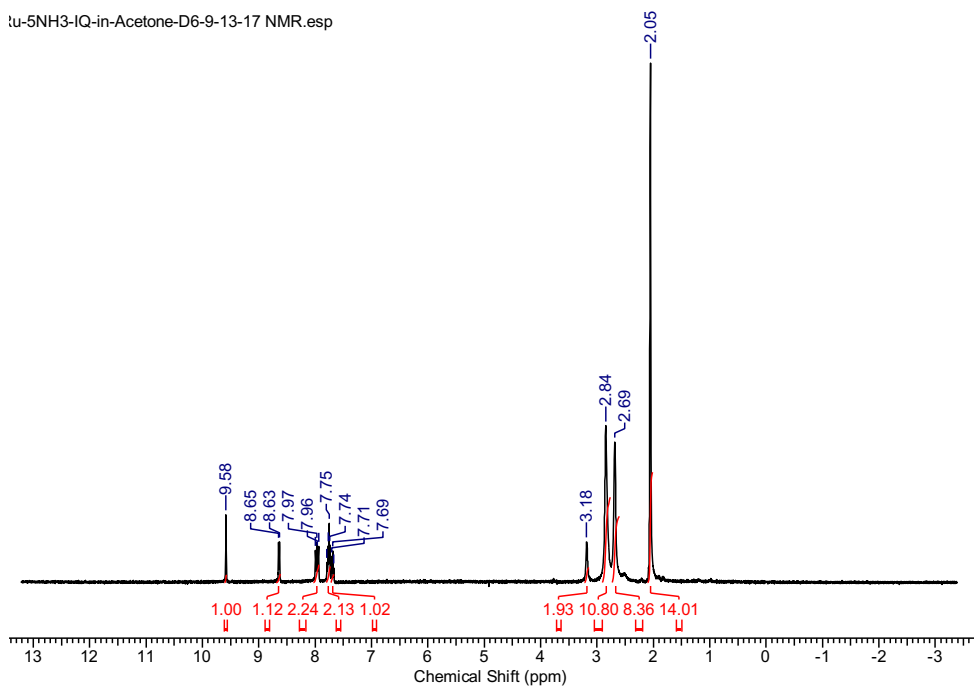
vacuum chamber (IVC) and 2) Turbo-pump ($10^{-3} - 10^{-5}$ mbar) for the outer vacuum chamber. The outer vacuum chamber is continuously pumped during the experiments for temperature stability.

3.3 RESULTS

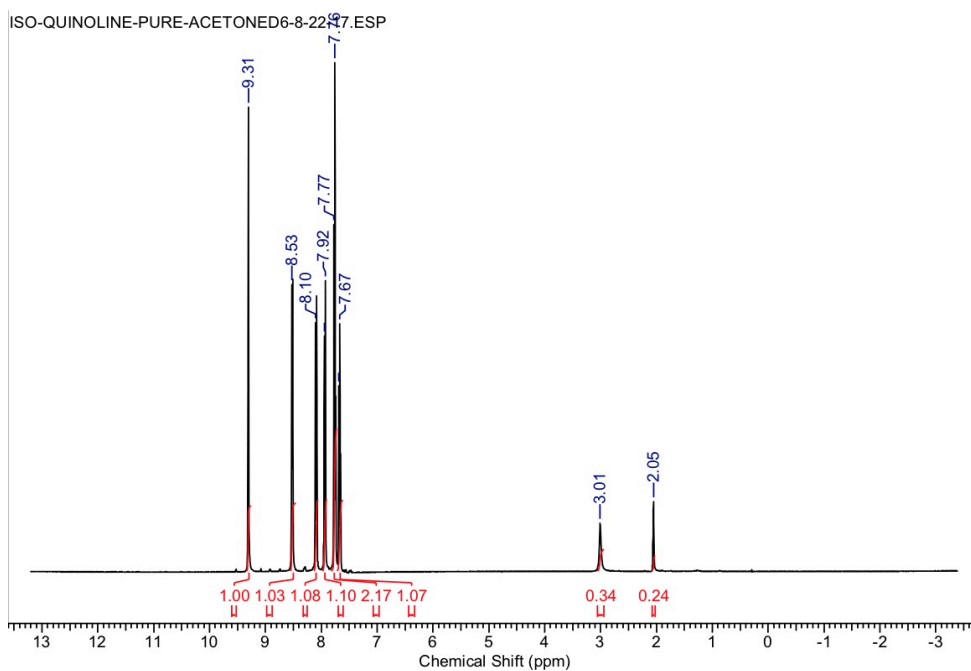
3.3.1 Proton Nuclear Magnetic Resonance Spectroscopy (^1H NMR)

The ^1H NMR spectra of the ruthenium pentaamine isoquinoline complex investigated is shown in Figure 36, 37; this spectrum was taken in acetone- D_6 . In this spectrum, the ammonia ligand peaks are split into a pseudo-doublet this could be H_2O in the up-field region with the centermost (largest) peak at 2.8 ppm. The ^1H NMR spectrum of ammonia should be a triplet (N has a nuclear spin of 1), but these are rarely resolved in complexes due to disorder in the relative proton coordinates in solution and other effects. In principle a complex with C_{4v} point group symmetry should have two peaks whose intensities are in a 4:1 ratio as a result of the different environments, however, the low symmetry quinoline ligand will reduce the complex symmetry and this might result in more peaks. The ratio of intensities of all the peaks assigned as ammonia to those of the quinoline peaks in the spectrum below is 3:1 and it should be about 2:1. This suggests that the sample has some $[\text{Ru}^{\text{II}}(\text{NH}_3)_5\text{L}]^{\text{m}+}$ impurity where L is not quinoline. In view of the instability (especially the photochemical instability) of this complex this is not surprising. Likewise, the multiplet that corresponds to the isoquinoline protons are shifted downfield at 7.6-8 ppm with two singlets that were pushed further in the downfield region. The pure isoquinoline ligand spectrum in Figure 37 shows all the aromatic protons in the down field region between 7.5-9.7 ppm.

tu-5NH3-IQ-in-Acetone-D6-9-13-17 NMR.esp

Figure 36: ^1H NMR of $[\text{Ru}(\text{NH}_3)_5\text{-ISO-Quinoline}]$

ISO-QUINOLINE-PURE-ACETONED6-8-22-2017.ESP

Figure 37: ^1H NMR of $[\text{ISO-Quinoline}]$

3.3.2. Absorption Spectra

a. Ambient and 90 K absorption spectra of [Ru(1-iso-TQA)(X)₂] Series of complexes

The ambient and 90 K UV-vis absorption spectra for both isomers of [Ru(1-iso-TQA)(X)₂] based complexes are shown in Figures 38 and 39. The lowest energy relatively intense absorption band of [Ru(1-iso-TQA)(CH₃CN)₂] is at 500 nm, while that of [Ru(1-iso-TQA)(CN)₂] is at 440 nm and for [Ru(1-iso-TQA)(SCN)₂] this band is at 470 nm. The lowest energy absorption bands of the 3-iso-TQA complexes are at somewhat higher energy with absorption maxima at: 440 nm for [Ru(3-iso-TQA)(CH₃CN)₂], and 450 nm for [Ru-3-iso-TQA-(CN)₂].

The ambient spectra are unusually broad and are clearly the result of the convolution of several similarly intense absorption bands. The component contributions are much better resolved in the 90 K absorption spectrum.

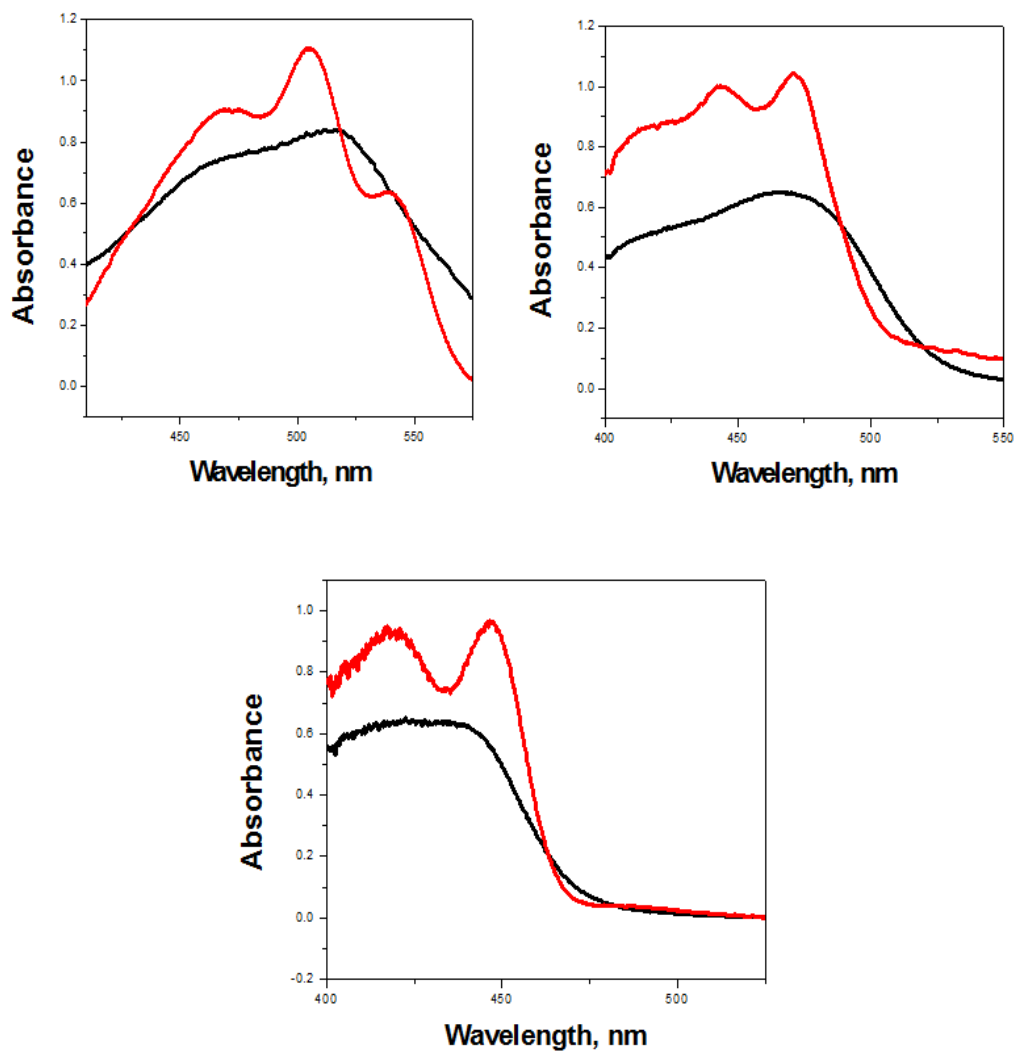


Figure 38. The normalized ambient and 90 K absorption spectra of $[\text{Ru}(1\text{-iso-TQA})(\text{X})_2]$ series. Top left if the spectrum for $[\text{Ru}(1\text{-iso-TQA})(\text{CH}_3\text{CN})_2]$; top right is for $[\text{Ru}(1\text{-iso-TQA})(\text{SCN})_2]$, middle bottom is for $[\text{Ru}(1\text{-iso-TQA})(\text{CN})_2]$. The black line represents the ambient condition absorption while the red line represents the 90 K absorption, all the absorption spectrum were taken in 4: 1 Ethanol: Methanol

b. Ambient and 90 K Absorption spectra of $[\text{Ru}(3\text{-iso-TQA})(\text{X})_2]$ complexes

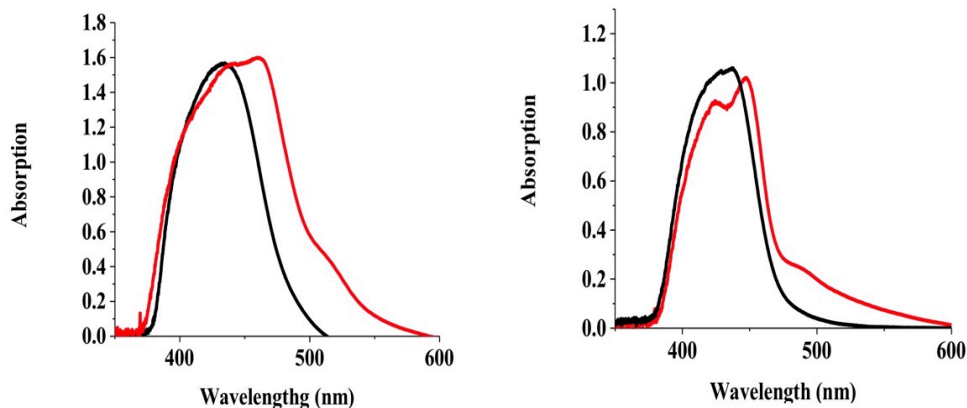


Figure 39: Ambient and 90 K UV-vis absorption comparison of $[\text{Ru}(3\text{-iso-TQA})(\text{NCCH}_3)_2]^{2+}$ left, $[\text{Ru}(1\text{-iso-TQA})(\text{CN})_2]$ right, in 4:1 ethanol: methanol. Black is the ambient spectrum and red is 90 K spectrum, spectra were determined in 4: 1 Ethanol: Methanol

c. Ambient and 77 K absorption of various ruthenium complexes

The ambient condition absorption spectrum of $[\text{Ru}(\text{NH}_3)_5(\text{isoquinoline})]$ is shown in the black curve in Figure 40. The maximum absorption of this complex is at 470 nm spectrum and there is a weaker peak at about 380 nm. The red spectrum is for the pure isoquinoline ligand which shows an absorption shoulder at about 450 nm.

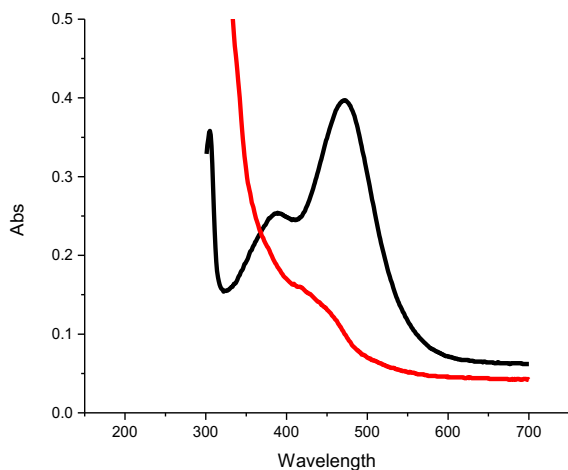


Figure 40: Ambient absorption of 10^{-4} M [Ru(NH₃)₅-Isoquinoline] and free isoquinoline ligand in 4:1 Ethanol: Methanol.

3.3.3. 77 K emission spectra

This section is shown the photophysical measurements of all complexes investigated in this project.

a. Comparison of the emission spectra of the [Ru(1-iso-TQA)(X)₂] and [Ru(3-iso-TQA)(X)₂] series of complexes.

The normalized 77 K emission spectra of the two isomers of [Ru(1-iso-TQA)(X)₂] series in alcohol are compared in Figures 41 and 42. These emission spectra all have unusually intense vibronic sidebands. The complexes of these two isomers have qualitatively similar emission envelopes, but quite different emission decay lifetimes.

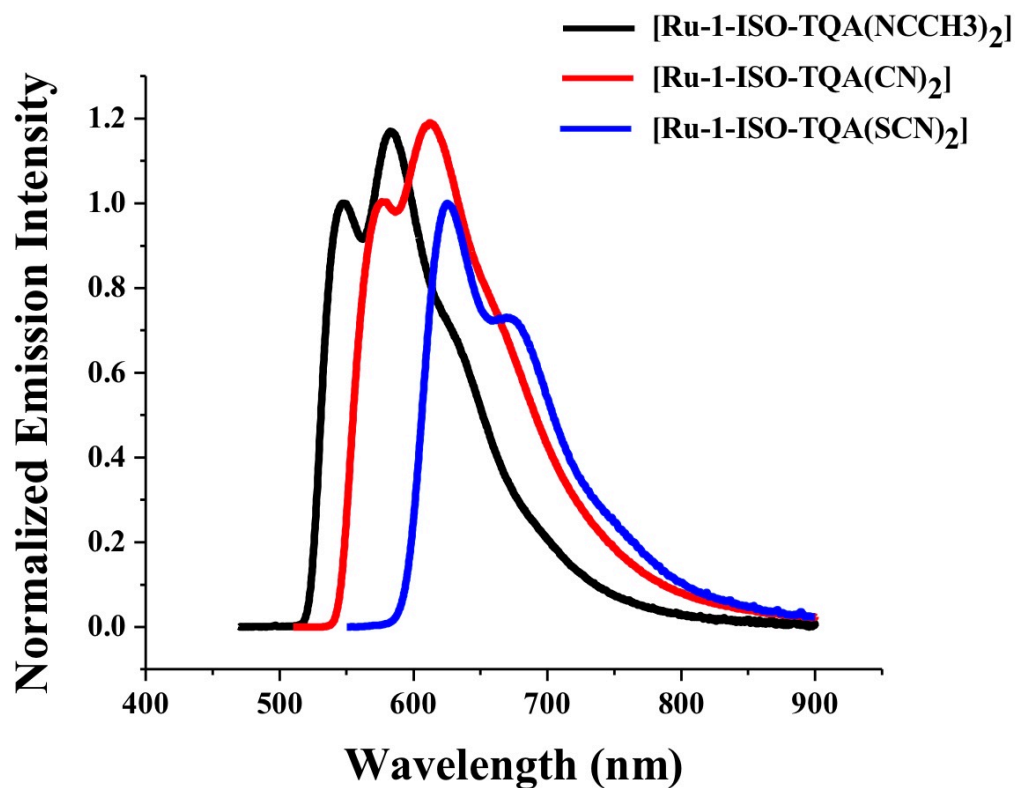


Figure 41. Normalized 77 K emission spectra of $[\text{Ru}(\text{1-iso-TQA})(\text{NCCH}_3)_2]^{2+}$, $[\text{Ru}(\text{1-iso-TQA})(\text{CN})_2]$ and $[\text{Ru}(\text{1-iso-TQA})(\text{NCS})_2]$. The emission spectra were in 4: 1 Ethanol: Methanol

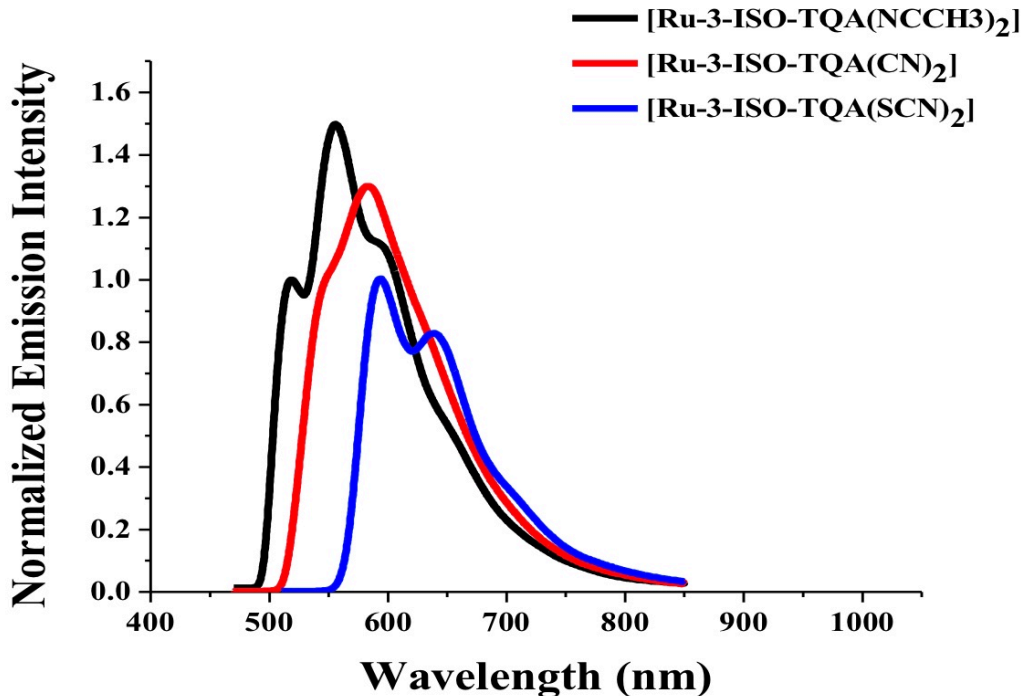


Figure 42. Normalized 77 K emission spectra of $[\text{Ru}(3\text{-iso-TQA})(\text{NCCH}_3)_2]^{2+}$, $[\text{Ru}(3\text{-iso-TQA})(\text{CN})_2]$ and $[\text{Ru}(3\text{-iso-TQA})(\text{NCS})_2]$. The emission spectra were obtained in 4: 1 Ethanol: Methanol.

b. 77 K emission spectra of $[\text{Ru}(\text{NH}_3)_5(\text{isoquinoline})]^{2+}$ complex

(i) The 77 K photochemistry of $[\text{Ru}(\text{NH}_3)_5(\text{isoquinoline})]^{2+}$.

This complex was very difficult to work with: it is difficult to purify, it emits very weakly, its emission overlaps with that of the free isoquinoline ligand and it photodecomposes at 77 K. Figure 43 shows typical 77 K emissions obtained in a butyronitrile solution after 8 min of 470 nm irradiation. These complicated spectra (compare the general bandshape with those above) illustrate the difficulties of working with this complex. The results are qualitatively similar in 77 K DMSO/water, butyronitrile and ethanol/methanol glasses. A few of these observations are presented here. For these emission measurements, the spectrometer had to be set so that it took 1 min of spectral

accumulation to capture an emission spectrum. The observation from the $[\text{Ru}(\text{NH}_3)_5(\text{isoquinoline})]^{2+}$ in butyronitrile shows that the free ligand emission intensity increases significantly during the irradiation time.

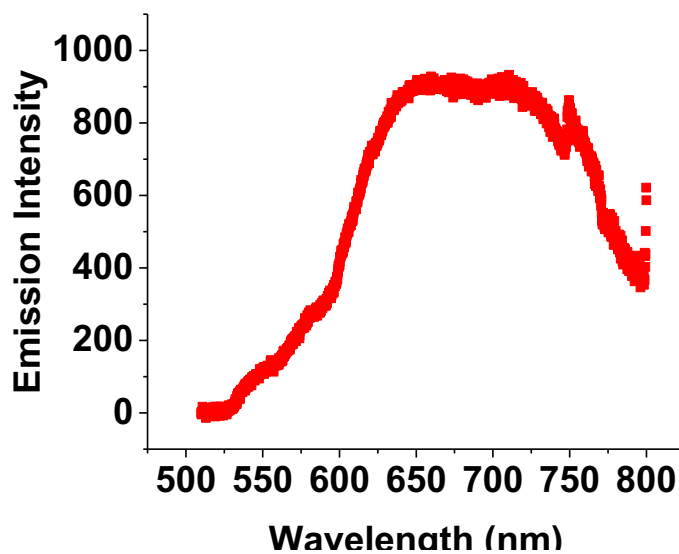


Figure 43: 77 K Emission of $6.2\text{E}-4 \text{ M}[\text{Ru}(\text{NH}_3)_5(\text{isoquinoline})]$ in butyronitrile using 470 excitation

77 K emission spectra of $[\text{Ru}(\text{NH}_3)_5\text{-isoquinoline}]$ are shown in Figure 44.

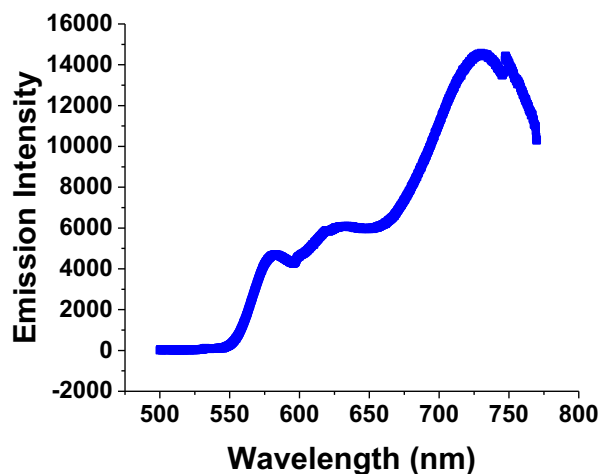


Figure 44: Emission spectra observed at 470 nm irradiation of $[\text{Ru}(\text{NH}_3)_5\text{-isoquinoline}]$ complex in butyronitrile at 77 K

The pure iso-quinoline ligand was found to emit at energies very close to the complex's emission. Figure 45 shows this emission in two different solvents.

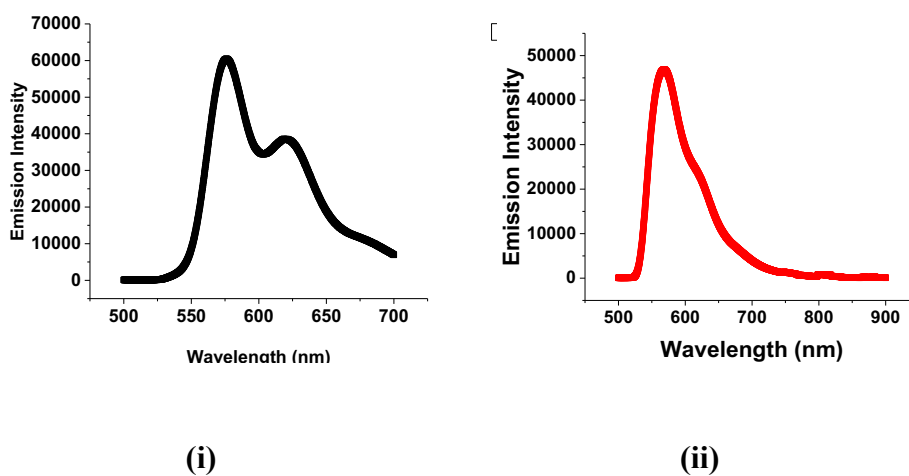


Figure 45. 470 nm 77 K irradiation of isoquinoline ligand in 4:1 ethanol : methanol, (i) and butyronitrile (i)

The $[\text{Ru}(\text{NH}_3)_5(\text{isoquinoline})]^{2+}$ excited state emission in ethanol : methanol is shown in Figure 46.

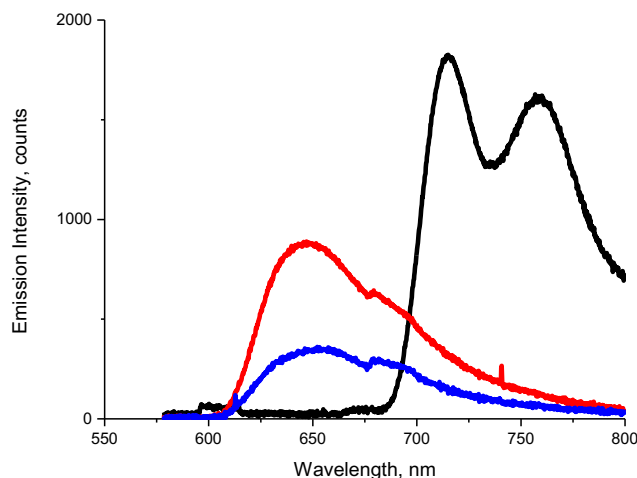


Figure 46. Comparison of the complex and free ligand emissions in ethanol: methanol. Black line represents the 77 K emission using 470 nm excitation; red line represent the 77 K emission of the isoquinoline free ligand at 405 nm excitation; blue line represent the 77 K of the free ligand using 470 nm excitation.

3.3.4. 77 K life-time measurements

The 77 K emission decay for the two isomers of $[\text{Ru}(\text{iso-TQA})(\text{X})_2]^{2+}$ in alcohol are shown in Figures 47 and 48. The decay measurements were done with mono exponential fits, the residuals are shown in red. In Figure 47 the longest lifetime was recorded for $[\text{Ru}-(1\text{-iso-TQA})(\text{CH}_3\text{CN})_2]^{2+}$ where the mean decay lifetime was determined to be 145 μs , the next longest lifetimes were determined to be 94, and 77.5 μs for $[\text{Ru}(3\text{-iso-TQA})(\text{CN})_2]^{2+}$ and $[\text{Ru}(1\text{-iso-TQA})(\text{CN})_2]^{2+}$, respectively. In addition, the lifetimes were determined to be 25 and 17.6 μs for $[\text{Ru}(3\text{-iso-TQA})(\text{SCN})_2]^{2+}$ and $[\text{Ru}(1\text{-iso-TQA})(\text{SCN})_2]^{2+}$, respectively. The shortest lifetime was determined to be 3.6 μs for $[\text{Ru}(3\text{-iso-TQA})(\text{Cl})_2]^{2+}$. The observations are summarized in Table 19.

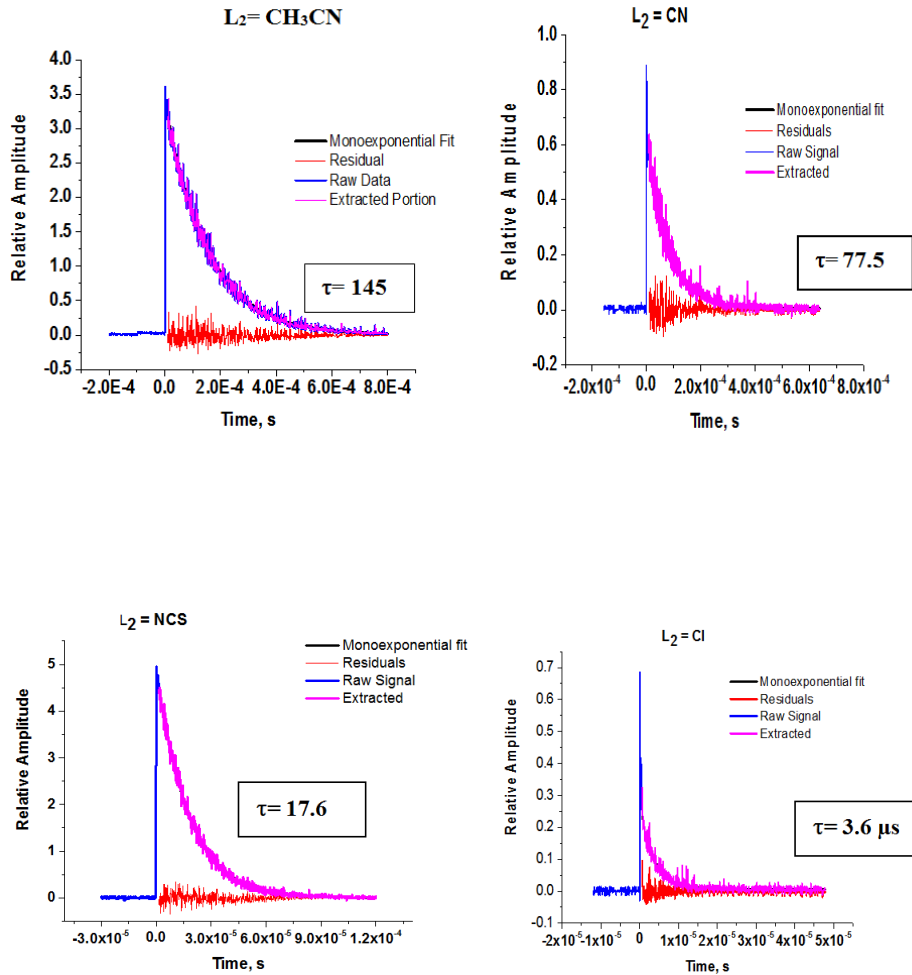


Figure 47. 77 K Lifetime measurements of [Ru(1-iso-TQA)(NCCH₃)₂] top left, [Ru(1-iso-TQA)(CN)₂] top right, [Ru(1-iso-TQA)(NCS)₂] bottom left, and [Ru(1-iso-TQA)(Cl)₂] bottom right.

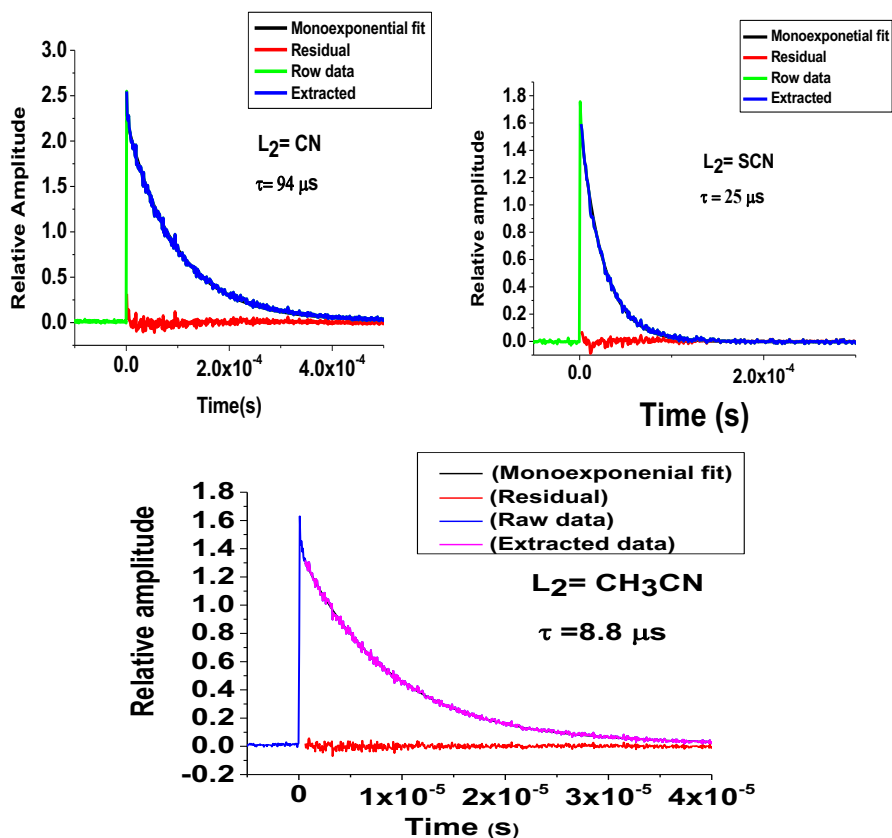


Figure 48. 77 K Lifetime Measurements for $[\text{Ru}(\text{3-iso-TQA})(\text{L})_2]^{m+}$ Series in 4:1 ethanol: methanol. Top left is the emission decay for $[\text{Ru}(\text{3-iso-TQA})(\text{CN})_2]^{m+}$, $[\text{Ru}(\text{3-iso-TQA})(\text{SCN})_2]^{m+}$ top right, and bottom is the emission decay for $[\text{Ru}(\text{3-iso-TQA})(\text{CH}_3\text{CN})]^{m+}$

3.3.5. Comparison of the spectroscopic properties of the triplet metal to ligand charge transfer ($^3\text{MLCT}$) various Ru-aromatic complexes

Table 19. Quantum yields, radiative and non-radiative rate constants of various [Ru(TQA)(X)₂], [Ru(NH₃)₅(isoquinoline)], and [Ru(NH₃)₅(phenyl-pyridine)]

Complex	$h\nu_{\text{abs(max)}} \text{ (cm}^{-1}/10^3 \text{ Ambient Temp)}$	$h\nu_{\text{em(max)}} \text{ (cm}^{-1}/10^3 \text{ 77 K)}$	$k_{\text{obs}} \text{ } \mu\text{s}^{-1d} \text{ 77 K}$	Quantum yields at 77 K	$k_{\text{RAD, ms}^{-1}}$	$k_{\text{NRD, ms}^{-1d}} \text{ 77 K}$
$\text{Ru(1(ISO-TQA)(NCCH}_3)_2)^{2+b}$	23.8	18.3	0.0069	0.452±0.016	3.1	3.8
$[\text{Ru(3-ISO-TQA)(NCCH}_3)_2]^{2+b}$		19.1	0.1136	0.52	59	50
$[\text{Ru(1-ISO-TQA)(CN)}_2]^b$	21.3	17.3	0.0129	0.26±0.049	3.4	9.5
$\text{Ru(3-ISO-TQA)(CN)}_2]^b$		18.3	0.01064	0.21	2.23	8.4
$[\text{Ru(1-ISO-TQA)(SCN)}_2]^c$	20.8	16	0.0568	0.499±0.064	28	29
$\text{Ru(3-ISO-TQA)(SCN)}_2]^c$		16.9	0.04			
$[\text{Ru(NH}_3)_5\text{isoQ}]^{2+ b}$		14	~30			
$[\text{Ru(NH}_3)_5(\text{phpy})]^{2+}_{91}$	22.32	13.02	1.8	0.00044(4)	0.8 ± 0.1	1,800

^a $k_{\text{obs}} = 1/\tau_{1/2}$ ^b4:1 Ethanol :Methanol, this work ^c Butyronitile; ^dTQA = tris(isoquinolin-1-ylmethyl)amine .

3.4. DFT Modeling

3.4.1 Calculated bond dissociation energies of pentaammine-Ru^{II} complexes with monodentate quinolone ligands

Since we unable to synthesize [Ru(NH₃)₅(quinolone)] after many trials with different synthetic procedures, DFT calculations were done to investigate whether there were any issues with the coordination sphere or bond energy of the target complexes. The

DFT calculations indicated that the Ru-quinoline bond disassociation energy (BDE) was about -5 kcal/mol smaller than the Ru-py BDE of the $[\text{Ru}(\text{NH}_3)_5\text{py}]$ complex.

Table 20. Calculation of The Bond Energies of $[\text{Ru}(\text{NH}_3)_5\text{L}]$, L = Quinoline or Iso-Quinoline ^a

Ligand	Complex	Dissociation energy of ligand (kcal/mol)	(Dissociation energy relative to py), ΔE (kcal/mol)
Pyridine	$[\text{Ru}(\text{NH}_3)_5\text{-py}]$	25.05	0.0
Quinoline	$[\text{Ru}(\text{NH}_3)_5\text{-Q}]$	19.97	-5.08
Iso-Quinoline	$[\text{Ru}(\text{NH}_3)_5\text{-Iso-Q}]$	25.06	0.01

^a Calculations done in collaboration with Dr. Yi-Jung Tu.

3.4.2. Excited state modeling done for this project by Dr. Yi-Jung Tu.

(a) **Singlet MLCT excited states.** The TD-DFT calculations for singlet excitation of ground-state of $[\text{RuTQA}(\text{ACN})_2]$ were performed with the B3PW91 functional and the results are summarized in Table 21. The calculated and experimental absorption spectra are compared in Figure 50.

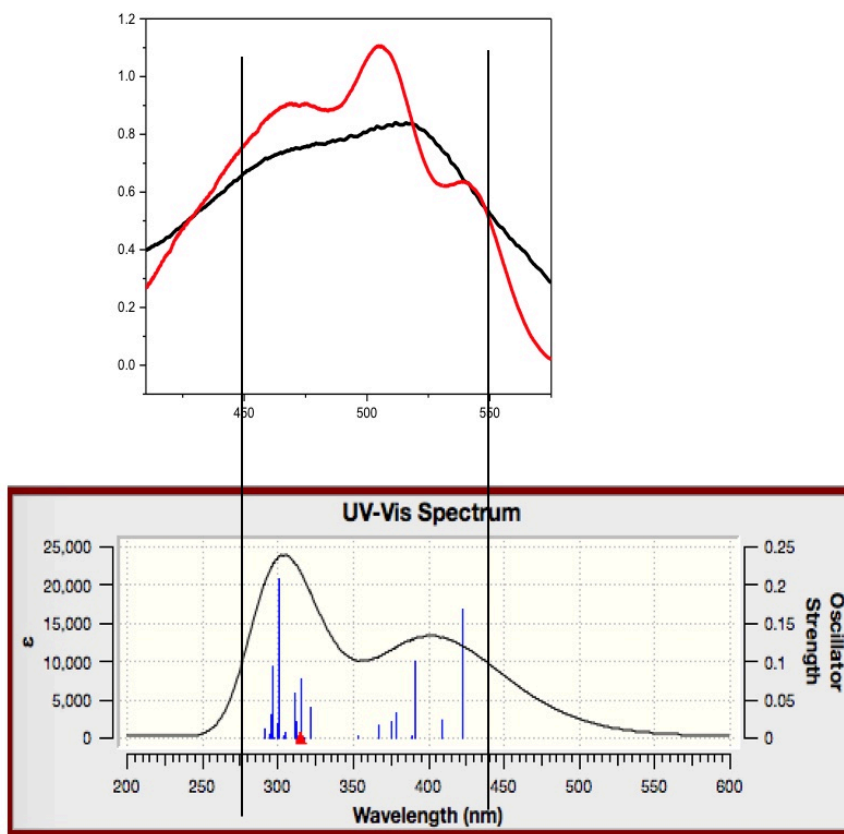
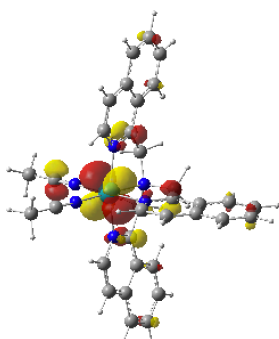
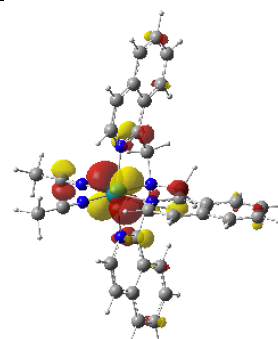
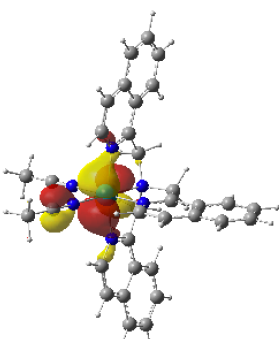
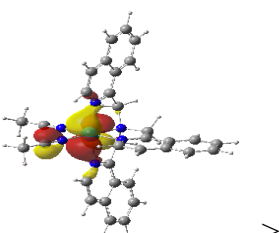
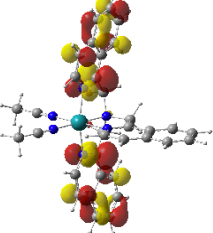


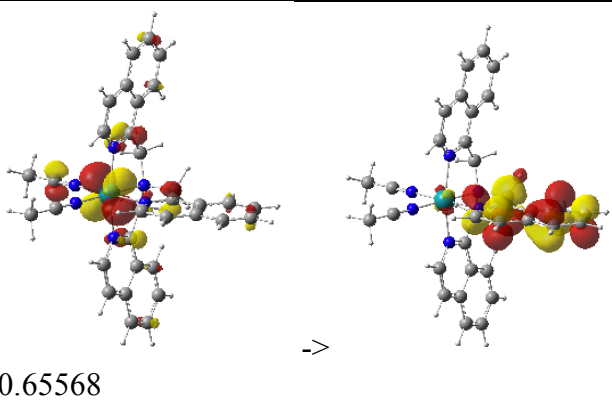
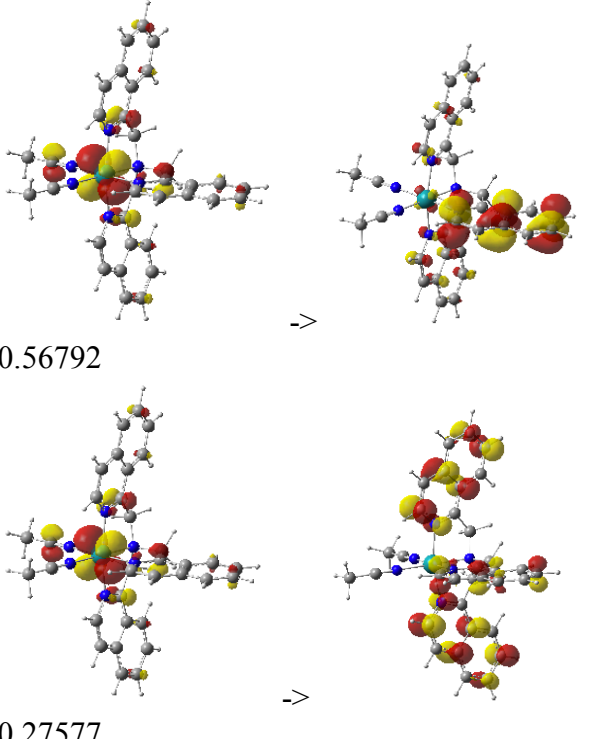
Figure 49. Comparison of calculated (lower “UV-Vis Spectrum”) and experimental (upper; black curve at 300 K and red curve at 90 K) spectra for Ru(TQA)(ACN)₂. The calculated energies are about 0.5 eV higher energy than the observed peaks

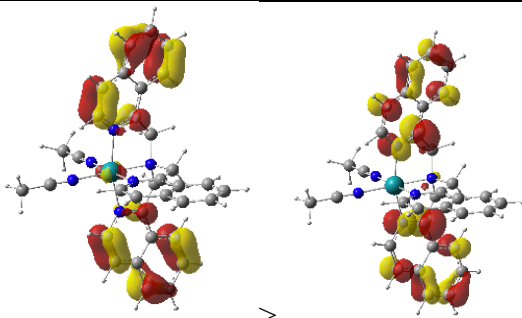
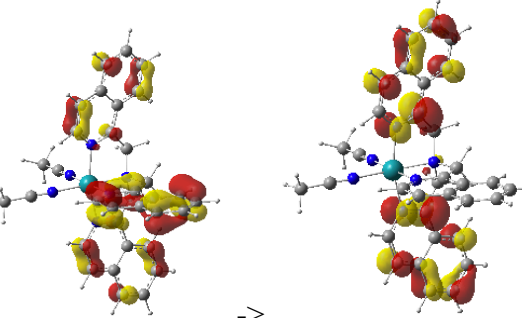
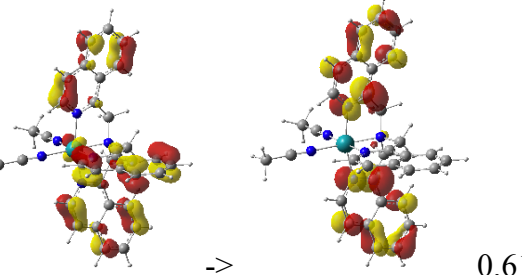
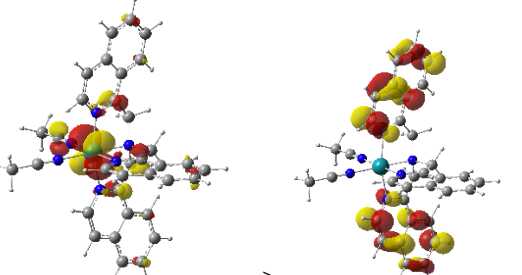
The bandshapes of the observed and calculated spectra are very different. Part of this arises from a difference in the observed and assumed (for the calculated spectra) bandwidths. There may be an issue with the relative oscillator strengths calculated for multi-transition absorption bands. The calculated energy differences between the calculated transitions with the largest oscillator strengths have much larger energy differences than those between the observed absorption peaks. Possible assignment of the 90 K peaks: Lowest energy MLCT transition with the electron in the excited state acceptor

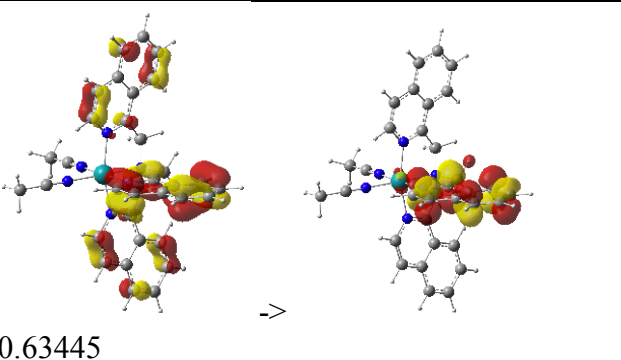
SOMO delocalized over the equivalent (more or less) quinoline moieties; the central band is likely an MLCT transition with the electron in an excited state acceptor SOMO that is localized on the unique quinoline moiety; and the highest energy band is likely an inter-quinoline ligand CT transition (mixed with a small amount of MLCT character. The dominant, lowest energy transition seems to have a metal-centered d_{xy} -type of orbital. All of the components of the observed “MLCT” absorption appear to be mixtures of different diabatic electronic configurations.

Table 21. Calculated $^1\text{MLCT}$ energies, oscillator strengths and Natural transition orbitals of the SOMOs for the $S_0 \rightarrow S_n$ transitions of $[\text{Ru}(\text{TQA})(\text{ACN})_2]$

Excited state	eV	nm	f	Orbital transition Donor	Acceptor
1	2.9314	422.95	0.1686		
				0.68990	
2	3.0354	408.46	0.0230		
				0.69059	

3	3.1744	390.57	0.1004	 <p>0.65568</p>
4	3.1909	388.55	0.0024	
5	3.2731	378.79	0.0321	
6	3.3010	375.60	0.0220	
7	3.3793	366.89	0.0051	
8	3.3815	366.65	0.0171	
9	3.5046	353.77	0.0015	
10	3.8513	321.93	0.0387	
11	3.8983	318.05	0.0003	
12	3.9292	315.55	0.0771	 <p>0.56792</p> <p>0.27577</p>
13	3.9723	312.12	0.0211	

14	3.9824	311.33	0.0584	 - 0.30569 >  -> 0.38039
15	3.9875	310.93	0.0429	
16	4.0720	304.48	0.0074	
17	4.0797	303.90	0.0030	
18	4.1247	300.59	0.2076	 -> 0.61292  -> 0.24011
19	4.1339	299.92	0.0188	
20	4.1601	298.03	0.0007	

21	4.1783	296.73	0.0943	 0.63445
22	4.2013	295.11	0.0308	
23	4.2131	294.28	0.0038	
24	4.2502	291.71	0.0113	
25	4.2518	291.61	0.0107	

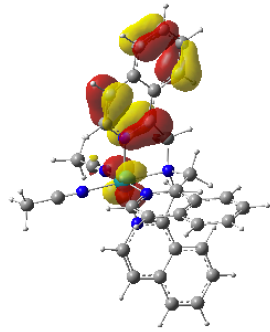
(b) Triplet excited states Natural transition orbitals of the SOMOs.

The NTOs for triplet excited states of $[\text{Ru}(\text{TQA})(\text{ACN})_2]$ with the $^3\text{MLCT}$ geometry are shown in Figure 50. All the triplet states appear to be more complex than the singlet states in Figure 50. The T_0 state is the most important of these since it would correspond to the emitting state and it appears to be a remarkable nearly 1:1 mixture of idealized diabatic MLCT and $\pi\pi^*$ excited states and its metal centered partly vacant orbital has approximately d_{xz} symmetry.

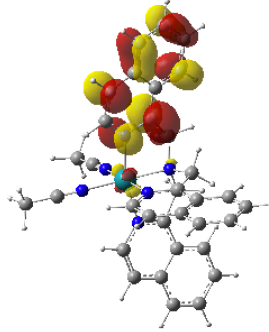
T₀: 1.7793 eV 696.80 nm f=0.0000

Donor

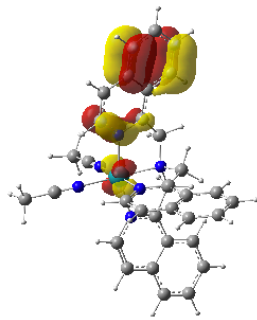
Acceptor



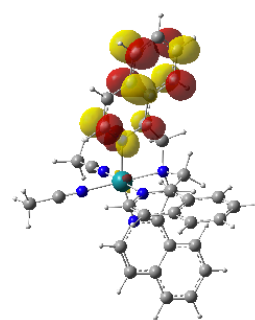
->



0.99235

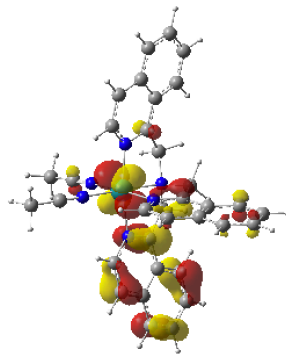


->

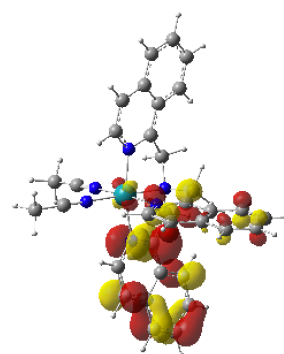


0.02879

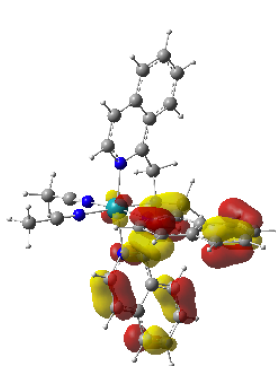
T₁: 2.4407 eV 507.98 nm f=0.0000



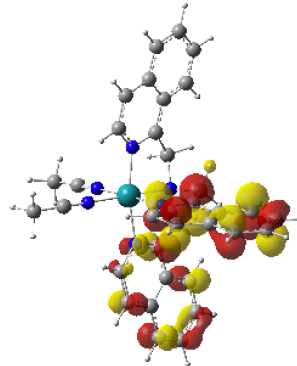
->



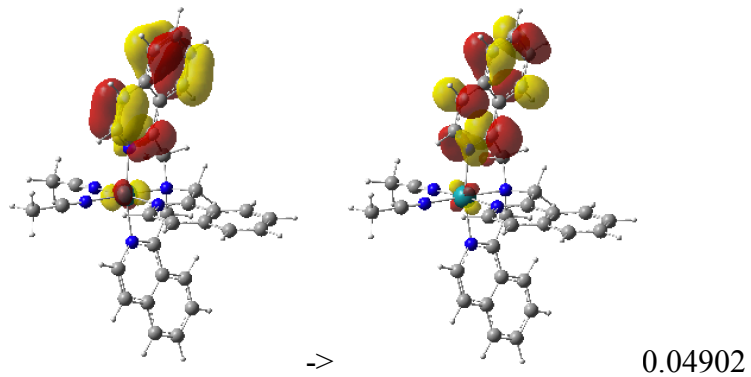
0.71338



->



0.19158



T₂: 2.5136 eV 493.25 nm f=0.0000

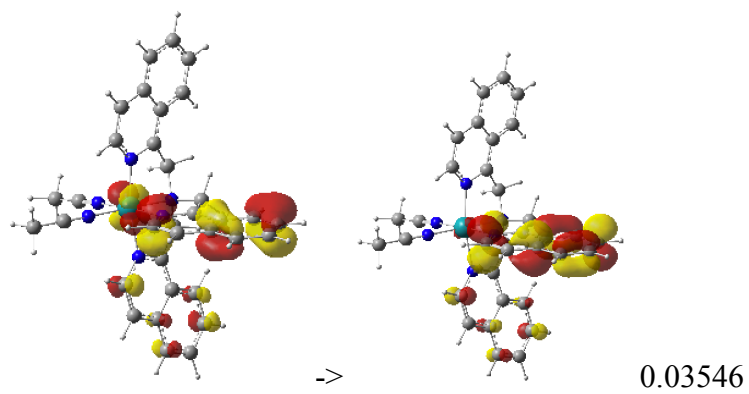
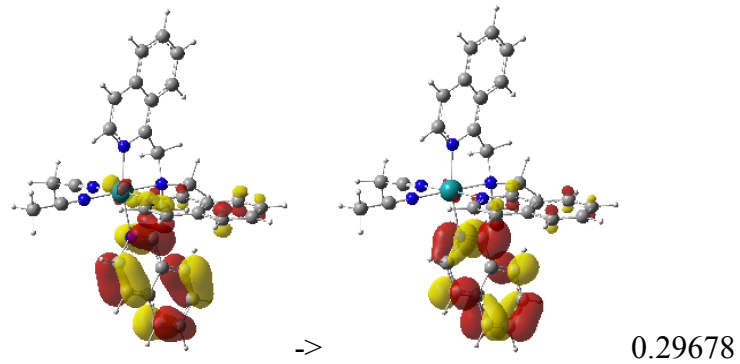
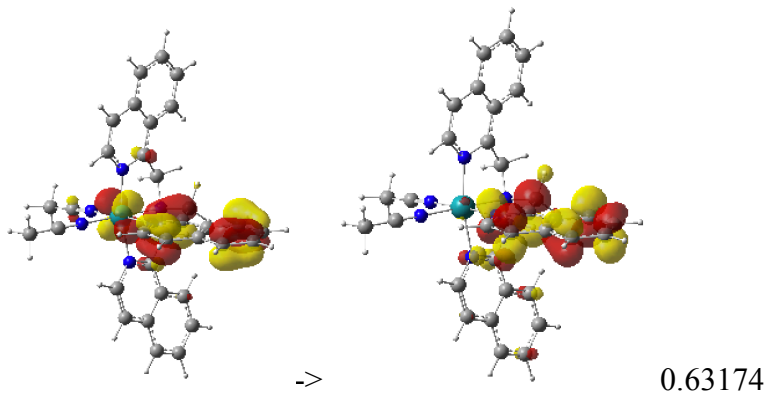


Figure 50. Calculated triplet excited state energies, oscillator strengths and Natural transition orbitals of the SOMOs of [Ru(TQA)(ACN)₂]

(c) Some comparisons of the calculated triplet state electronic structures of [Ru(TQA)(X)₂] complexes with different ancillary ligands.

In a classical organic chromophore the emitting state is typically the lowest energy excited state. However, in Ru-Ar complexes this is not always the case and there are often states with lower energies than the ones whose emission is detected,^{16,17,23,33} These are often metal-centered excited states (MC) as found in the DFT modeling summarized in Figure 51 and Table 22.^{38, 57-58, 80}

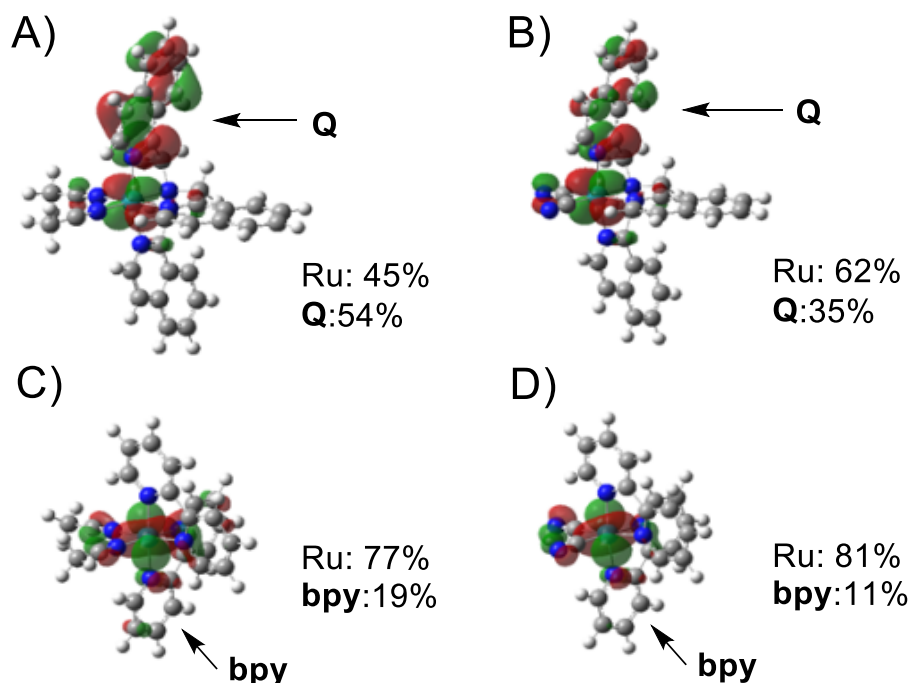


Figure 51. Comparison of donor SOMOs (isovalue=0.03 a.u.) and orbital contributions (%) for the lowest energy CT state of TQA and bpy Ru complexes with the ancillary ligands: A) [Ru(TQA)(MeCN)₂]²⁺; B) [Ru(TQA)(CN)₂]; C) [Ru(bpy)₂(MeCN)₂]²⁺; D) [Ru(bpy)₂(CN)₂] in the ³CT optimized geometries

Table 22. lists the relative energies of the $^3\text{MLCT}$ and the ^3MC states. The ^3MC energies calculated for the cyanide complexes were close to or slightly higher than those of the $^3\text{MLCT}$ states, while the MeCN complexes have significantly lower energy ^3MC states.

Table 22. Relative energies of the $^3\text{MLCT}$ and ^3MC states and orbital contributions (%) of Ru and ligands to the SOMOs of A) $[\text{Ru}(\text{TQA})(\text{MeCN})_2]^{2+}$; B) $[\text{Ru}(\text{TQA})(\text{CN})_2]$; C) $[\text{Ru}(\text{bpy})_2(\text{MeCN})_2]^{2+}$; D) $[\text{Ru}(\text{bpy})_2(\text{CN})_2]$

			ΔE^a $\text{cm}^{-1}, \times 10^3$	SOMO(1)		SOMO(2)	
				Ru	Ligand ^b	Ru	Ligand ^b
A)	$^3\text{MLCT}$	(T_3)	0	45	54	3	97
	^3MC	(T_0)	-4.5	78	17	77	17
	^3MC	(T_1)	-3.3	77	18	91	8
	^3MC	(T_2)	-2.8	75	22	86	9
B)	$^3\text{MLCT}$	(T_1)	0	62	35	3	97
	^3MC	(T_0)	-1.2	75	17	81	8
C)	$^3\text{MLCT}$	(T_1)	0	78	19	2	98
	^3MC	(T_0)	-3.7	92	6	74	16
D)	$^3\text{MLCT}$	(T_0)	0	81	11	2	98
	^3MC	(T_1)	2.1	91	2	73	22

^a Energies of the $^3\text{MLCT}$ states are set to be zero. Energies of the ^3MC states are compared to those of the $^3\text{MLCT}$ states. ^b Ligand = TQA or bpy.

Previous calculations of Mazumder, et al.⁹² for $[\text{Ru}(\text{MeCN})_4\text{bpy}]^{2+}$ found that the energy barrier for the internal conversion can be small so that the ^3MC states can be thermally accessed at ambient temperature. These results are consistent with the difficulty in finding an ambient emission from these complexes and with the previous work of CH_3CN photodissociation from $[\text{Ru}(\text{TQA})(\text{MeCN})_2]^{2+}$ at room temperature.⁹³

3.5. Ambient and 77 K Life-time measurements of cathepsin L (CSTL) inhibitors bearing Re(I) and Ru(II)

This work was done to characterize the $^3\text{MLCT}$ of cathepsin L (CSTL) inhibitors bearing Re(I) and Ru(II), work done with professor corporation with Jeremy Kodanko group.

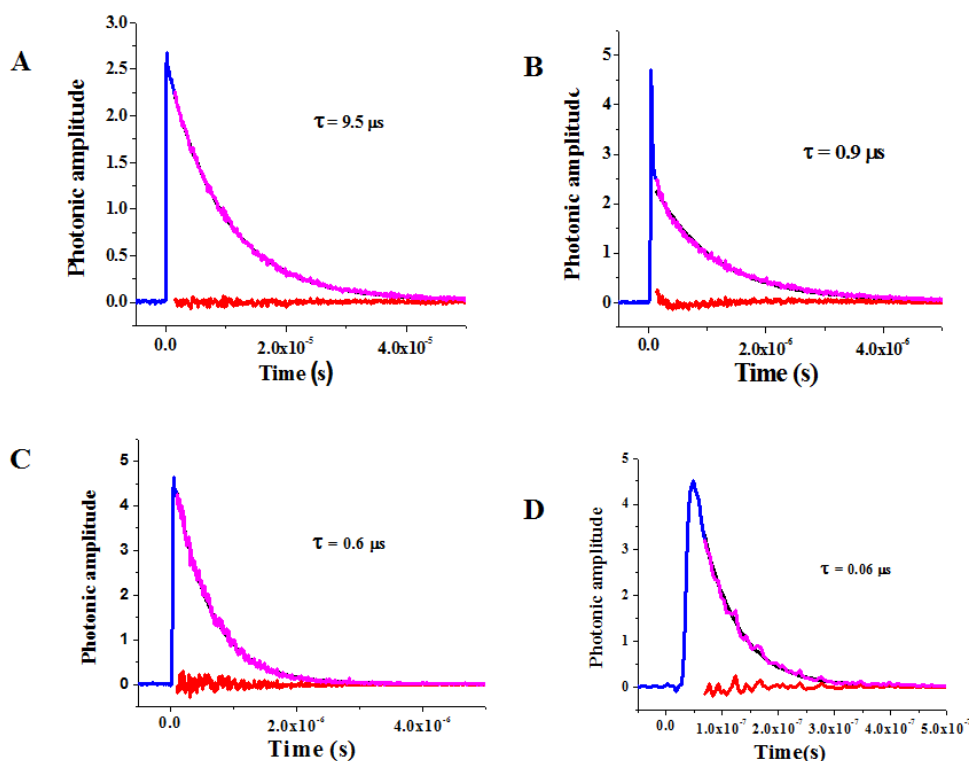


Figure 52: Emission decay of [MH-3-110] and [MH-3-55] concentration 47.5 μM and 4.09 μM respectively at ambient and 77 K (frozen solution)² in potassium phosphate buffer 50 mM, PH 7.4 and 10% DMSO solvent using 337 N nm pulsed excitation monitored at 543 and 631. (A) [MH-3-110] at 77 K; (B) [MH-3-55] at 77 K. (C) [MH-3-110] at ambient condition. (D) [MH-3-55] at ambient condition. The mono exponential fit (black) and the extracted data (pink) are indistinguishable; residuals are in red. The samples were probably microcrystalline at 77K. A fast decay component with about 10% of the substrate amplitude was probably mostly due to the instrument response to scattered excitation light, but it could also contain contribution from heterogeneities or impurities. Exponential decay fittings performed in Origin; IRF= 12 ns.

Table 23: 77 K and ambient condition lifetime measurements of [MH-3-110] and [MH-3-55] with 337 nm^a excitation in potassium phosphate buffer 50 mM, PH 7.4 and 10% DMSO solvent monitored 543 and 631 respectively.

Complex ^b	Lifetime (μ s) ^c		Initial amplitude (A) ^d	
	77K	Ambient condition	77 k	Ambient condition
[MH-3-110]	9.5 \pm 0.02 ^e	0.6 \pm 0.02	2.6	5.1
[MH-3-110]	9.5 \pm 0.02	0.6 \pm 0.02	2.6	5.1
[MH-3-110]	9.5 \pm 0.02	0.6 \pm 0.02	2.6	5.2
[MH-3-55]	0.9 \pm 0.1	0.06 \pm 0.02	2.8	9.6
[MH-3-55]	0.9 \pm 0.1	0.06 \pm 0.02	2.8	9.7
[MH-3-55]	0.9 \pm 0.1	0.06 \pm 0.02	2.8	9.9

^a Nitrogen laser excitation wavelength was 337 nm; ^b complex names were abbreviated as [MH-3-110] for and [MH-3-55]; ^c lifetime measurements were determined three times and recorded in microseconds; ^d(A) is the initial amplitude; ^e Standard errors.

3.6. DISSCUSSION AND CONCLUSIONS

The Ru-quinoline chromophores have some unique spectroscopic and photophysical properties. Thus, the lowest energy absorption bands of the Ru-TQA complexes are not typical MLCT absorptions, but appear to be the convolution of several different, near in energy absorption bands, while the vibronic “sidebands” dominate the emission spectra of the Ru-TQA complexes with the highest energy emissions. This has little if any precedent among reported MLCT emission spectra. DFT modeling suggests that the Ru-TQA excited states that involved in the lowest energy absorption component

and in the observed emission have very different electronic configurations and that the emitting excited state has at least as much quinolone- $\pi\pi^*$ character as (Ru-quinoline)-MLCT character. Such an electronic configuration of the emitting state is consistent with the unusually intense vibronic sidebands.

Since the Ru-quinoline complexes with high energy emissions seemed to have such unusual spectroscopic properties and since the configurational mixing between $^3\text{MLCT}$ and $^3\pi\pi^*$ excited states is strongly dependent on the $^3\text{MLCT}$ energies in Ru-bpy complexes,^{38, 79, 83, 86} a spectroscopic comparison between the Ru-TQA complexes one or more complexes with lower energy emissions is likely to provide a useful perspectives of the Ru-quinoline excited state properties. The $[\text{Ru}(\text{NH}_3)_5(\text{quinoline})]^{2+}$ complexes were selected for this purpose. While these complexes were more difficult to handle than anticipated, the observed spectra provide some useful perspectives.

3.6.1 Absorption spectroscopy and the singlet excited states.

The very broad absorption bands observed for the Ru-TQA chromophores at room temperature are partially resolved into 2-5 components at 90 K. The DFT modeling of the $[\text{Ru}(3\text{-iso-TQA})(\text{NCCH}_3)_2]^{2+}$ complex indicates that the observed visible-UV absorptions arise from a mixture of MLCT, intra-TQA ligand and inter-TQA ligand absorptions. For the 3-iso-TQA complexes the 90 K spectra show three at least partly resolved absorption bands. Since the DFT modeling found many transitions in this region, not all of the observed absorptions can be simply described, but the lowest energy transition of $[\text{Ru}(3\text{-iso-TQA})(\text{NCCH}_3)_2]^{2+}$ is readily assigned as a nearly classical $\text{S}_0 \rightarrow ^1\text{MLCT}$ transition with the two equivalent quinolone moieties of the complex acting as acceptors. This is the basis

for assigning the transitions of the remaining complexes; see Table 24. The higher energy transitions of the 3-iso-TQA complexes are difficult to assign with confidence, but they must involve significant ligand→ligand contributions. The calculated spectrum shown in Figure 50 does not clearly show the expected three dominant transitions that are observed and it is spread over a significantly larger energy range than is observed. Thus, it appears that the calculated S_0 →ligand transition energies differ more from those observed than do the calculated S_0 →MLCT energies. This might be a consequence of the functional used for the calculation.

Table 24. Summary of absorption spectra of the complexes

Acceptor Ligand	Ancillary Ligands	Abs. Max. nm	Probable Assignment	Calc. Max., nm	Aprox. Ru Orbital in SOMO
3-iso-TQA	(AN) ₂	541	MLCT (S ₁)	423	(dπ) _{xz}
		505	MLCT (S ₃)	391	
		469	MLCT, Inter(Q), Intra(Q) (S ₁₄ , S ₁₄ , S ₁₈)	300-315	
	(NCS ⁻) ₂	466	MLCT		
		441			
		~420			
	(CN ⁻) ₂	443	MLCT		
		429			
	1-iso-TQA	(AN) ₂	(496) _{sh}		
450			MLCT		
426					
(CN ⁻) ₂		(517) _{sh}			
		437	MLCT		
		467			
1-iso-Q	(NH ₃) ₅	710-715	MLCT		
		388			
1-iso-Q	(free ligand)	(435) _{sh}	nπ*		

The 90 K $[\text{Ru}(1\text{-iso-TQA})(\text{X})_2]^{m+}$ absorption spectra also show multiple components, but with more significant low and high energy shoulders. Since there are so many possible transitions in the TQA complexes, the observation of absorption shoulders is not surprising. The lowest energy dominant absorption is assigned as predominantly an $S_0 \rightarrow {}^1\text{MLCT}$ transition analogous to $[\text{Ru}(3\text{-iso-TQA})(\text{NCCH}_3)_2]^{2+}$.

The $[\text{Ru}(\text{NH}_3)_5(1\text{-iso-quinoline})]^{2+}$ absorption spectrum is simpler than those of the TQA complexes, at least partly because there are no inter-ligand transitions. That two absorption bands are observed for this complex suggests that some internal quinoline-ligand transitions contribute, but this is not yet established.

The free ligand also absorbs in the high energy visible region and a weak shoulder is observed at 435 nm which is almost certainly the $n \rightarrow \pi^*$ absorption that is typical of this class of aromatic imines.⁹⁴ When the quinoline ligand is coordinated to Ru^{II} the nitrogen “non-bonding” electron pair of the ligand form a donor-acceptor bond to the metal and the $n \rightarrow \pi^*$ transition is expected to be at higher energy.

3.6.2 Emission spectroscopy and the triplet excited states.

The DFT modeling of the lowest energy $[\text{Ru}(3\text{-iso-TQA})(\text{NCCH}_3)_2]^{2+}$ triplet excited state indicates that the emitting state has an extended aromatic electronic configuration that can be approximated as a nearly equal combination of MLCT and $\pi\pi^*$ character. The unusually large ligand contribution to the electronic configuration of this excited state provides a very reasonable explanation for the observation that the vibronic contributions to the emission spectrum are much larger than is usually observed for ${}^3\text{MLCT}$ emissions. Thus, in contrast to the Ru-TQA complexes, the $\text{Ru}(\text{bpy})_2$ species show less

contribution (11-19%) from the bpy ligand in the metal-centered SOMOs as illustrated in Figure 51, and the $^3\text{MLCT}$ states of Ru-(bpy) chromophores have much smaller contributions from the $\pi\pi^*$ states.⁷⁹ Since the $\pi\pi^*$ state is a longer-lived than a pure $^3\text{MLCT}$ state, this greater configurational mixing could be the reason behind the longer excited state lifetimes for the Ru-TQA species. Among the four complexes studied by DFT, $[\text{Ru}(\text{TQA})(\text{MeCN})_2]^{2+}$ displays the highest mixing, has the most prominent vibronic sidebands and has the highest energy emission. If the energy of the acceptor ligand $\pi\pi^*$ excited state is only a very weak function of the ancillary ligands, then the amount of mixing, which will increase as the energy difference between the MLCT and $\pi\pi^*$ states decreases; that it will increase as the $^3\text{MLCT}$ energy increases as has been observed for the Ru-bpy chromophores.^{38, 79, 83-84, 86} This effect is clearest for the $[\text{Ru}(\text{NH}_3)_5\text{isoquinoline}]^{2+}$ complex which is the lowest energy emitter of the Ru-quinoline chromophores.

3.6.3 Triplet excited state emission quantum yields, relaxation rates and excited state properties.

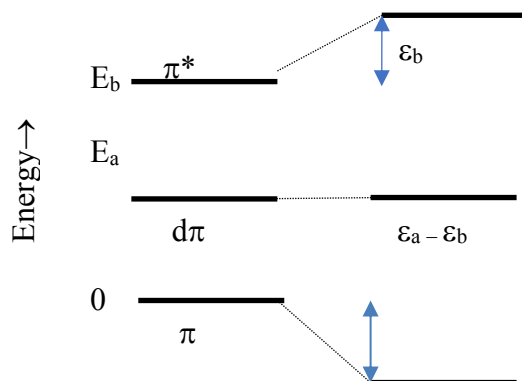
The emission spectra of the Ru-TQA chromophores are relatively well resolved, their emission yields are relatively large and their lifetimes are relatively long for Ru-Ar complexes despite the DFT-based excited states being lower in energy. This is fairly common with the Ru-Ar class of complexes and it apparently arises because the ^3MC states are so much more distorted than the Ru-bpy, Ru-MDA, etc., complexes with their distortions in different nuclear coordinates so that the higher energy, usually $^3\text{MLCT}$ excited state potential energy surface is not usually much distorted by mixing between these states and the barriers to crossing between them are large at 77 K.^{58, 80} On the other

hand these barriers are often small enough that crossing is rapid at 300 K, consistent with the difficulty in finding an ambient emission from these complexes and with the previous work of CH₃CN photodissociation from [Ru(TQA)(MeCN)₂]²⁺ at room temperature.⁹³

The ³MLCT emission of these complexes has a very small radiative rate constants. The radiative rate constants span the range observed for Ru-bpy and Ru-MDA complexes.

3.7. Overview: summary of significance and implications

The DFT modeling and the observed variations in vibronic sideband contributions have led to a model of the Ru-Ar triplet charge transfer excited states in which the HOMO of the aromatic ligand radical anion, Ar^{-•}, mixes with the partly occupied dπ(Ru^{III}) orbital to form the donor-SOMO. The resulting excited state interactions can be qualitatively addressed in terms of a simple Huckel-level treatment in which the MLCT/ππ* excited state mixings are treated in terms of the mixings between the Ar^{-•}-HOMO, the Ar^{-•}-SOMO and the partly occupied dπ(Ru^{III}) orbital where only the dπ orbital mixings are important and result in stabilization energies ε_x:



Then the ground and triplet excited state energies for a four electron system are: $E_G = 2E_a$ and $E_E = 2E_a + E_b - \epsilon_a$. Thus, the observed excited state energy varies as $\Delta E = (E_E - E_G) = E_b - \epsilon_a + 2\epsilon_b$. The stabilization energies are the square of the appropriate matrix element divided by the energy difference between the mixed states so that as $E_a \rightarrow 0$ or for $E_a < H_a$, $E_a \rightarrow H_a$ and the π and $d\pi$ orbitals are totally mixed.

This simple model for excited state electronic mixing is qualitatively consistent with the energy relationships observed for these complexes. In the limit of weak configurational mixing between the acceptor ligand states and the electronic states of the metal the stabilization energies will be small compared to the energy differences between electronic states so that $\epsilon_x \ll (E_a \text{ or } E_b)$ so that $\Delta E(\text{weak}) \approx (E_b - E_a)$. Within this context, the free energy difference between the one electron oxidation and reduction of the ground state is also approximately equal to E_b . Thus, in the weak mixing limit one expects a nearly 1:1 correspondence between the electrochemically determined oxidation and reduction free energies, $-F\Delta E_{1/2}$, for a series of closely related complexes and their emission band origins (which are usually very close to $h\nu_{\text{max}}(\text{emis})$ for these complexes). This has been found to be very close to the case for Ru-bpy chromophores,^{61-62, 95} although the slopes of the correlations may be closer to 0.8:1.⁹⁶ For $E_a \ll E_b$ and/or very strong excited state mixing, $\Delta E \approx E_b$ while the electrochemical relationships will be unchanged so that the emission band origin would be expected at energies much greater than those expected based on a 1:1 electrochemical correlation. This is consistent with our observations on the Ru-quinoline chromophores.

REFERENCES

1. Jortner, J.; Ottolenghi, M.; Stein, G., The Formation of Solvated Electrons in the Photochemistry of the Phenolate Ion in Aqueous Solutions. *J. Phys. Chem.* **1963**, *85*, 2712.
2. Buxton, G. V.; Greenstock, C. L.; Helman, W. P.; Ross, A. B., Critical review of rate constants for reactions of hydrated electrons, hydrogen atoms and hydroxyl radicals (OH/O⁻) in aqueous solution. *J. Phys. Chem. Ref. Data.* **1988**, *17*, 513.
3. Crosby, G. A., Spectroscopic Investigations of Excited-States of Transition-Metal Complexes. *Accounts of Chemical Research* **1975**, *8* (7), 231-238.
4. Malouf, G.; Ford, P. C., Photochemistry of the ruthenium (II) ammine complexes, Ru (NH₃)₅ (py-X)²⁺. Variation of systemic parameters to modify photochemical reactivities. *Journal of the American Chemical Society* **1977**, *99* (22), 7213-7221.
5. Wagenknecht, P. S.; Ford, P. C., Metal centered ligand field excited states: Their roles in the design and performance of transition metal based photochemical molecular devices. *Coordination Chemistry Reviews* **2011**, *255* (5-6), 591-616.
6. Österman, T.; Abrahamsson, M.; Becker, H.-C.; Hammarström, L.; Persson, P., Influence of Triplet State Multidimensionality on Excited State Lifetimes of Bis-tridentate RuII Complexes: A Computational Study. *The Journal of Physical Chemistry A* **2012**, *116* (3), 1041-1050.
7. Bonnett, R., Photosensitizers of the Porphyrin and Phthalocyanine Series for Photodynamic Therapy. *Chemical Society Reviews* **1995**, *24* (1), 19-33.
8. Dougherty, T. J.; Gomer, C. J.; Henderson, B. W.; Jori, G.; Kessel, D.; Korbelik, M.; Moan, J.; Peng, Q., Photodynamic therapy. *J Natl Cancer Inst* **1998**, *90* (12), 889-905.

9. Sun, L. C.; Hammarstrom, L.; Akermark, B.; Styring, S., Towards artificial photosynthesis: ruthenium-manganese chemistry for energy production. *Chemical Society Reviews* **2001**, *30* (1), 36-49.
10. Balzani, V.; Juris, A., Photochemistry and photophysics of Ru(II)□polypyridine complexes in the Bologna group. From early studies to recent developments. *Coordination Chemistry Reviews* **2001**, *211* (1), 97-115.
11. Hupp, J. T.; Williams, R. D., Using resonance Raman spectroscopy to examine vibrational barriers to electron transfer and electronic delocalization. *Accounts Chem Res* **2001**, *34* (10), 808-817.
12. Xie, P.; Chen, Y. J.; Endicott, J. F.; Uddin, M. J.; Seneviratne, D.; McNamara, P. G., The metal-to-ligand charge-transfer luminescences of ruthenium(II)-polypyridine-tetraam(m)ine complexes. Support for the interconvertibility of optical and thermal (kinetic) Franck-Condon parameters. *Inorg Chem* **2003**, *42* (17), 5040-2.
13. Xie, P.; Chen, Y. J.; Uddin, M. J.; Endicott, J. F., The characterization of the high-frequency vibronic contributions to the 77 K emission spectra of ruthenium-am(m)ine-bipyridyl complexes, their attenuation with decreasing energy gaps, and the implications of strong electronic coupling for inverted-region electron transfer. *J Phys Chem A* **2005**, *109* (21), 4671-89.
14. Chen, Y. J.; Xie, P.; Endicott, J. F.; Odongo, O. S., Probes of the metal-to-ligand charge-transfer excited states in ruthenium-Am(m)ine-bipyridine complexes: the effects of NH/ND and CH/CD isotopic substitution on the 77 K luminescence. *J Phys Chem A* **2006**, *110* (25), 7970-81.

15. Chen, Y. J.; Endicott, J. F.; McNamarra, P. G., Contrasts in the 77 K emission spectra, structures, and dynamics of metal-to-metal and metal-to-ligand charge-transfer excited states. *J Phys Chem B* **2007**, *111* (24), 6748-60.
16. Einstein, A., Über einen die Erzeugung und Verwandlung des Lichtes betreffenden heuristischen Gesichtspunkt *Annalen der Physik* **1905**, *17* (6), 132.
17. Kloepfer, J. A.; Vilchiz, V. H.; Lenchenkov, V. A.; Chen, X.; Bradforth, S. E., Time-resolved scavenging and recombination dynamics from I:e-I:e- caged pairs. *J. Chem. Phys.* **2002**, *117*, 766.
18. Messina, F.; Bram, O.; Cannizzo, A.; Chergui, M., Real-time observation of the charge transfer to solvent dynamics. *Nat Commun* **2013**, *4*, 2119.
19. Noyes, R. M., Kinetics of competitive processes when reactive fragments are produced in pairs. *Journal of the American Chemical Society* **1955**, *77* (8), 2042-2045.
20. Noyes, R. M., Models Relating Molecular Reactivity and Diffusion in Liquids. *Journal of the American Chemical Society* **1956**, *78* (21), 5486-5490.
21. Buxton, G. V.; Dainton, F. S., Radical and molecular yields in the γ -radiolysis of water. II. The potassium iodide-nitrous oxide system in the pH range 0 to 14. *Proc. R. Soc. Lond. A* **1965**, *287* (1411), 427-443.
22. Czapski, G.; Ogdan, J.; Ottolenghi, M., On the photochemical cage effect in aqueous solutions of the halide ions. *Chemical Physics Letters* **1969**, *3* (6), 383-385.
23. Buxton, G. V.; Dainton, F. S., Radical and molecular yields in the γ -radiolysis of water. II. The potassium iodide-nitrous oxide system in the pH range 0 to 14. *Proc. R. Soc. Lond. A* **1965**, *287* (1411), 427-443.

24. Harned, H. S.; Owen, B. B., *The Physical Chemistry of Electrolytic Solutions*. 3rd ed.; Reinhold Pub. Corp.: New York, 1958.
25. Meisel, D.; Matheson, M. W.; Mulac, W. A.; Rabani, J., Transients in the flash photolysis of aqueous solutions of tris(2,2'-bipyridine)ruthenium(II) ion. *J. Phys. Chem.* **1977**, *81*, 1449.
26. Thompson, D. W.; Wishart, J. F.; Brunschwig, B. S.; Sutin, N., Efficient Generation of the Ligand Field Excited State of Tris-(2,2'-bipyridine)-ruthenium(II) through Sequential Two-Photon Capture by [Ru(bpy)₃]²⁺ or Electron Capture by [Ru(bpy)₃]³⁺. *J. Am. Chem. Soc.* **2001**, *105*, 8117.
27. Goetz, M.; von Ramin-Marro, D.; Musa, M. H. O.; Schiewek, M., Photoionization of [Ru(bpy)₃]²⁺: A Catalytic Cycle with Water as Sacrificial Donor. *J. Phys. Chem. A* **2004**, *108*, 1090.
28. Tarnovsky, A. N.; Gawelda, W.; Johnson, M.; Bressler, C.; Chergui, M., Photexcitation of Aqueous Ruthenium(II)-tris-(2,2'-bipyridine) with High-Intensity Femtosecond Laser Pulses *J. Phys. Chem. B*, **2006**, *110*, 26497.
29. Goetz, M.; von Ramin-Marro, D., The photoreduction of [Ru(bpy)₃]³⁺ investigated by two-pulse two-colour laser-flash photolysis. *Chemical Physics Letters* **2007**, *47*, 352.
30. Kloepfer, J. A.; Vilchiz, V. H.; Lenchenkov, V. A.; Germaine, A. C.; Bradforth, S. E., The ejection distribution of solvated electrons generated by the one-photon photodetachment of aqueous I⁻ and two-photon ionization of the solvent. *J. Chem. Phys.* **2000**, *113*, 6228.

31. Messina, F.; Bram, O.; Cannizzo, A.; Chergui, M., Real-time observation of the charge transfer to solvent dynamics. *Nature Communications* **2013**, *4*, 3119/1-3119/6.
32. Matsubara, T.; Efrima, S.; Metiu, H. I.; Ford, P. C., Solvent Effects on the Electronic Spectra of the Ruthenium(II) Complexes $\text{Ru}(\text{NH}_3)_6^{2+}$ and $\text{Ru}(\text{en})_3^{2+}$: Evidence for Charge Transfer to Solvent Transitions. *Journal of the Chemical Society, Faraday Transactions 2: Molecular and Chemical Physics* **1979**, *75*, 390.
33. Matsubara, T.; Ford, P. C., Photochemistry of the Ruthenium(II)-Saturated Amine Complexes in Aqueous Solution. *Inorg. Chem.* **1978**, *17*, 1747.
34. Yurenev, P. V.; Kretov, M. K.; Scherbinin, A. V.; Stepanov, N. F., Environmental broadening of the CTTS bands: the hexaammineruthenium(II) complex in aqueous solution. *J. Phys. Chem. A* **2010**, *114*, 12804.
35. Yurenev, P. V.; Scherbinin, A. V.; Stepanov, N. F., Hybrid Ab Initio/EFP Approach for Calculating d-d Absorption Spectrum of Hexaammineruthenium(II) Ion in Aqueous Solutions. *International Journal of Quantum Chemistry* *108*, 2711.
36. Chen, Y.-J.; Endicott, J. F.; Swayambunathan, V., Mixed-Valence Properties of the Metal to Ligand Charge Transfer Excited States of Polypyridyl-Bridged Bis-Ruthenium(II) Complexes. *Chem. Phys.* **2006**, *326*, 79.
37. Mazumder, S.; Thomas, R. A.; Lord, R. L.; Van Camp, R. A.; Schlegel, H. B.; Endicott, J. F., A DFT and Spectroscopic study of Intramolecular Electron-Transfer in some mono-Bipyridine Ruthenium(II) Complexes. *Can. J. Chem.* **2014**, *Submitted*.
38. Thomas, R. A.; Tsai, C. N.; Mazumder, S.; Lu, I. C.; Lord, R. L.; Schlegel, H. B.; Endicott, J. F.; Chen, Y. J., Energy Dependence of the Ruthenium(II)-Bipyridine Metal-

to-Ligand-Charge-Transfer Excited State Radiative Lifetimes: Effects of $3\pi\pi^*$ (bipyridine) Mixing. *J. Phys. Chem. B* **2015**, *119* (24), 7393.

39. *Origin 9.0* Origin Lab Corp.: Northampton, MA.

40. *PSI-Plot*, Polysoftware International: Pearl River, NY.

41. Müller, P.; Brettel, K., [Ru(bpy)₃]²⁺ as a reference in transient absorption spectroscopy: differential absorption coefficients for formation of the long-lived 3MLCTexcited state. *Photochem. Photobiol. Sci.* **2012**, *11* (632).

42. Braterman, P. S.; Harriman, A.; Heath, G. A.; Yellowlees, L. J., The Electronic Absorption Spectrum and Structure of the Emitting State of the Tris(2,2'-bipyridyl)ruthenium(II) Complex Ion. *J. Chem. Soc. Dalton Trans.* **1983**, 1801.

43. Meisel, D.; Matheson, M. S.; Mulac, W.; Rabani, J., Transients in the flash photolysis of aqueous solutions of tris (2, 2'bipyridine) ruthenium (II) ion. *The Journal of Physical Chemistry* **1977**, *81* (15), 1449-1455.

44. Goetz, M.; von Ramin-Marro, D.; Othman Musa, M. H.; Schiewek, M., Photoionization of [Ru (bpy) ₃] ²⁺: A catalytic cycle with water as sacrificial donor. *The Journal of Physical Chemistry A* **2004**, *108* (6), 1090-1100.

45. Tarnovsky, A.; Gawelda, W.; Johnson, M.; Bressler, C.; Chergui, M., Photexcitation of Aqueous Ruthenium (II)-tris-(2, 2 '-bipyridine) with High-Intensity Femtosecond Laser Pulses. *The Journal of Physical Chemistry B* **2006**, *110* (51), 26497-26505.

46. Buxton, G. V.; Greenstock, C. L.; Helman, W. P.; Ross, A. B., Critical review of rate constants for reactions of hydrated electrons, hydrogen atoms and hydroxyl radicals (·

OH· O⁻ in aqueous solution. *Journal of physical and chemical reference data* **1988**, *17* (2), 513-886.

47. Marcus, R. A., Chemical and electrochemical and electrochemical electron-transfer theory. *Annu. Rev. Phys. Chem.* **1964**, *15*, 155.

48. White, J. K.; Schmehl, R. H.; Turro, C., An overview of photosubstitution reactions of Ru(II) imine complexes and their application in photobiology and photodynamic therapy. *Inorganica Chimica Acta* **2017**, *454*, 7.

49. Adamson, A. W., transition metal complex photochemistry. *Discussions Faraday Society* **1960**, *29*, 163.

50. Van Houten, J.; Watts, R. J., Temperature Dependence of the Photophysical and Photochemical Properties of the Tris(2,2'-bipyridyl)ruthenium(II) Ion in Aqueous Solution. *J. Am. Chem. Soc.* **1976**, *98*, 4853.

51. Durham, B.; Caspar, J. V.; Nagle, J. K.; Meyer, T. J., Photochemistry of tris (2, 2'-bipyridine) ruthenium (2+) ion. *J. Am. Chem. Soc.* **1982**, *104*, 4803.

52. Endicott, J. F.; Ramasami, T.; Tamilarasan, R.; Lessard, R. B.; Brubaker, G. R., Structure and reactivity of the metal-centered transition metal excited states. *Coord. Chem. Rev.* **1987**, *77*, 1.

53. Sauvage, J.-P.; Collin, J.-P.; Chambron, J.-C.; Guillerez, S.; Coudret, C.; Balzani, V.; Barigelletti, F.; De Cola, L.; Flamigni, L., Ruthenium(II) and Osmium(II) bis(terpyridine) complexes in covalently-linked multicomponent systems: synthesis, electrochemical behavior, absorption spectra, and photochemical and photophysical properties. *Chem. Rev.* **1994**, *94*, 993.

54. Balzani, V.; Juris, A.; Venturi, M.; Campagna, S.; Serroni, S., Luminescent and Redox-Active Polynuclear Transition Metal Complexes. *Chem. Rev.* **1996**, *96*, 759.
55. Endicott, J. F.; Perkovic, M. W.; Heeg, M. J.; Ryu, C. K.; Thompson, D., Ligand-Induced, Stereochemical Relaxation of Electronic Constraints in a Simple Chemical Process Examples from Hexaam(m)ine Cr(III) Photophysics. In *Electron Transfer Reactions: Inorganic, Organometallic and Biological Applications*, Isied, S. S., Ed. American Chemical Society: Washington, D. C., 1997; Vol. 253, pp 199-220.
56. Tfouni, E., Photochemical reactions of ammineruthenium(II) complexes. *Coord. Chem. Rev.* **2000**, *196*, 281.
57. Tsai, C.-N.; Tian, Y.-H.; Shi, X.; Lord, R. L.; Schlegel, H. B.; Chen, Y. J.; F., E. J., Experimental and DFT Characterization of Metal-to-Ligand Charge-Transfer Excited States of (Rutheniumammine)(Monodentate Aromatic Ligand) Chromophores. *Inorg. Chem.* **2013**, *52* (17), 9774-9790.
58. Tsai, C. N.; Mazumder, S.; Shi, X.; Zhang, X. Z.; Schlegel, H. B.; Chen, Y. J.; Endicott, J. F., Metal-to-Ligand Charge-Transfer Emissions of Ruthenium(II) Pentaammine Complexes with Monodentate Aromatic Acceptor Ligands and Distortion Patterns of their Lowest Energy Triplet Excited States. *Inorg. Chem.* **2015**, *54*, 8495.
59. Yoshikawa, N.; Yamabe, S.; Sakaki, S.; Kanehisa, N.; Inoue, T.; Takashima, H., Transition states of the 3MLCT to 3MC conversion in Ru(bpy)₂(phen derivative)₂⁺ complexes. *J. Molecular Structure* **2015**, *1094*, 98.
60. Kane-Maguire, N. A. P., Photochemistry and photophysics of coordination compounds: chromium. *Topics in Current Chemistry* **2007**, *280*, 37.

61. Gorelsky, S. I.; Kotov, V. Y.; Lever, A. B. P., Vertical ionization energies and electron affinities of ions in solution from outer-sphere charge transition energies. *Inorg. Chem.* **1998**, *37* (18), 4584.
62. Lever, A. B. P.; Dodsworth, E. S., Echem and CT. In *Electronic Structure and Spectroscopy of Inorganic Compounds, Vol. II*, Lever, A. B. P.; Solomon, E. I., Eds. Wiley: New York, 1999; p 227.
63. Diamantis, P.; Gonthier, J. F.; Tavernelli, I.; Rothlisberger, U., Study of the Redox Properties of Singlet and Triplet Tris(2,2'-bipyridine)ruthenium(II) ([Ru(bpy)₃]²⁺) in Aqueous Solution by Full Quantum and Mixed Quantum/Classical Molecular Dynamics Simulations. *J. Phys. Chem. B* **2014**, *118*, 3950–3959.
64. Demas, J. N.; Crosby, G. A., Quantum Efficiencies on Transition Metal Complexes. 11. Charge-Transfer Luminescence. *J. Am. Chem. Soc.* **1971**, *93*, 2841.
65. Sun, Q.; Mosquera-Vazquez, S.; Daku, L. M. L.; Guénee, L.; Goodwin, H. A.; Vauthey, E.; Hauser, A., Experimental Evidence of Ultrafast Quenching of the 3MLCT Luminescence in Ruthenium(II) Tris-bipyridyl Complexes via a 3d State. *J. Am. Chem. Soc.* **2013**, *135* (37), 13660.
66. Wang, P.; Zakeeruddin, S. M.; Moser, J. E.; Nazeeruddin, M. K.; Sekiguchi, T.; Gratzel, M., A stable quasi-solid-state dye-sensitized solar cell with an amphiphilic ruthenium sensitizer and polymer gel electrolyte. *Nat Mater* **2003**, *2* (6), 402-7.
67. Garner, R. N.; Gallucci, J. C.; Dunbar, K. R.; Turro, C., [Ru(bpy)₂(5-cyanouracil)₂]²⁺ as a potential light-activated dual-action therapeutic agent. *Inorg Chem* **2011**, *50* (19), 9213-5.

68. Dhar, S.; Nethaji, M.; Chakravarty, A. R., Steric protection of a photosensitizer in a N,N-bis[2-(2-pyridyl)ethyl]-2-phenylethylamine-copper(II) bowl that enhances red light-induced DNA cleavage activity. *Inorg Chem* **2005**, *44* (24), 8876-83.
69. Klein, C.; Nazeeruddin, M. K.; Liska, P.; Di Censo, D.; Hirata, N.; Palomares, E.; Durrant, J. R.; Gratzel, M., Engineering of a novel ruthenium sensitizer and its application in dye-sensitized solar cells for conversion of sunlight into electricity. *Inorg Chem* **2005**, *44* (2), 178-80.
70. Holder, A. A.; Zigler, D. F.; Tarrago-Trani, M. T.; Storrie, B.; Brewer, K. J., Photobiological impact of $[(bpy)_2Ru(dpp)]_2RhCl_2]Cl_5$ and $[(bpy)_2Os(dpp)]_2RhCl_2]Cl_5$ [bpy=2,2'-bipyridine; dpp=2,3-Bis(2-pyridyl)pyrazine] on vero cells. *Inorg Chem* **2007**, *46* (12), 4760-2.
71. Barbara, P. F.; Meyer, T. J.; Ratner, M., *J. Phys. Chem.* **1996**, *100*, 13148.
72. Crosby, G. A., Rubpy. *Acc. Chem. Res.* **1975**, *8*, 231.
73. Endicott, J. F.; Chen, Y.-J., Charge Transfer-Excited State Emission Spectra of Mono- and Bi-Metallic Coordination Complexes: Band Shapes, Reorganizational Energies and Implications for Lifetimes. *Coord. Chem. Rev.* **2007**, *251*, 328.
74. Balzani, V.; Juris, A.; Venturi, M.; Campagna, S.; Serroni, S., Luminescent and Redox-Active Polynuclear Transition Metal Complexes. *Chem. Reviews* **1996**, *96*, 759.
75. Kober, E. M.; Casper, J. V.; Lumpkin, R. S.; Meyer, T. J., *J. Phys. Chem.* **1986**, *90*, 3722.

76. Myers, A. B., Relating absorption, emission, and resonance-Raman spectra with electron transfer rates in photoinduced charge transfer systems. *Chem. Phys.* **1994**, *180*, 215.
77. Nozaki, K.; Takamori, K.; Nakatsugawa, Y.; Ohno, T., Theoretical Studies of Phosphorescence Spectra of Tris(2,2'-bipyridine) Transition Metal Compounds. *Inorg. Chem.* **2006**, *45*, 6161.
78. Yersin, H.; Braun, D.; Hensler, G.; Gallhuber, E., In *Vibronic Processes in Inorganic Chemistry*, Flint, C. D., Ed. Kluwer: Dordrecht, 1989; p 195.
79. Lord, R. L.; Allard, M. M.; Thomas, R., A.; Odongo, O. S.; Schlegel, H. B.; Chen, Y.-J.; Endicott, J. F., Structural Variations of Triplet Metal-to-Ligand-Charge-Transfer Excited States of Mono-Bipyridine-Ruthenium(II) Complexes: Comparisons of 77 K Emission Spectra and a Computational Model. *Inorg. Chem.* **2013**, *52*, 1185.
80. Mazumder, S.; Thomas, R. A.; Lord, R. L.; Schlegel, H. B.; Endicott, J. F., A density functional theory and spectroscopic study of intramolecular quenching of metal-to-ligand charge-transfer excited states in some mono-bipyridine ruthenium(II) complexes. *Can. J. Chem.* **2014**, *92* 996.
81. Tsai, C. N.; Mazumder, S.; Zhang, X. Z.; Schlegel, H. B.; Chen, Y. J.; Endicott, J. F., Charge Transfer Excited-States of Ruthenium(II)-(Acceptor Ligand) Chromophores: Intensity Stealing in Ruthenium(II) Complexes with Aromatic Acceptor Ligands. *Inorg. Chem.* **2016**, *55*, 7341.
82. Tsai, C.-N.; Shi, X.; Tian, Y.-H.; Yeh, M.-L.; Luo, D.-W.; Schlegel, H. B.; Chen, Y. J.; Endicott, J. F., Pyrazine-Bridged di-Ruthenium Complexes with Mixed Valence

Excited States: Spectroscopic Observations and Computational Modeling. *Inorg. Chem.* **2017**, *to be submitted* nnn.

83. Chen, Y.-J.; Xie, P.; Heeg, M. J.; Endicott, J. F., Influence of "innocent" ligands on the MLCT Excited-State Behavior of Mono(bipyridine)ruthenium(II) complexes. *Inorg. Chem.* **2006**, *45*, 6282.

84. Odongo, O. S.; Heeg, M. J.; Chen, Y.-J.; Xie, P.; Endicott, J. F., Variations in Ruthenium-Bipyridine-Complex Emission Bandshapes Induced by Excited State-Excited State Configurational Mixing *Inorg. Chem.* **2008**, *47*, 7493.

85. Xie, P.; Chen, Y.-J.; Uddin, M. J.; Endicott, J. F., The Characterization of the High-Frequency Vibronic Contributions to the 77 K Emission Spectra of Ruthenium-Am(m)ine-Bipyridyl Complexes, Their Attenuation with Decreasing Energy Gaps, and the Implications of Strong Electronic Coupling for Inverted-Region Electron Transfer. *J. Phy. Chem. A* **2005**, *109*, 4671.

86. Xie, P.; Chen, Y.-J.; Uddin, M. J.; Endicott, J. F., The Characterization of the High-Frequency Vibronic Contributions to the 77 K Emission Spectra of Ruthenium-Am(m)ine-Polypyridyl Complexes: Their Attenuation with Decreasing Energy Gaps and the Implications of Strong Electronic Coupling for Inverted-Region Electron-Transfer. *J. Phys. Chem. A* **2005**, *109*, 4671.

87. Mikata, Y.; Kawata, K.; Iwatsuki, S.; Konno, H., Zinc-specific fluorescent response of tris(isoquinolylmethyl)amines (isoTQAs). *Inorg Chem* **2012**, *51* (3), 1859-65.

88. Sharma, R.; Knoll, J. D.; Ancona, N.; Martin, P. D.; Turro, C.; Kodanko, J. J., Solid-phase synthesis as a platform for the discovery of new ruthenium complexes for efficient release of photocaged ligands with visible light. *Inorg Chem* **2015**, *54* (4), 1901-11.
89. Curtis, J. C.; Sullivan, B. P.; Meyer, T. J., Hydrogen-Bonding-Induced Solvatochromism in the Charge-Transfer Transitions of Ruthenium(II) and Ruthenium(III) Ammine Complexes. *Inorganic Chemistry* **1983**, *22* (2), 224-236.
90. Russell, M. G.; Carling, R. W.; Atack, J. R.; Bromidge, F. A.; Cook, S. M.; Hunt, P.; Isted, C.; Lucas, M.; McKernan, R. M.; Mitchinson, A.; Moore, K. W.; Narquizian, R.; Macaulay, A. J.; Thomas, D.; Thompson, S. A.; Wafford, K. A.; Castro, J. L., Discovery of functionally selective 7,8,9,10-tetrahydro-7,10-ethano-1,2,4-triazolo[3,4-a]phthalazines as GABA A receptor agonists at the α_3 subunit. *J Med Chem* **2005**, *48* (5), 1367-83.
91. Ragazzon, G.; Verwilst, P.; Denisov, S. A.; Credi, A.; Jonusauskas, G.; McClenaghan, N. D., Ruthenium (II) complexes based on tridentate polypyridine ligands that feature long-lived room-temperature luminescence. *Chemical Communications* **2013**, *49* (80), 9110-9112.
92. Mazumder, S.; Thomas, R. A.; Lord, R. L.; Schlegel, H. B.; Endicott, J. F., A density functional theory and spectroscopic study of intramolecular quenching of metal-to-ligand charge-transfer excited states in some mono-bipyridine ruthenium(II) complexes. *Can. J. Chem.* **2014**, *92*, 996

93. Sharma, R.; Knoll, J. D.; Ancona, N.; Martin, P. D.; Turro, C.; Kodanko, J. J., Solid-Phase Synthesis as a Platform for Discovering Photoactivated Ruthenium Complexes. Submitted for Publication.
94. Birks, J. B., *Photophysics of Aromatic Molecules*. Wiley-Interscience: New York, 1970.
95. Dodsworth, E. S.; Lever, A. B. P., Correlations between electrochemical potentials and optical charge transfer energies in ruthenium bipyridine derivatives. *Chem. Phys. Lett.* **1986**, *124*, 152.
96. Allard, M. M.; Odongo, O. S.; Lee, M. M.; Chen, Y.-J.; Endicott, J. F.; Schlegel, H. B., Effects of Electronic Mixing in Ruthenium(II) Complexes with Two Equivalent Acceptor Ligands. Spectroscopic, Electrochemical and Computational Studies. *Inorg. Chem.* **2010**, *49*, 6840.

ABSTRACT**CHEMICAL AND PHYSICAL STUDIES OF CHARGE TRANSFER EXCITED STATES OF RUTHENIUM COMPLEXES WITH AROMATIC LIGANDS**

by

MARIM KHALIFA ALNAED**August 2018****Advisors:** Dr. John F. Endicott and Dr. Wen Li**Major:** Chemistry (Analytical)**Degree:** Doctor of Philosophy

The $^3\text{MLCT}$ excited states generated from tris-bipyridineruthenium(II), $[\text{Ru}(\text{bpy})_3]^{2+}$ and related complexes were ionized by 405 nm irradiation in ambient, acidic aqueous solutions. The photoionization product was $\text{Ru}(\text{bpy})_3^{3+}$ and an electron with a quantum yield of about 0.04 ± 0.02 in 0.5 M acid. However, 532 nm radiation does not induce photoionization, but it generates the $^3\text{MLCT}$ excited state that can be photoionized by 405 nm irradiation. Dramatic decreases in $[\text{Ru}(\text{bpy})_3]^{2+}$ emission intensities were observed when dual laser irradiations were used for 10-30 min in 0.5 M H^+ . The proton is a very good electron scavenger, and the rate of photoionization of the $^3\text{MLCT}$ excited state was determined to be acid dependent and it increased about ten-fold for acid concentrations between 0.001 and 4 M when 0.1 M isopropanol was used to scavenge hydrogen atoms. The increase in photoionization rate at acid concentration greater than 0.1 M indicate that the proton scavenges electron containing ion pair species in highly acidic solutions. The minimum free energy required to ionize the $[\text{Ru}(\text{bpy})_3]^{2+}$ $^3\text{MLCT}$ excited state is about 2

eV (620 nm). Such thermodynamic considerations also indicate that photoionization processes are possible for many of the electron donors whose excited states might be considered for use as photosensitizers. This suggests that the shorter wavelength visible light could lead to their degradation through reactions of the resulting free radicals and other product species when they are used in long term applications.

Ru-quinoline chromophores of the general formula $[\text{Ru}(\text{iso-TQA})\text{L}_2]^{n+}$, where TQA is tris(isoquinolin-1-ylmethyl)amine, and L is MeCN, CN or SCN, and $n = 0$ or 2 , have some unique spectroscopic and photophysical properties. DFT modeling suggests that the Ru-TQA excited states have very different electronic configurations where the emitting excited state has the same contribution from quinolone- $\pi\pi^*$ character as MLCT. In addition, the lowest energy absorption bands of the Ru-TQA complexes are not typical MLCT absorptions, it contains a convolution of several near in energy absorption bands. Furthermore, those complexes were determined to have a long lifetime and large quantum yields at 77 K and the vibronic structure of those complex are large and that might arise from $^3\text{MLCT} / ^3\pi\pi^*$ mixing.

AUTOBIOGRAPHICAL STATEMENT

MARIM KHALIFA ALNAED

Professional Preparation

- Graduate** - Wayne State University, Detroit, MI
 - Ph.D. in Analytical Chemistry (inorganic spectroscopy), 2018
- Undergraduate** - Tripoli University, Tripoli, Libya
 - B.S. Chemistry, 1998

Presentations

- " Visible Light Photoionization of the tris-Bipyridine-Ruthenium(II) Triplet Metal to Ligand Charge Transfer Excited State: Observations and Implications" Talk -The ACS Central Regional Meeting, Dearborn, MI, June 2017
 "The Photo-Generation of Electrons (and Hydrogen-atoms) from the Near-Ultraviolet Irradiation of tris-(bipyridine) Ruthenium(II)" Poster- Chemistry Department Symposium, Wayne State University, Detroit, MI, 2015

Publications

Alnaed, M. K.; J. F. Endicott, "The Visible Light Photoionization of the tris-Bipyridine-Ruthenium(II) Triplet Metal-to Ligand Charge-Transfer Excited State: Chemical Scavenging Probes of the Threshold Energy and Short-Lived Intermediates," manuscript will be submitted soon.

Huisman, **M;** **Alnaed**, M.K.; Kodanko, J. J, "An Affinity Enhanced Luminescent Probe for Targeting and Imaging Cathepsin L", *Inorg. Chem*, **2018**, 57, 13, 788.

Alnaed, M.K.; R. A. Thomas, Y. Tu, Y. J. Chen, J. J. Kodanko, H. B. Schlegel and J. F. Endicott, *Characterization of the Electronic Excited States Ruthenium-Quinoline Chromophores: Spectroscopy and Density Functional Theory Modeling*, manuscript in preparation.

Alnaed, M. K.; "Studies on the Chemical Nature of Maltenes Separated from Sludge Deposits" Proceedings of The International Conference on Stability and Handling of Liquid Fuels, 7th, Graz, Austria, Sept. 24-29, 2000, 1, p.321.